ANALYSIS OF HIGH RATE FRACTURE TESTS OF POLYMERS

By
Alexander Rager

Department of Mechanical Engineering
Imperial College London
Exhibition Road, London SW7 2BX

A Thesis submitted for the degree of Doctor of Philosophy
of the University of London and for the Diploma of Imperial College

February 2003

Abstract

This work is concerned with the three point bend impact test on polymers. A test series with three different polymers was performed and the time to fracture from the three point bend impact test was measured. Data from a round robin within ESIS, which was performed as a part of this work, is also presented. A dependency of the time to fracture with impact velocity was found and was explained with a thermal model. Numerical modeling of the three point bend test with a finite volume program was employed to enhance understanding of the test and to obtain dynamic correction functions, which are necessary to calculate K and G from time to fracture. A simple model of the three point bend test and a more complicated model, which included contact effects, were analyzed. A good fit with the experiment was found for the contact model. The anvils were found to be important only at a late stage in the test. Various test parameters were varied to investigate their influence on the dynamic correction function. The contact stiffness was found to have an important influence on the shape of the dynamic correction function. Due to the nonlinear contact stiffness the impact velocity also affects the dynamic correction function. For a polymer specimen and a steel striker the specimen width and the specimen material were found to have only a small influence on the dynamic correction function. The dynamic correction function for G was found to exhibit higher oscillations than the dynamic correction function for K and hence the former is a more sensitive parameter. The time to fracture results from the test series were converted into K and G with a procedure based on the numerical analysis.

Acknowledgements

My sincere thanks to my supervisor Prof. J. G. Williams who guided me throughout the project with patience and constant encouragement. Many thanks also to Dr. A. Ivankovic who who was of invaluable help and full of optimism during the numerical part of my project. I am grateful to Hugh MacGillivray, Dr. P. S. Leevers and Dr. B. Blackman for their help and advice. Special thanks to Dr. V. Tropsa for his assistance with the numerical work. I am also grateful to Nick Tailor, P. Savage, Dr. S. Hazra, Dr. L. Moreno and Dr. J. M. Smith.

Many thanks to my parents, who were always there to support me and to Michaela.

The financial support provided by Delphi is gratefully acknowledged.

Contents

Nomenclature

Latin alphabet

a	Crack length
b_i	Polynomial coefficients
c_b	Bar wave speed
c_l	Longitudinal wave speed
c_t	Transverse wave speed
c_r	Rayleigh wave speed
f	Geometry factor
$\boldsymbol{f}$	Body force vector
f_g	Upper frequency bound
g_d	Dynamic correction function for the energy release rate
$\boldsymbol{i}_x$	Unit vector in x-direction
k_d	Dynamic correction function for the stress intensity factor
k_1	Contact stiffness
k_2	Specimen stiffness
$\boldsymbol{n}$	Unit vector of outward normal
r	Radius
t	Time
$\boldsymbol{t}$	Traction vector
t_f	Time to fracture
t_g	Time to fracture from gold lines
t_r	Rise time
t_s	Time to fracture from strain gauge
u	Displacement
$\boldsymbol{u}$	Displacement vector
y	Distance from neutral axis
z_c	Critical distance

A	Area
B	Thickness
C_m	Machine compliance
C_s	Specimen compliance
D	Diameter of Caustic
E	Elastic modulus
E_k	Kinetic energy
E_s	Strain energy
G	Energy release rate
G_c	Critical energy release rate
G_d	Dynamic energy release rate
G_{st}	Static energy release rate
$H(t)$	Heavyside function
$\boldsymbol{I}$	Identity tensor
J	J integral
K	Stress intensity factor
K_c	Critical stress intensity factor
K_d	Dynamic stress intensity factor
K_{st}	Static stress intensity factor
L	Specimen length
M_b	Bending moment
P	Load
P_{max}	Maximum load
S	Span
S	Surface of body (Chapter 3)
T	Temperature
T_m	Transition temperature
U	Strain energy density
U_Q	Area under load-displacement curve
V	Impact velocity
V	Volume of body (Chapter 3)
W	Specimen width
W_e	External work
X	Nondimensional time
X_0	Starting point of k_d versus X curve on x axis
$1D$	One dimensional
$2D$	Two dimensional
$3D$	Three dimensional

Greek alphabet

α	Stiffness ratio
Γ, Γ_0	Paths around the crack tip
Δa	Crack extension
ΔT	Temperature rise
ε	Strain tensor
θ	Angle
λ, μ	Lamé constants
ν	Poisson's ratio
ν_o	Opening displacement of a point along a crack face
ν_t	Half of the crack tip opening displacement
ϕ	Energy calibration factor
ρ	Density
σ	Stress tensor
σ_{yy_t}	Stress component in y-direction at the crack tip
σ_0	Constant stress value
τ	Period of specimen oscillation
ψ	Dimensionless specimen compliance
∇	Nabla operator

Main abbreviations

CMOD	Crack mouth opening displacement
CTOD	Crack tip opening displacement
DSIF	Dynamic stress intensity factor
DOF	Degree of freedom
ESIS	European Structural Integrity Society
FD	Finite Difference
FE	Finite Element
FV	Finite Volume
IRC	Impact response curve
LEFM	Linear elastic fracture mechanics
OPB	One point bend
PE	Polyehtylene
PMMA	Polymethylacrylate
PVC	Poly-vinylchloride
SENB	Single edge notched bend specimen
SIF	Stress intensity factor
TPB	Three point bend

List of Figures

List of Tables

Chapter 1

Background

1.1 Introduction

Today polymers are found in a multitude of applications. In many cases it is necessary to know the fracture toughness of these materials and there is an increasing demand for the high rate properties of polymers. The automotive industry, for example, uses a large volume of polymers for car components and is especially interested in the fracture properties at impact rates. For quasi-static loading rates there are standard test procedures for the determination of fracture toughness and critical energy release rate available [1, 2]. For intermediate rates of loading below 1m/s a test procedure was developed by the European Structural Integrity Society (ESIS) [3]. For loading rates greater than 1m/s there is no standard test procedure for polymers available. The aim of this project is therefore to contribute towards a possible standard test method for determining fracture toughness and critical energy release rate for polymers at high rates ($>$ 1m/s).

1.2 Dynamic fracture mechanics

1.2.1 Basic definitions

This work only deals with fracture in Mode I. Therefore it is convenient to use K for the opening mode stress intensity factor K_I and G for the opening mode energy release rate G_I.

For a plane crack of a length a in a body of arbitrary size and loaded in Mode I the stress intensity factor K is defined as

$$K = \lim_{r \to 0} \sqrt{2\pi r}\, \sigma_{yy}(r, 0) \tag{1.1}$$

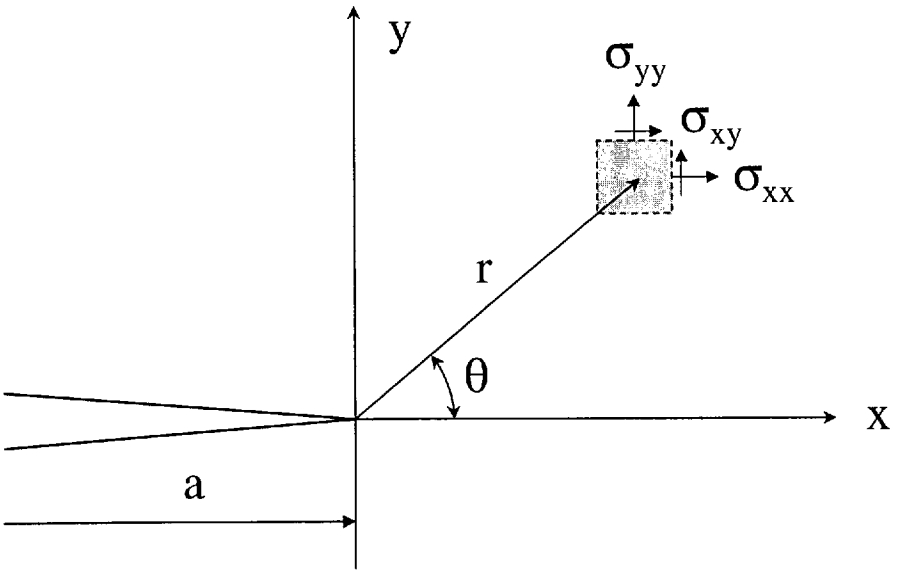

Figure 1.1: Coordinate system and stresses.

with the radius r , the angle θ and the principal stress in y-direction $\sigma_{yy}(r, \theta)$ (Figure 1.1). This relationship is valid for a stationary crack with constant or transient loading as well as for a moving crack.

The energy release rate, G, can be defined either in a global or a local way. Seen from the global position G can be derived from the global energy balance. G can then be written [4] as

$$G = \frac{dW_e}{dA} - \frac{dE_s}{dA} - \frac{dE_k}{dA} \tag{1.2}$$

with the external work, W_e, the strain energy, E_s, the kinetic energy, E_k, and the change in fracture area, dA. G has the units of J/m^2. The calculation of G from the global energy balance is only possible in the case of a crack advance and it is usually applied for calculating G for a moving crack as in [4].

Seen from a local perspective G can be defined with the crack tip closure integral, which was introduced by Irwin [5]. Irwin's contention was, that, if a crack is extended by a small amount, Δa, the energy absorbed in the process is equal to the work required to close the crack back to its original length. This can be expressed as

$$G = \lim_{\Delta a \to 0} \frac{1}{\Delta a} \int_0^{\Delta a} \sigma_{yy} \nu_o dx \tag{1.3}$$

where ν_o is the opening displacement of a point along a crack face [6, 7]. This expression for G is particularly suitable for computational purposes. Rybicki and Kanninen [6] as

well as Jih [8] used the crack tip closure integral to calculate the SIF in a FE program via Equation 1.4. The crack tip closure integral can be calculated for stationary cracks, as it does not need a crack advance.

In the case of a stationary crack in a static or transient field a relationship between K and G exists with [9]

$$G = \frac{\left(1-\nu^2\right) K^2}{E} \tag{1.4}$$

for plane strain, where E is the elastic modulus and ν is the Poisson's ratio. For plane stress the factor $\left(1-\nu^2\right)$ has to be omitted. With Equation (1.4) it is possible to calculate K from G obtained with the crack tip closure integral. It should be noted that even for a moving crack a relationship between K and G exists, which in this case depends upon the crack speed [9].

1.3 Stress wave propagation

Stresses in a body propagate as stress waves at certain speeds. This is important because it means that it takes a certain, finite time for the stress wave to reach a particular point in the body. Stress waves from a point of impact interact with the crack and create a change in the stress field around the crack tip. In an analytical study Brock [10] found indications that it is a complicated pattern of direct and reflected waves that essentially generates brittle fracture at the crack tip in a three point bend (TPB) test. This also means that the crack tip stress field is affected by the specimen geometry. The information of the specimen geometry is transported to the crack by reflected stress waves.

There are different types of waves which travel at different velocities. Detailed descriptions of stress waves can be found in [11] and [12]. In a thin bar the stress state is approximately one-dimensional [12]. The velocity of a wave propagating under a 1D state of stress can be calculated from

$$c_b = \left(\frac{E}{\rho}\right)^{\frac{1}{2}} \tag{1.5}$$

where c_b is usually called the bar wave speed. The material density is denoted as ρ.

In an infinite, elastic medium free from body forces there are two types of stress waves [11]. The first is the longitudinal wave with the wave speed

$$c_l = \left(\frac{\lambda+2\mu}{\rho}\right)^{\frac{1}{2}}. \tag{1.6}$$

It is also called dilatation wave or pressure wave (P-wave). λ and μ are the Lamé constants, which can be expressed with E and ν as

$$\lambda = \frac{\nu E}{(1+\nu)(1-2\nu)} \tag{1.7}$$

and

$$\mu = \frac{E}{2(1+\nu)}. \tag{1.8}$$

The latter, μ, is also called the shear modulus. The second type of waves in an infinite, elastic medium are transverse waves with a wave speed of

$$c_t = \left(\frac{\mu}{\rho}\right)^{\frac{1}{2}}. \tag{1.9}$$

This type of wave is also called the shear or S-wave. In contrast to longitudinal waves, shear waves do not change the volume of the body.

At a surface a different type of waves can propagate which are called Rayleigh waves. They are confined to a thin layer close to the surface and the Rayleigh wave speed depends upon the Poisson's ratio with

$$c_r = f(\nu)c_t \tag{1.10}$$

where $f(\nu)$ is a function which satisfies the Rayleigh equation for a given ν. Values for $f(\nu)$ can be found in [11]. For example for a Poisson's ratio of $\nu = 0.33$ we find $f(\nu) = 0.932$.

For a thin plate in plane stress the longitudinal wave speed is given by

$$c_l = \left(\frac{E}{\rho(1-\nu^2)}\right)^{\frac{1}{2}}. \tag{1.11}$$

This relationship is only valid when the wavelength is very large compared to the thickness of the plate. If the wavelength is very small compared to the thickness of the plate, longitudinal waves travel with the Rayleigh wave speed. Transverse waves in the thin plate in plane stress have the same wave speed as transverse waves in an infinite, elastic medium.

For plane strain the longitudinal and transverse wave speeds are the same as for the infinite, elastic medium.

Böhme [13] found that the interaction of the first longitudinal wave fronts with the crack generates an initial decrease of the stress intensity factor (SIF) in the TPB test. The first significant increase of the SIF was found at times comparable to the arrival time of the first direct transverse wave.

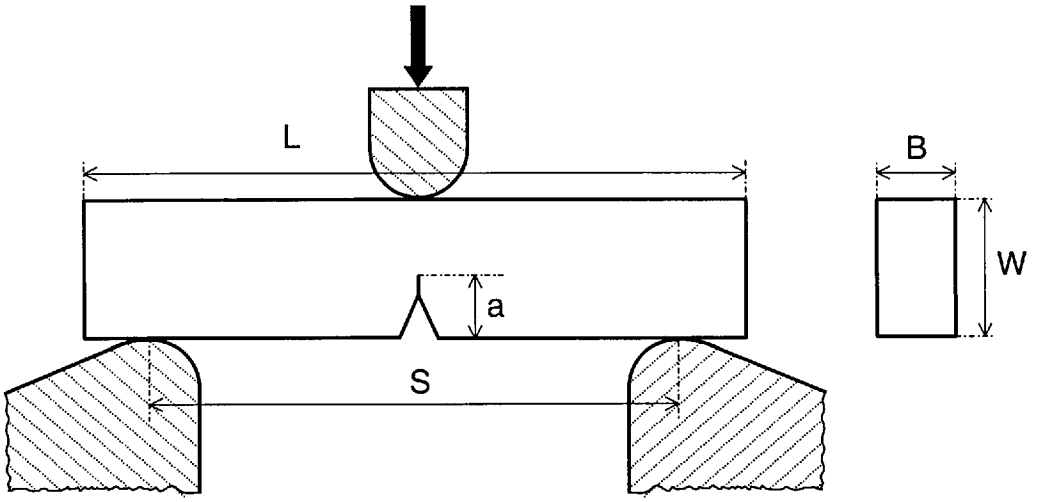

Figure 1.2: The TPB test configuration.

1.4 The quasi-static three point bend test

Figure 1.2 shows the test setup of the three point bend test with a single edge notched bend (SENB) specimen. For the determination of K_c and G_c at low testing rates under quasi-static conditions there is a standard test procedure available [2]. This procedure uses the load-displacement curve to obtain the fracture toughness and the critical strain energy release rate in a displacement controlled test. Linear elastic fracture mechanics (LEFM) is applied. If LEFM is valid, the fracture toughness can be calculated from

$$K_c = f\frac{P_{max}}{BW^{\frac{1}{2}}}. \tag{1.12}$$

P_{max} is the maximum load from the load-displacement curve in Figure 1.3. B is the thickness of the specimen and W is the specimen width. f is a geometry factor, which is dependent on a/W, the notch length ratio and S/W, the span ratio. For a SENB geometry f is calculated [14] with

$$f = \frac{6\left(\frac{a}{W}\right)^{\frac{1}{2}}\left(1.99 - \left(\frac{a}{W}\right)\left(1 - \left(\frac{a}{W}\right)\right)\left(2.15 - 3.93\left(\frac{a}{W}\right) + 2.7\left(\frac{a}{W}\right)^2\right)\right)}{\left(1 + 2\left(\frac{a}{W}\right)\right)\left(1 - \left(\frac{a}{W}\right)\right)^{\frac{3}{2}}} \tag{1.13}$$

for $S/W = 4$ and for a notch length ratio a/W between 0 and 1. The critical strain energy release rate is calculated from the area under the load-displacement curve, U_Q (Figure 1.3) with

$$G_c = f\frac{U_Q}{BW\phi} \tag{1.14}$$

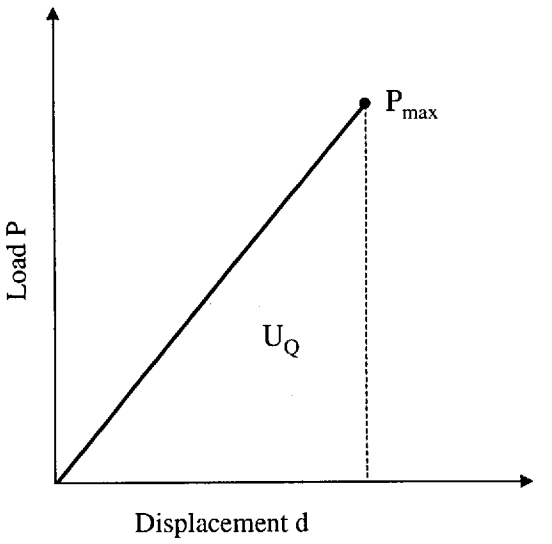

Figure 1.3: Schematic load-displacement curve.

where ϕ is the energy calibration factor, which can be found tabulated in the test procedure. U_Q should be corrected by subtracting the energy absorbed by the indentation of the specimen.

1.5 The dynamic three point bend test

1.5.1 Overview

Dynamic three point bend tests with notched samples have been performed for quite some time. Instrumented Charpy tests have been reported since 1926 [15] when the tests were conducted to determine the impact energy.

Various dynamic effects occur in the impact test. They make an evaluation of the test along the lines of the static procedure difficult to impossible, depending upon the test speed. Therefore Nash [16] did an analysis of the hammer forces and bending moments occurring in the impact test. He used a beam model, which is a 1D theory, to calculate the striker force and the bending moment in the beam during the test. Under the assumption of the stress distribution across the beam width to be similar for the static and dynamic case a stress intensity factor can be calculated from the central bending moment. This underlies many 1D methods.

One of the very important issues in a displacement controlled test is the influence of the contact stiffness between striker and specimen. Nash and Lange [17] investigated the influence of the contact stiffness on the TPB impact test. They used a beam model

with the first bending mode only and did calculations with and without a linearized contact law. Nash and Lange found good agreement with experiments for the model including contact effects. They concluded that a model without inclusion of contact stiffness does not yield a realistic description of the impact process. They also remarked that it is difficult to determine the initiation time from the load-time curve, as peaks in this curve are due to the dynamics of the system and not necessarily connected with crack initiation. Initiation time was measured in [17] with a strain gauge.

Saxon [18] connected the first peak in the load-time signal with the inertia loading from the acceleration of the specimen from rest to the striker velocity. He also linked the oscillations recorded after the inertia peak with the flexural response of the specimen. Saxon found that the initial load imparted to the specimen is governed by elastic wave mechanics.

Turner [19] pointed out that the prime effect in the TPB impact test is the specimen inertia. He introduced nondimensional factors such as a characteristic time, which is scaled with the natural frequency of the beam. Turner found that the contact stiffness is an important parameter in the TPB impact test and that the initial slope of the test can be related to the contact stiffness. He concluded that the whole test is governed by the vibrational characteristics of the beam-pendulum nose system. He proposed to calculate K from the central bending moment. He also proposed a time to fracture approach. As the determination of time to fracture from the load trace is not advisable, he recommended the use of strain gauges close to the crack tip or conductive strips across the crack path for this purpose.

Kishimoto [20] derived a simple formula for the dynamic stress intensity factor (DSIF) using Nash's analysis [16]. The DSIF is assumed to be proportional to the displacement of the specimen at the center. All bending modes except for the fundamental mode were neglected. Good agreement with a finite element (FE) solution was achieved for a saw-tooth shaped load input. It should be noted that this loading pattern is an idealized case. Also, the assumed rigid hinge connection between specimen and anvil does not hold in the experiment. This was also shown experimentally by Böhme and Kalthoff [21]. In [22] Kishimoto presented an improved version of his model from [20] and included the effect of rotatory inertia and transverse shear deformation using Timoshenko's beam theory. Both models calculate the SIF via a convolution integral from the striker load, which is an input parameter.

Kalthoff [23] did experiments with the shadow optical method of caustics, which is an optical tool for measuring stress intensity and applied this technique for investigating dynamic fracture phenomena. In a transparent material the displacements around the crack tip act as a divergent lens for parallel light passing through the specimen (Figure 1.4). A shadow area can be observed, which is surrounded by a luminous curve, the caustic. Examples of caustics in transmission and reflection can be seen in Figure 1.5.

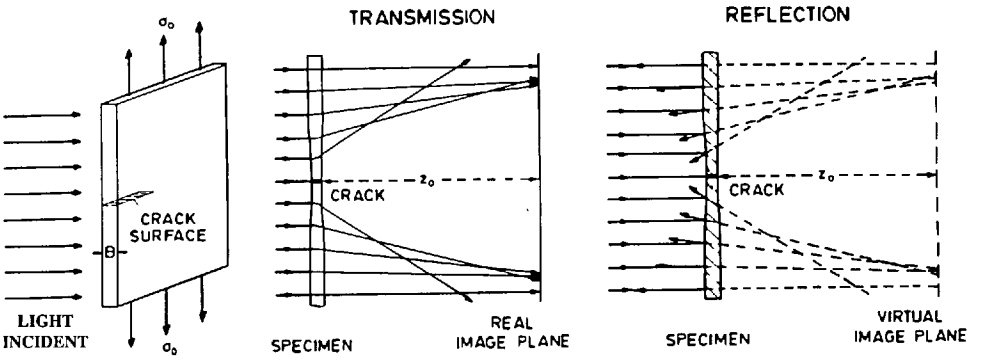

Figure 1.4: The principle of the shadow optical method of caustics. From [23].

For a non-transparent specimen a mirrored front surface is required. Due to surface deformation, light rays near the crack tip are reflected towards the center line and a similar caustic is obtained. The size of the shadow pattern is related to the SIF at the crack tip. The diameter of the caustic, D, is proportional to the SIF with

$$K \propto D^{\frac{5}{2}}. \tag{1.15}$$

Kalthoff and Böhme [23, 24] used a 24 spark high speed camera for photographing the shadow patterns under dynamic loading. The SIF was then obtained from evaluating the diameter of the caustic on the photographs and its conversion via Equation (1.15).

Böhme, together with Kalthoff [24, 21] did experiments on large epoxy specimens (Figure 1.6). He used Caustics in transmission to measure the DSIF. He also instrumented the anvil and the striker with strain gauges and recorded the specimen movement at the anvils with an optical system.

Böhme found that, as a first reaction to the impact, the specimen moves away from the anvils. In the case of a short specimen with length, L, to width, W, ratio $L/W = 4.1$ and the span to width ratio $S/W = 4$ a second impact occurs at the anvils. This was found not to be the case for longer specimen with $S/W = 5.5$. The movement of the specimen at the anvil contact point only started after a characteristic time. This time was found to coincide with the time needed for the transverse stress wave from the impact point to reach the anvils. Böhme concluded that the loss of contact at the anvils contradicts the boundary condition of a constant, zero displacement at the supports, which is often assumed in beam models e.g. in [16, 20]. Between the time of the striker impact and the impact of the specimen onto the supports the specimen is in a one point bend mode. This means that in this period the vibration pattern of an unsupported beam is excited.

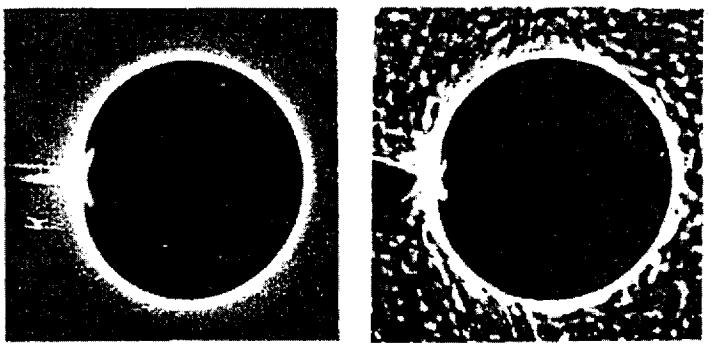

PMMA (TRANSMISSION) HIGH STRENGTH STEEL (REFLECTION)

Figure 1.5: Typical caustics in transmission and reflection. From [23].

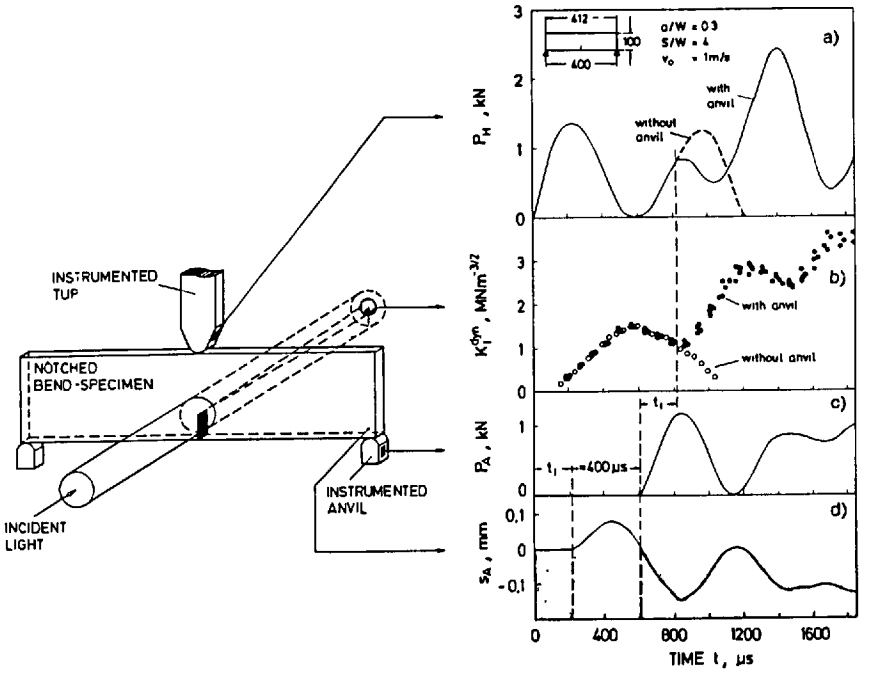

Figure 1.6: Böhme's test setup and the response of a short SENB specimen with $S/W = 4.1$. From [23].

Giovanola [25] took the concept of the one point bend a stage further and proposed the use of the so-called one point bend (OPB) test. In line with the findings of Böhme, he claimed that it is in many cases unnecessary to support bend specimen at high impact rates. Brittle fracture occurs in many cases before the anvil has interacted with the specimen. The applicability of the OPB test is limited by the maximum loading time and the maximum SIF, which are dependent upon the specimen dimensions, the material properties of the specimen and the impact velocity. Giovanola suggested the use of ballast at the end of the specimen to increase the maximum loading time and the maximum SIF.

Peuser [26] analyzed experiments performed by Böhme and Kalthoff [24, 21] on large epoxy specimens. He used a finite difference (FD) scheme as well as a beam model. The measured striker load was used as an input into both models. Peuser was the first who included the anvil stiffness into a model of the TPB impact test. The supports were modeled as linear springs, which can only be subjected to compression. This was based on the importance of the anvils in the impact process, which was reported by Böhme [21]. In agreement with the experiment, Peuser found that the specimen first moves away from the supports, then it impacts on the support and bounces back again. This was observed for rather short specimens with a length to width ratio of $L/W = 4.1$. A beam model with 2 beams connected with a hinge and a torsion spring was also applied. The supports were again modeled as springs and the anvil stiffness was determined experimentally. The stress intensity factor was calculated from the angular distortion from the center of the beam. This is equivalent to the proportionality of the SIF with the displacement at midspan (assuming a constant beam stiffness). Reasonable agreement with the experimental SIF was achieved with the beam model and the measured load-time curve as an input. The accuracy of the beam model was reported to become worse with increasing L/W ratio.

1.5.2 Determination of a transition time

Ireland [27] proposed the restriction of the range of applicability of the static load based procedure to times to fracture, which are larger than the duration of three oscillations of the measured striker load

$$t_f \geq 3\tau \tag{1.16}$$

with τ being the period of oscillations of the specimen, which can be approximated as

$$\tau = 1.68\frac{S}{c_b}\left(\frac{W}{S}\right)^{\frac{1}{2}}(EBC_s)^{\frac{1}{2}} \tag{1.17}$$

where S is the support span, W is the specimen width, B is the thickness, E is the elastic modulus, C_s is the specimen compliance and c_b is the bar wave speed. This time of 3τ was considered as a transition time to separate the initial, dynamically influenced

time from the time, when a quasistatic procedure can be applied. Kalthoff [23] showed that this criterion does not hold in all cases. Depending upon the test conditions (like the contact stiffness) and the specimen geometry the transition time for using the static procedure can be significantly longer than 3τ, as it can be seen in Figure 1.7. What is

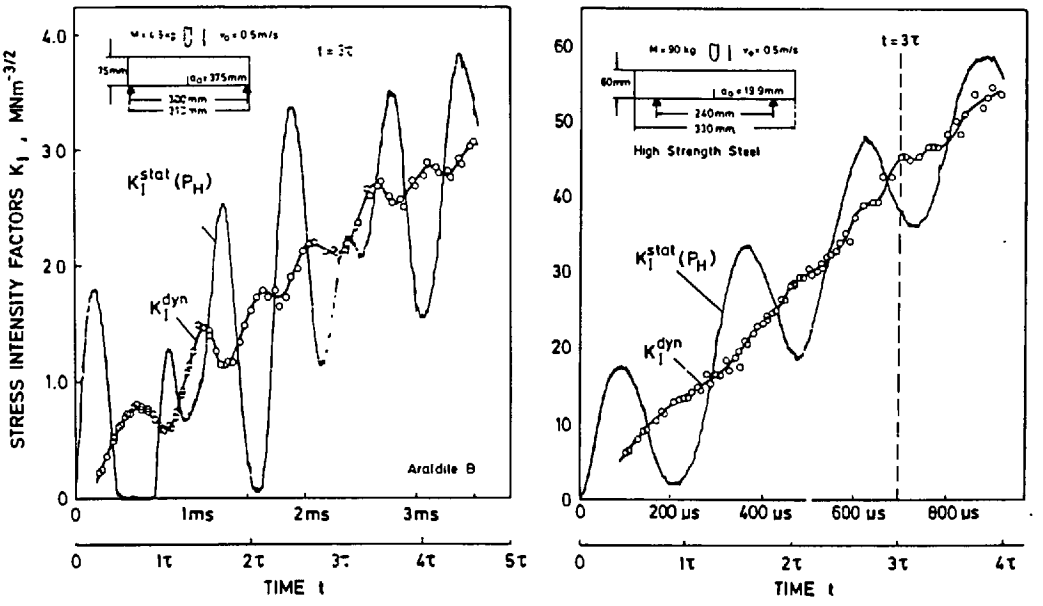

Figure 1.7: Stress intensity factors for two different experiments. From [23].

also obvious in the diagrams is that the dynamic effects at the crack tip (K_I^{stat} in Figure 1.7) are much lower than the dynamic effects in the striker signal (K_I^{dyn} in Figure 1.7) and that they decrease faster to an insignificant level. Böhme [28] presented transition times for different specimen geometries based on SIF measurements at the crack tip. These transition times are for most specimen geometries smaller than the transition time proposed by Ireland. The disadvantage is that, although the dynamic effects have fallen within the $\pm 10\%$ envelope and no dynamic correction needs to be applied, the SIF has to be evaluated at the crack tip, which means that instrumentation of the specimen is still necessary in most cases.

1.5.3 The time to fracture approach

For highly dynamic tests Kalthoff [29, 30] introduced the concept of impact response curves. For fixed test conditions such as striker geometry, impact velocity, specimen material and geometry a unique relationship between dynamic fracture toughness and time can be found. Kalthoff called this fracture toughness-time relationship impact response curve. It depends only on the elastic reaction of the specimen-striker system. Initially these curves were determined with caustics in reflection mode [29] on large

steel samples. In [30] a calibrated crack tip strain gauge was used to determine these curves. Once such impact response curves are known, they can be used to obtain the dynamic fracture toughness from the time to fracture only. This is illustrated in Figure 1.8. This technique can be applied to any material with the same material

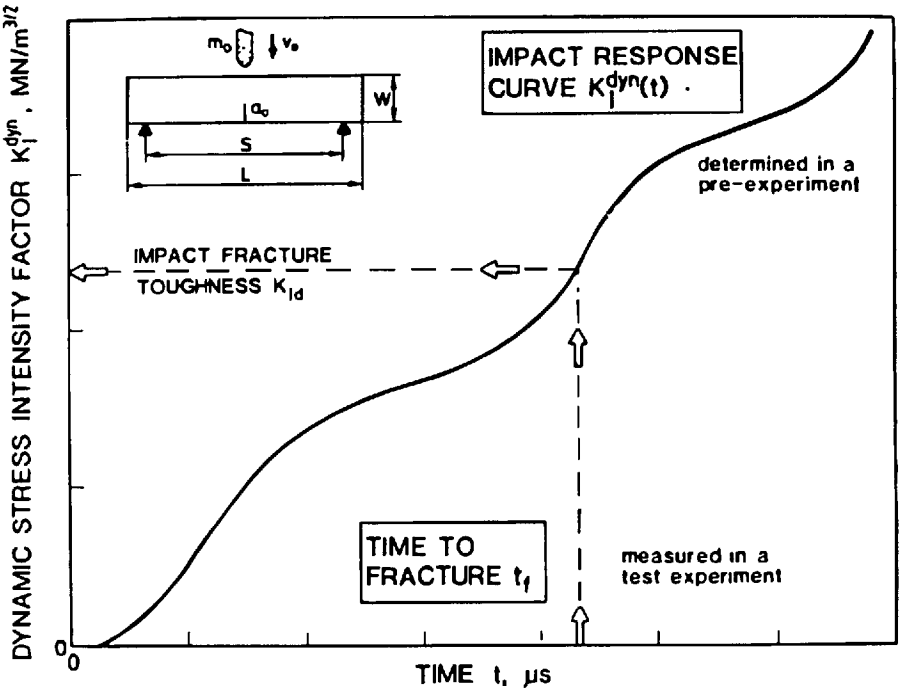

Figure 1.8: Determination of the dynamic fracture toughness by the impact response curve concept. From [30].

properties (E, ν) under the same impact conditions. The use of this technique was especially proposed for steels. The concept of impact response curves (IRC) [29] is also applicable to the one point bend test. Giovanola [25] proposed measuring the IRC with a calibrated strain gauge or directly with the elastic singularity solution of the crack tip strain field measured with a strain gauge. The advantage of the IRC method is that time to fracture can be measured quite easily without the need for calibrated strain gauges. Kalthoff [29] proposed the use of two uncalibrated strain gauges. One gauge is located on the striker and records the time of contact between striker and specimen. The other gauge is placed on the specimen close to the crack tip and records initiation. This technique avoids the necessity of calibrating the striker and especially each specimen. The disadvantage of this method is that for each testing condition a new impact response curve is needed, which involves exact measurements with calibrated strain gauges.

Böhme [24, 31] took the concept of impact response curves further and introduced a nondimensional time X with

$$X = \frac{c_l t}{W} \tag{1.18}$$

where t is the time and c_l is the longitudinal wave speed. He determined experimentally a dynamic correction function

$$k_d = \frac{K_d}{K_{st}} \tag{1.19}$$

with the dynamic SIF K_d and the static SIF K_{st} for several specimen geometries (Figure 1.9) with caustics. The advantage of the concept is the normalization of time with

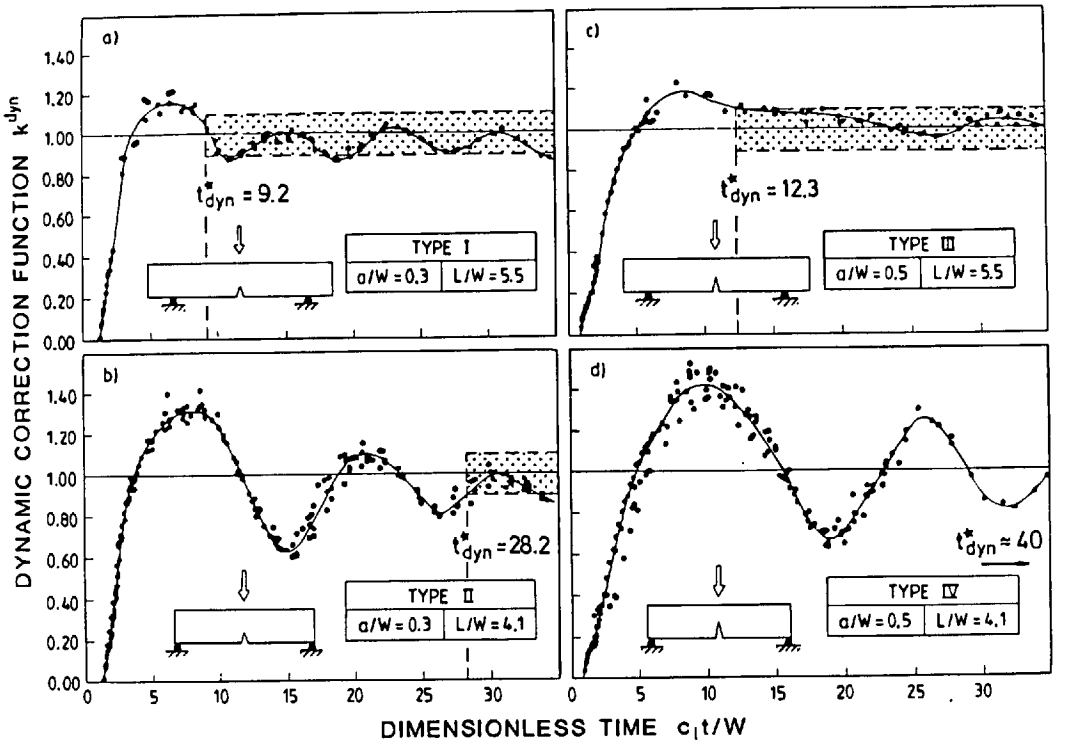

Figure 1.9: Dynamic key curves for 4 different specimen geometries. From [28].

respect to wave speed and width. The curve remains the same for materials with different elastic properties i.e. different wave speeds as well as for different specimen widths, as long as the specimen proportions are held constant. Böhme called these dynamic correction functions dynamic key curves. Looking at the curves in Figure 1.9 it is easy to see that some specimen geometries are more favorable than others. The transition time for the dynamic correction function to fall within the $\pm 10\%$ envelope is the lowest for specimen of Type I. This favorable specimen geometry has a span to width ratio of $S/W = 4$, a length to width ratio of $L/W = 5.5$ and a notch length ratio of $a/W = 0.3$. The highest transition time is observed for Type IV, which has a transition time more than 4 times higher than Type I. Apparently longer specimens

with $L/W = 5.5$ give a much better response with less dynamic effects than shorter specimens with $L/W = 4.1$.

In order to calculate K_d with the dynamic key curve concept the time to fracture has to be measured. This can be done the same way as proposed for the impact response curve method. The dynamic fracture toughness is calculated [31] from

$$K_d = K_{st} \cdot k_d(X = c_l t_f / W) \tag{1.20}$$

with the dynamic correction function value evaluated at the time to fracture, t_f. The static fracture toughness K_{st} is evaluated [31] with

$$K_{st} = \frac{f}{\psi} \frac{E}{W^{\frac{1}{2}}} \frac{V t_f}{(1 + C_m/C_s)} \tag{1.21}$$

where V is the impact speed and ψ is the dimensionless specimen compliance after Bucci [32] with

$$\begin{aligned} \psi = 0.24 \left(\frac{S}{W}\right)^3 \left(1.04 + 3.28 \left(\frac{W}{S}\right)^2 (1+\nu)\right) + 2 \left(\frac{S}{W}\right)^2 \left(\frac{a}{W}\right) \\ \left(4.21 \left(\frac{a}{W}\right) - 8.89 \left(\frac{a}{W}\right)^2 + 36.9 \left(\frac{a}{W}\right)^3 - 83.6 \left(\frac{a}{W}\right)^4 + 174.3 \left(\frac{a}{W}\right)^5 \right. \\ \left. -284.8 \left(\frac{a}{W}\right)^6 + 387.6 \left(\frac{a}{W}\right)^7 - 322.8 \left(\frac{a}{W}\right)^8 + 149.8 \left(\frac{a}{W}\right)^9 \right) \end{aligned} \tag{1.22}$$

and the specimen compliance

$$C_s = EB\psi \tag{1.23}$$

where B is the specimen thickness and C_m is the machine compliance. The static fracture toughness is, in this case, computed via an equivalent load calculated from the displacement and the compliance. Thus Equation 1.21 is equivalent to Equation 1.12 with the difference that in Equation 1.21 the machine compliance is taken into account.

1.5.4 Models of the TPB test

Numerical models with FE or FD can achieve a good match between the model predictions and the experiment, but they do not provide much insight into the physical process involved. Moreover, an analytical solution provides some understanding of the influence of the various parameters involved in the test [33]. A simple analytical model is also very useful for a straightforward evaluation of test results. That is why many studies have been undertaken to find appropriate analytical models. Various models have been developed for the dynamic TPB test.

1.5.4.1 Force input models

Many models use the measured force signal as an input to calculate the SIF response at the crack tip. Several of them were already mentioned [16, 26, 20, 22] in Section 1.5.1. The disadvantage of all force input models is that they require an accurate measurement of the force-time record. Furthermore, the point of initiation cannot be accurately detected from the load signal at high rates [19]. This means that expensive instrumentation of the specimen is necessary.

Marur [34] calculated the dynamic SIF response of the TPB specimen to the experimental load with a FE model with beam elements. A linearized anvil contact stiffness was used. The agreement with the experimental SIF history was better for short beams than for beams with an overhang. For short times the agreement is not good, presumably because the beam elements do not capture the dynamic stress field at the crack tip accurately. The anvil reaction was modeled quite accurately.

Rokach [35] developed a hybrid experimental/numerical method. He established a relationship between the SIF, the recorded striker load, the recorded anvil load and the specimen response via a convolution integral and a unit step function. The nonlinearity of the contact zone is thereby included in the force signal. The impact DSIF response functions can be derived analytically or numerically. Numerically it can be obtained with a FE model and a unit step load. Another possibility is to use the modal superposition method. Eigenfrequencies and weight coefficients were calculated from a FE model for this purpose. If the first eigenfrequency alone is used the model coincides with Kishimoto's solution [20]. Rokach [36] showed that the higher modes are important at short times.

Weissbrod [37] developed a procedure for short Charpy specimens. The dynamic SIF was determined with a convolution integral using the measured force signal. The response of the sample to a unit impulse is calculated with the finite element method. A fracture gauge or a strain gauge is used in this procedure to determine the instant of fracture. This means that instrumentation of the specimen is necessary and a calibrated loadcell is also needed, as the accuracy of the measured force directly affects the SIF result.

1.5.4.2 Load-point displacement models

These models are complete models in the sense that, assuming a linearly changing displacement, i.e. a constant velocity, the whole impact process is modeled. Except for the impact velocity, no measured data are needed.

Williams [38, 39] developed a one mass two spring model with the specimen mass, the contact stiffness and the specimen stiffness. This one degree of freedom model allows

the calculation of a dynamic correction function for G as well as for the SIF. It shows a significant dependence on the contact stiffness.

A one degree of freedom model with the specimen modeled as an Euler-Bernoulli beam developed by Williams [40] includes the contact stiffness and higher modes of the specimen. The contact stiffness is modeled as a linear spring. A rigid hinge connection between the specimen and the anvil is used. A procedure is proposed to calculate the contact stiffness from Hertz's solution and the beam model. In analogy with Equation (1.19) a dynamic correction function for the energy release rate, g_d, is defined in [40] as

$$g_d = \frac{G_d}{G_{st}} \tag{1.24}$$

where G_d is the dynamic strain energy release rate and G_{st} is the static energy release rate.

Using a 2D FE program, Marur [41] found a significant influence of the specimen overhang, when $L > S$, on the SIF-time curve. If the anvil node was fixed in the computations, the influence of the overhang vanished. This is sensible, as the vibrational pattern is forced to be the same by fixing the nodes.

In [42] Rokach used a 2D FE model with the commercial program ADINA with a linearized anvil contact stiffness. Computing the anvil force, he showed that the assumption of a permanent contact between specimen and support is invalid. Rokach claimed that there is only a small influence of the way the linearization of the contact stiffness is performed on the SIF results. He also found that the contribution of higher modes is only important for $L/S > 1$. He proposed that for a Charpy type specimen with $L/S = 1.375$ the first two eigenmodes should be used.

An analytical model with the specimen modeled as rigid body halves with a hinge for the process zone was developed by Orynyak [43]. The SIF was calculated from the angle of the hinge. Springs were placed between striker and specimen and between specimen and supports to account for contact effects. Some disagreement with measurements was found. This was due to the simplification of the specimen halves which were modeled as rigid bodies.

Marur [44] developed a 2DOF 2 mass, 2 spring, 2 dashpot model for the TPB test, which he solved numerically. The SIF was taken to be proportional to the force in the spring representing the specimen. Marur showed that there is considerable influence of the contact stiffness ratio (contact stiffness divided by specimen stiffness) on the beam response.

A model with an elastically constrained free-free Timoshenko beam was proposed by Marur in [33]. To include the effect of the overhang, the full length of the beam was modeled. The supports were modeled as springs, active only in compression. The model

has 2DOF, the rigid body translation mode and the fundamental bending mode. The displacement was applied through a linear spring, representing the contact stiffness. The impact process was divided into two phases: the free phase and the constrained phase, as the specimen gains contact with the supports at a defined period of time. Relatively good agreement with experimental data was achieved for short specimens with $L/W = 4.1$. For long specimens with $L/W = 5.5$ the model does not predict the SIF-time dependency satisfactorily. Marur believed that this is due to the influence of higher modes. The influence of higher modes for longer specimen was also reported by Rokach [42].

A 3DOF model for the OPB test was developed by Marur in [45]. A dynamic analysis of the OPB test was performed with the impactor modeled as a point mass with an initial velocity acting on the specimen, which is represented by a Timoshenko beam. Only the first vibrational mode is taken into account. Again, this model is reasonably accurate only for short beams, as otherwise there is a significant influence of higher vibrational modes.

Lorriot [46] and Landrein [47] proposed a 2DOF 2 mass 2 spring model to model the specimen and specimen-striker interaction. The specimen stiffness was modeled as a spring with the stiffness of a notched Timoshenko beam. The agreement with experiments was not very satisfactory.

A 2D FE model with the contact effects taken into account was presented by Rokach in [48]. Striker and support were modeled as rigid cylinders. This is approximately true for brittle polymers, but for metallic materials the finite stiffness of striker and supports affects the contact stiffness. Good agreement with Böhmes dynamic key curve measurements from [24] was observed. Rokach found that the variation of the Poisson's ratio within a certain range does not affect the dynamic correction function greatly. He proposed using the bar wave speed, c_b for the nondimensional time to normalize out the Poisson ratio influence. Rokach also studied the influence of the specimen geometry on the oscillation pattern of the DSIF-time record. He found that oscillations are larger for shorter specimens. Rokach reported that the smallest dynamic effects were observed for $L/W = 5.0 - 5.5$ and $a/W = 0.3$. In the initial period the dynamic correction functions were found to be independent of the specimen length. This is expected because as long as no stress waves from the ends of the specimen have returned to the crack tip, the crack is unaware of the specimen length.

A linearized expression for the contact stiffness between a cylinder and a beam is derived by Rokach in [49] from 3D FE studies. A convolution type expression for the one point bend test in conjunction with the linearized contact stiffness leads to a simplified analytical expression for the DSIF time record. Only the first eigenmode is taken into account. With this simple model, the peak SIF and the time of the peak for a OPB test can be approximated. This is useful for planning OPB tests.

1.5.5 Instrumentation

Ireland [50] showed the importance of the experimental equipment for the TPB impact test. With limited frequency response equipment the recorded signals are distorted, since the high frequency parts of the signal are attenuated. The same applies if filtering of the data is performed. Equipment such as amplifiers should therefore have sufficient frequency response. Filtering should only be used in special cases and with a clear understanding of the overall effects of limited frequency response.

1.5.5.1 Strain gauges

Strain gauges are commonly used for the instrumentation of the striker as well as the specimen. They have a limited frequency response themselves. The frequency response of the strain gauge is dependent upon the gauge size. Smaller gauges have a better frequency response i.e. smaller rise times. For relatively small strain gauges of 3mm on steel the upper frequency bound is higher than 300kHz [51, 52]. This corresponds to a rise time smaller than $1\mu s$. Winkler [53] proposed to use the rise time instead of the upper frequency bound, as it is more descriptive and can be directly compared with time dependent changes in the measured signal. Assuming a first order behaviour the rise time can be calculated from

$$t_r \approx \frac{0.35}{f_g} \tag{1.25}$$

where f_g is the upper frequency bound. The capacity of the wiring and the following strain gauge amplifier further lowers the frequency response of the system [53]. The total rise time can be approximately calculated from

$$t_r \approx \left(\sum_i t_{r_i}^2 \right)^{\frac{1}{2}} \tag{1.26}$$

where t_{r_i} is the rise time of each device in the signal chain. The device with the slowest response in the signal chain is the limiting factor.

For direct measurements of the magnitude of the stress intensity factor from a strain gauge the placement of the gauge is very important. Dally [54] investigated the influence of strain gauge placement on the accuracy of the SIF measurement. The SIF is obtained with strain functions expressed as infinite series. These series can be truncated when a certain amount of error is accepted. Dally found that there are three regions for strain gauge placement. Region 1 very near the crack tip is invalid due to 3D and plasticity effects. The far field region 3 is invalid, as the truncated series does not describe the strain field. He therefore found a region 2 between region 1 and 3, where the truncated series solution represents the strain field to a given accuracy. Dally concluded that a

single gauge with proper placement and orientation can be used to measure the SIF with sufficient accuracy.

1.5.5.2 Displacement measurement

Instead of measuring the striker load or the strain close to the crack, it is also possible to measure the displacement. Marur [34] found that the load point displacement is less sensitive to test conditions than the striker load. Optical measurement systems are often used for such displacement measurements.

Lorriot [46] and Landrein [47] used a laser displacement system to measure the specimen displacement. The big advantage of such a system is that there is no need for instrumenting the specimen, which is very important for routine testing. It should be noted that the measurement system used by Lorriot and Landrein has a very limited frequency response.

Sharpe and Böhme [55] measured the crack tip opening displacement, CTOD, with 2 measurement points on opposite crack faces with a laser interferometer. Good agreement with a crack tip strain gauge was achieved.

De Luna and coworkers [56] used a high speed photography technique with 4 coupled CCD cameras to obtain the crack mouth opening displacement, CMOD, from the recorded images. From CMOD they calculated the DSIF.

If the specimen is loaded with a Hopkinson bar, the impact velocity, which is the first derivative of the displacement with respect to time, can be determined from the strain measured with strain gauges on the bar. Dutton and Mines [57] found that in the case of a specimen loaded with a Hopkinson bar the impact velocity cannot be regarded as constant during the test. The displacement is therefore not linear with time.

Chapter 2

TPB Impact Tests

2.1 Introduction

As the main purpose of this work is to contribute towards a test standard for high rate TPB impact tests on SENB specimen, experiments with different materials were carried out to check the applicability of the test technique for these materials. The main value to be determined in such an experiment is the time to fracture. As there were some doubts about the practicability of a fracture time based approach the focus of the experimental work was on the accurate determination of fracture time. A round robin was conducted within ESIS TC4 as a part of this project to obtain experience from different labs with the test technique and improve the test procedure. First the results from the author will be presented. The results from the labs taking part in the round robin will then be compared with the results from the author.

2.2 Experimental

Three materials were tested for this work; polymethylacrylate (PMMA), unplasticied poly-vinylchloride (PVC) and medium density polyethylene (PE). All three materials were supplied in 10 mm thick sheets. A single edge notched bend specimen (SENB) geometry was used with a width, W, of 16 mm and a thickness, B, of 8 mm. The span, S, was 64 mm, equivalent to a S/W ratio of 4. The length of the specimen was 88 mm, equivalent to a L/W ratio of 5.5, which was found to be the best ratio to minimize dynamic effects [48]. The notch depth ratio a/W was chosen to be 0.3 for the same reason, so the precrack was approximately 4.8 mm long. Due to the different toughness of the materials, different notching techniques were applied. For the PMMA impact tapping in a special notching rig was used. The rig was designed to guide a razor blade perpendicular to the surface during the tapping process using a hammer. A precrack

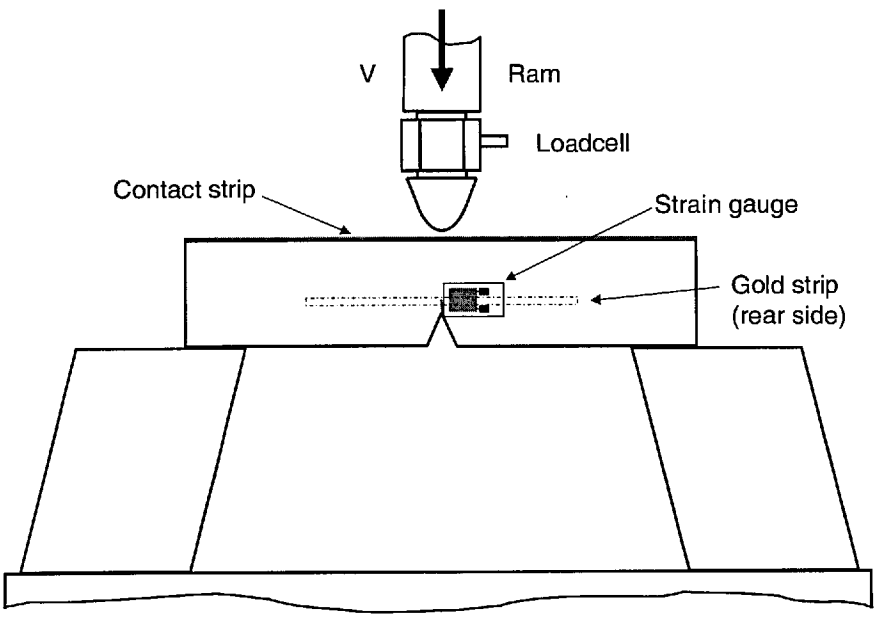

Figure 2.1: The TPB test setup.

could then be pushed ahead of the blade into the material in controllable small steps of around half a millimeter. For the tougher PVC and PE samples a notch was machined up to almost the final depth and then a razor blade was sliced across the bottom of the notch, generating a small, sharp extension of the notch. For both notching techniques a new razor blade was taken for each specimen. Heavy duty industrial blades were used to prevent big crack tip radii due to bending or breaking of the tip of the blade. The actual crack length was measured after each test under a microscope using a CCD camera and image analysis software. Five equidistant measurements over the thickness were taken and subsequently averaged.

The tests were conducted at room temperature using a 20 kN high speed servohydraulic testing machine (Model 1343, Instron Ltd.) with a maximum velocity of around 28 m/s. A displacement controlled mode was selected for testing and the test setup is shown in Figure 2.1. The specimens were tightly held in position with rubber bands on a three point bend fixture with flat supports. The load was applied with a titanium striker with a tip radius of 2 mm. A titanium alloy was chosen because it is very stiff with a low density. The load was measured by a 2.2 kN piezoelectric load cell (208A03, PCB Piezoelectronics Inc.). The natural frequency of the striker-load cell combination was measured as 28 kHz. A very thin layer of gold with a thickness less than 1 μm was sputtered on the top face of each specimen with a sputter coater designed for coating electron microscope samples. A voltage of 5 V was applied to the contact strip. In case of contact between specimen and striker a voltage step occurs due to earthing the

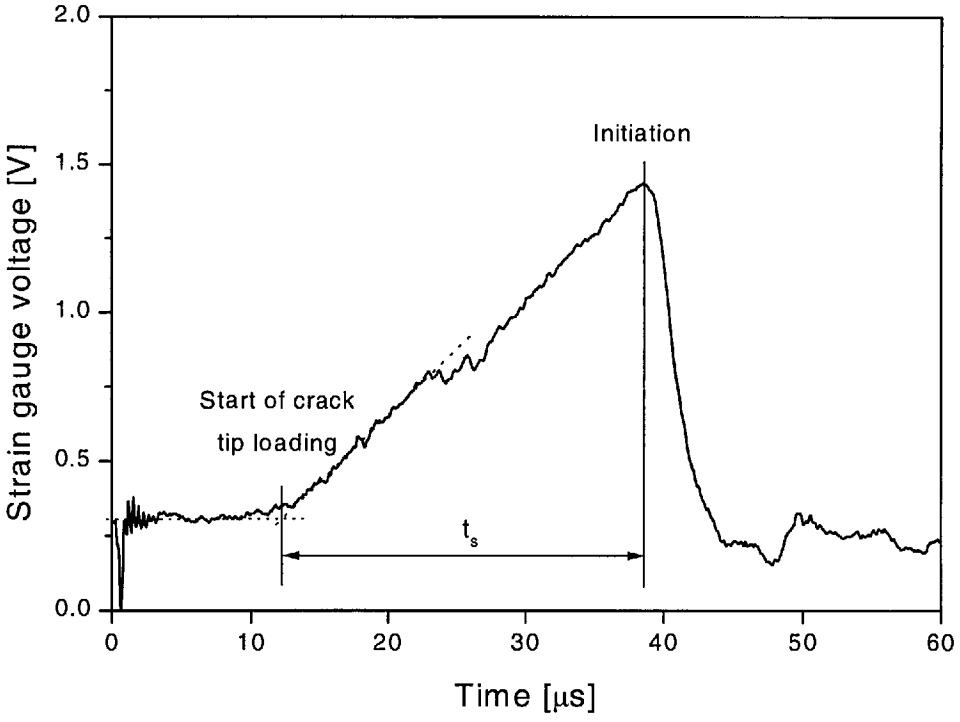

Figure 2.2: Time to fracture determination.

striker. This gives a very clear and fast indication of contact between specimen and striker. The same gold strip technique was also tried to measure the time of initiation via crack propagation on the sides of some specimens. A thin line (around 1 mm width) of gold was sputtered in front of the crack tip and when the crack propagated, the line was broken and a voltage drop occurred in a resistor in series with the gold strip. The aim behind this was to explore whether it is possible to avoid the expensive and time-consuming instrumentation using strain gauges and nevertheless measure the fracture time accurately. To measure crack initiation, a single 120 Ω foil strain gauge (CEA-06-032UW-120, Measurements Group Inc.) with a grid size of 0.7 × 0.7 mm was placed approximately 1 mm away from the crack tip. A fast 900 kHz strain gauge amplifier was used to to amplify the strain gauge signal. The signals from the load cell, the strain gauge and the gold strips were recorded by two 100 MS/s PC-based oscilloscopes (PS 200, Pico Technology Ltd.). The time to fracture, t_s, was taken from the strain gauge trace and Figure 2.2 shows how the time to fracture is measured from the strain signal. t_s was measured from the point where the strain signal started to rise to the peak value. Two straight lines were drawn to determine the former and the latter is taken as the highest point.

Table 2.1: Participating laboratories, abbreviations and test machines.

Laboratory	Abbreviation	Test machine
Cranfield University	CU	drop tower
ICI	ICI	drop tower
Imperial College	IC	servohydraulic
Politecnico di Milano	PDM	drop tower
University of Leoben	UOL	servohydraulic

2.3 The high rate round robin

As a part of this project a round robin within ESIS TC4 was performed [58]. ESIS TC4 is Technical Committee 4 from the European Structural Integrity Society (ESIS) dealing with Polymers and Composites [59]. This round robin is the second on high rate testing within ESIS TC4. The first round robin on this topic was performed in 1998 by Böhme [60, 61]. The aim of this second round robin was to check the feasibility of the experimental technique of measuring time to fracture at high rates of loading in a TPB test and also to improve the test procedure, which is given in Appendix A. Four other labs in Europe took part in this round robin, which can be found together with their abbreviation listed in Table 2.1.

The same materials as mentioned in Section 2.2 were tested in the round robin. The specimens for the round robin were machined at Cranfield University. The notching was done at Imperial College by the author the same way as the samples for the tests performed at Imperial College. This was done to ensure that differences in the results are not due to specimen preparation or notching, which can have a big influence on the results.

The participating labs used different test machines to load the specimens. Three labs used drop towers (Table 2.1), namely CU, ICI and PDM, whereas IC (see Section 2.2) and UOL used servohydraulic test machines. The drop towers from CU and PDM are spring assisted to generate a high test velocity without the need of a very high drop tower. Except for ICI all labs used a crack tip strain gauge to measure t_s as described in Section 2.2. ICI used a gold strip on the side of the specimen to determine crack initiation and the difference from the the contact strip rise to the initiation time was taken as t_s. A correction for the time for the stress wave to reach the crack tip was applied.

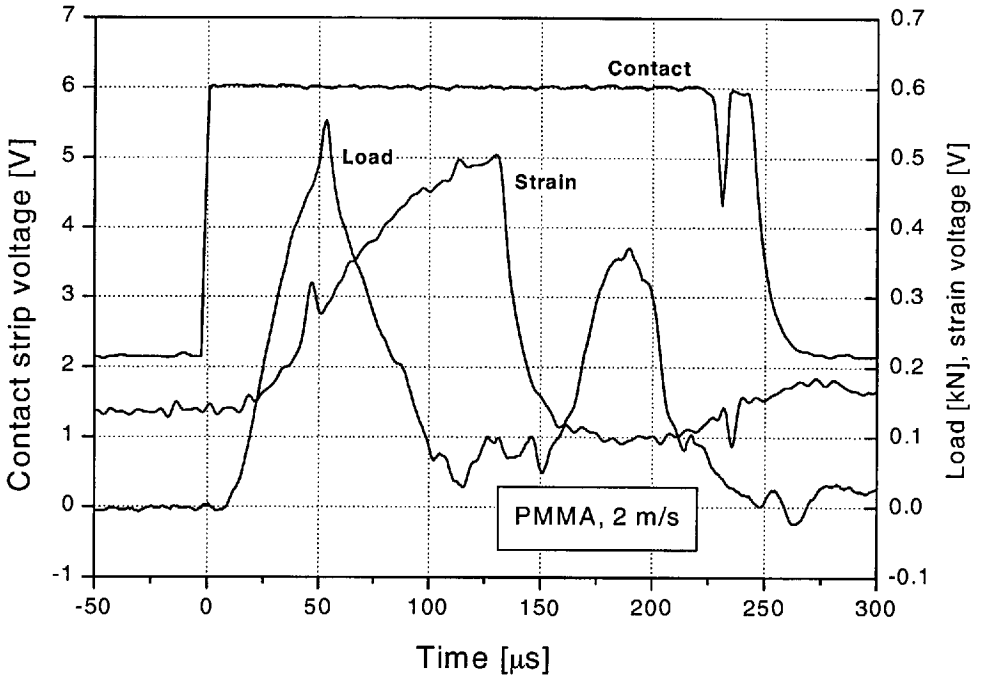

Figure 2.3: Test trace for PMMA at 2m/s.

2.4 TPB impact test results

Typical test traces for each material are shown in Figure 2.3 to 2.14. In the figures the signal from the gold line on the side of the specimen is called crack propagation, as it acts in a similar way to a crack propagation gauge. The other curves show strain, load and the signal from the contact strip on top of the specimen.

Typical test traces for PMMA are shown in Figure 2.3 to 2.5. At a velocity of 2m/s (Figure 2.3) the strain gauge signal is quite close to a triangular pulse which is due to the brittle nature of this polymer and a clear maximum point can be detected. The load has a minimum around 130μs, but no loss of contact is observed. Even at this comparably low velocity the load signal does not give a reasonable indication of the crack tip loading. The delay of the load signal due to the propagation time of the elastic waves in the striker to the loadcell is around 8μs. In Figure 2.4 test data for 4m/s is displayed. The strain signal is again fairly triangular with a sharp peak and a steep drop. The signal from the contact strip shows that specimen and striker stay in contact until and even after initiation occurs. Initiation happens during the inertia peak while the specimen is still accelerating. This is characteristic for high rate tests and brittle failure. Figure 2.5 shows a test at 27m/s and the strain signal is no longer triangular, but shows a maximum peak and then oscillations before it finally drops. These oscillations could be due to multiple initiation of the crack at different points of the precrack and subsequent crack arrest. The surface of the specimen breaks at the

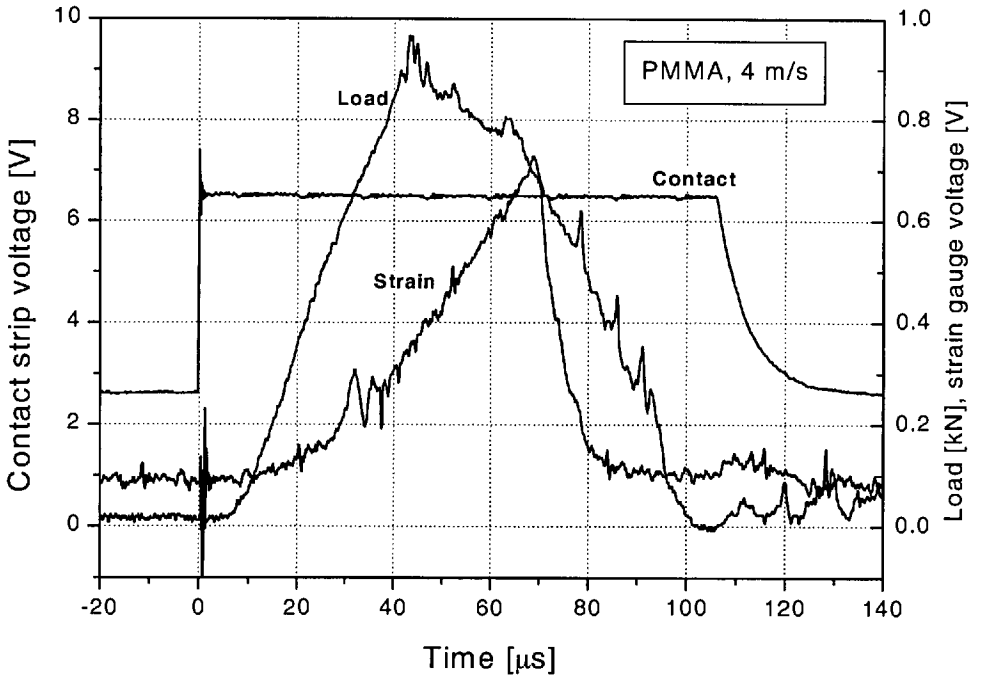

Figure 2.4: Test trace for PMMA at 4m/s.

point where the strain gauge signal finally drops, which can be observed in the signal from the crack propagation strip on the opposite side of the specimen. The first and highest peak is taken as the point of initiation. The initial spikes in the strain gauge and the crack propagation signal are caused by the steep change in the contact strip signal. This change induces a voltage in the grid of the strain gauge and in the gold line on the side of the specimen. Examples of test traces for PVC are shown in Figure 2.6 to 2.10. At a test velocity of 1m/s (Figure 2.6) the load and the strain signal show typical oscillations, which occur in a TPB impact test. The first peak in the load signal is the inertia peak from the acceleration of the specimen [18]. This first peak is only observed in the load signal, but not in the strain gauge trace. The subsequent oscillations in the load signal are due to flexural vibrations of the specimen. The amount of dynamic effects in the strain gauge curve is significantly smaller than in the load signal for this test. Crack initiation causes a steep drop in the strain signal. After a delay of around $10\mu s$ the load signal drops also. This time depends on the distance of the load transducer from the tip of the striker. Contact between specimen and striker is observed until $70\mu s$ after initiation. For PVC at 2m/s (Figure 2.7) initiation occurs during the second peak of the striker load oscillation. The specimen almost bounces off the striker at this velocity. At 8m/s (Figure 2.8) initiation occurs within the inertia peak. It would be a mistake to determine the time to fracture from the peak of the load signal, which has nothing to do with initiation. The gold line on the side of the specimen fractures $3\mu s$ after the peak in the strain gauge signal. At 16m/s there seems

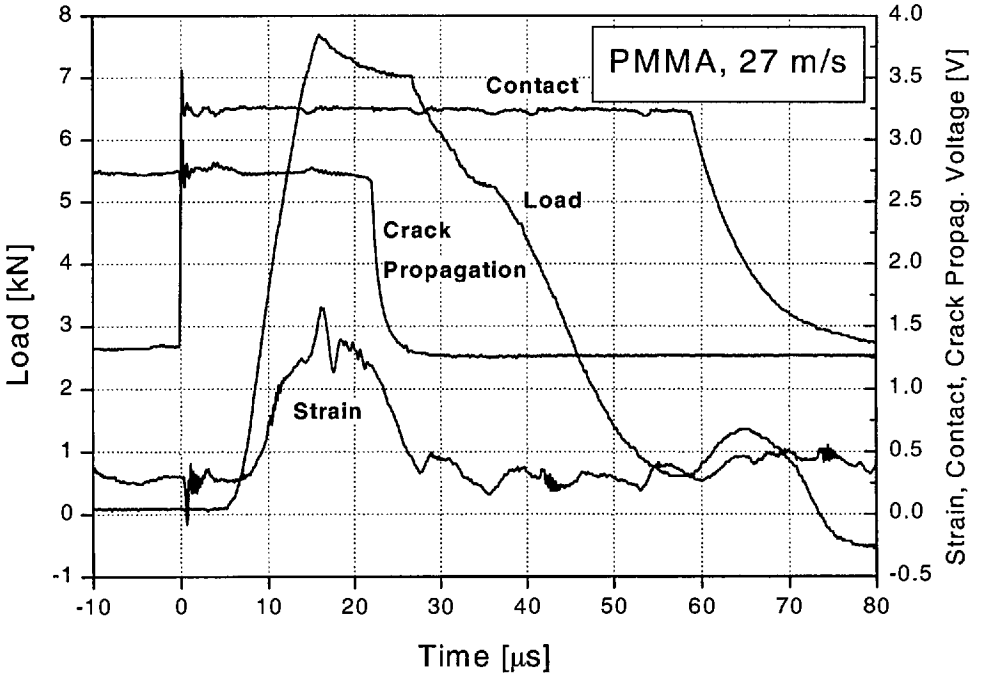

Figure 2.5: Test trace for PMMA at 27m/s.

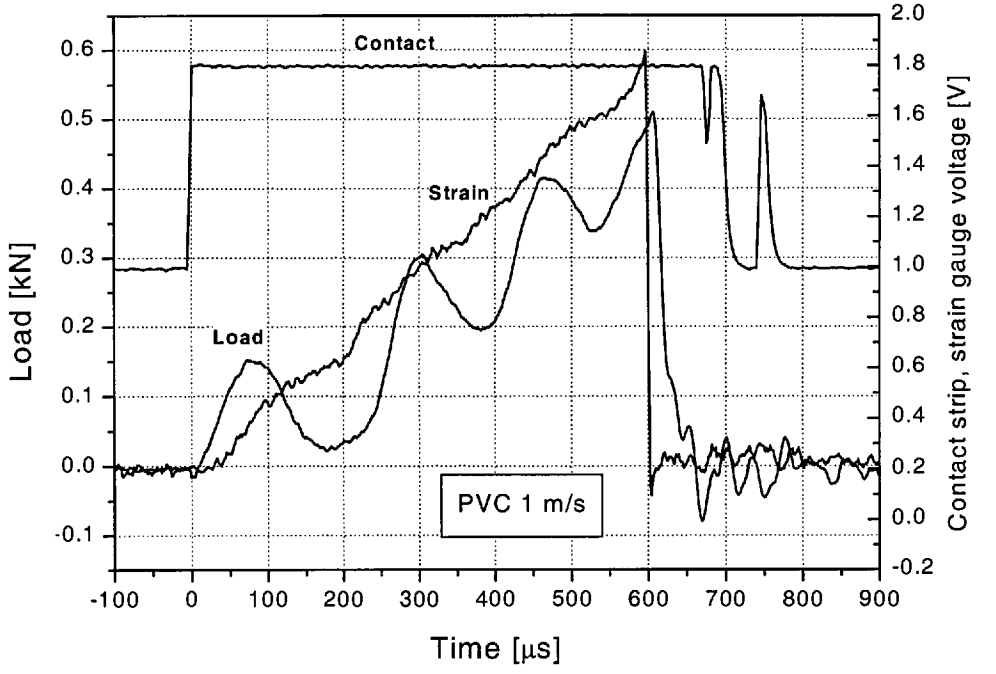

Figure 2.6: Test trace for PVC at 1m/s.

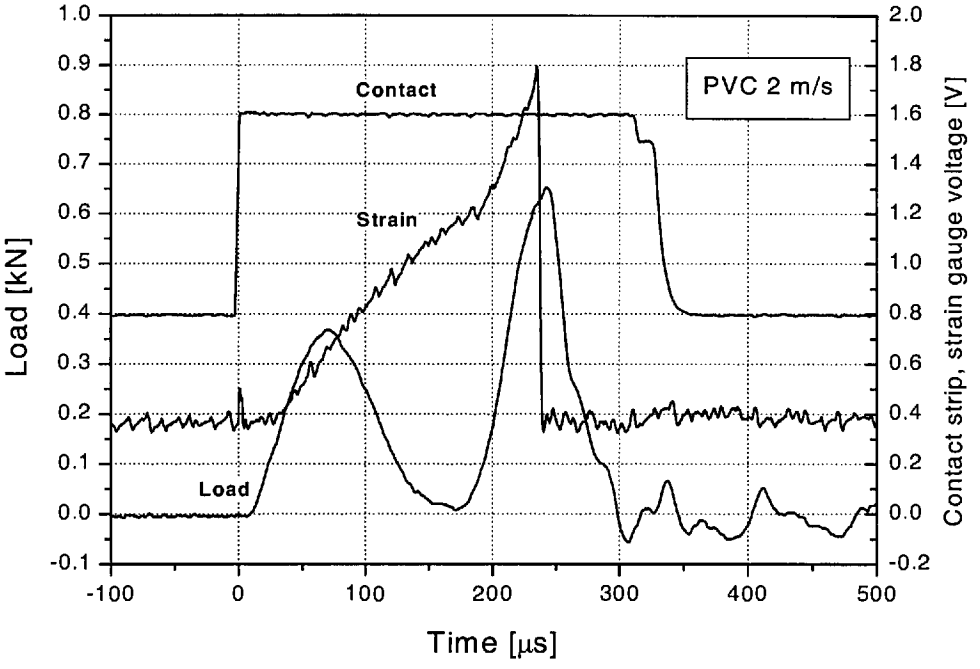

Figure 2.7: Test trace for PVC at 2m/s.

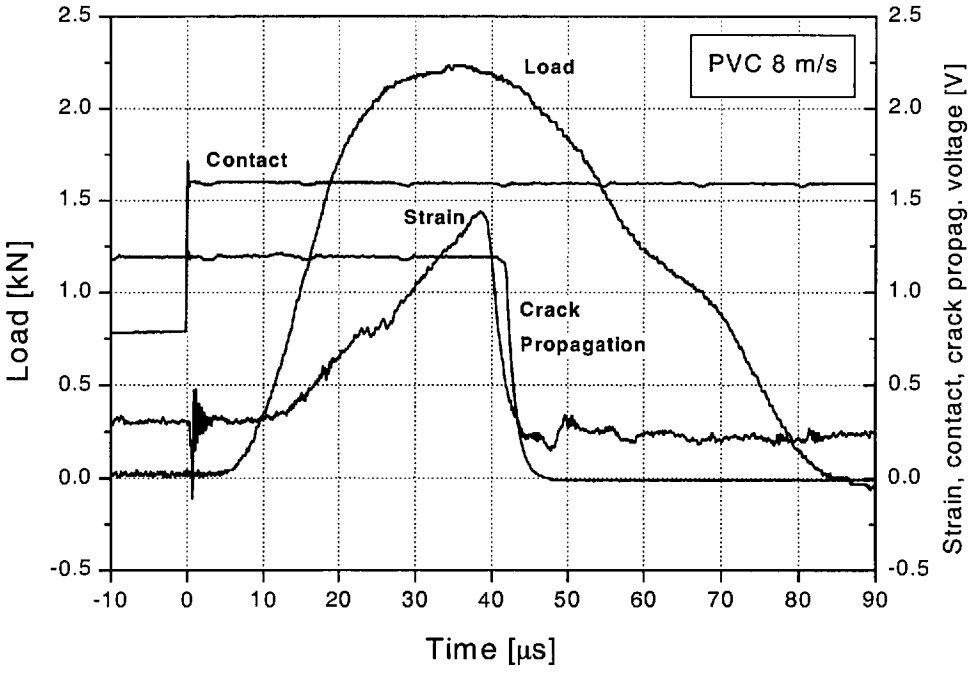

Figure 2.8: Test trace for PVC at 8m/s.

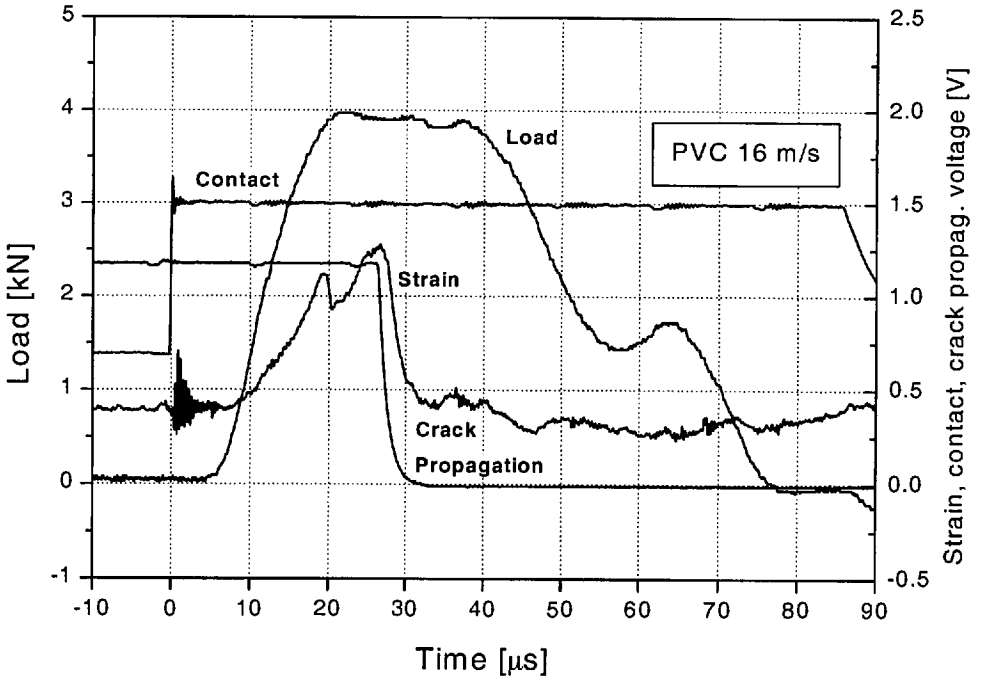

Figure 2.9: Test trace for PVC at 16m/s.

to be some plasticity in the contact area, as the load signal shows a plateau at the peak (Figure 2.8). The drop in the signal from the gold line coincides with the peak of the strain gauge signal for this test. Contact between specimen and striker is observed until initiation and for some 60μs afterwards. In Figure 2.10 a dataset for PVC at 27m/s is given and the strain gauge trace is almost triangular. There is again a remarkable amount of coincidence between the strain trace peak and the drop in the signal from the gold line on the specimen side.

Figures 2.11 to 2.14 give test traces for PE. The time to fracture measured by the strain gauge, t_s, is much longer than for tests with PMMA because of the ductile nature of PE. The slowly falling strain after initiation is representative of a slower falling crack propagation signal. It can be seen also that for this material the load signal does not give a reliable measurement of the actual crack tip loading at high velocities (> 2m/s). In Figure 2.11 for PE at 1m/s there is a considerable amount of plasticity. The oscillations in the load signal are small and they are damped out after a few cycles. The strain signal is also rounded, indicating plasticity. At 1m/s the drop in the strain signal coincides with a drop in the load signal due to the long fracture time. At 2m/s (Figure 2.12) a loss of contact can be observed between striker and specimen. This is the reason for a negative (tensile) striker load around 200μs. From the crack tip strain curves an embrittlement with increasing loading rate can be seen. From a rounded strain signal at 1m/s the shape changes to a steep drop at 2m/s. At 8m/s a plateau in the load signal is observed, which indicates plasticity between striker and specimen. The strain

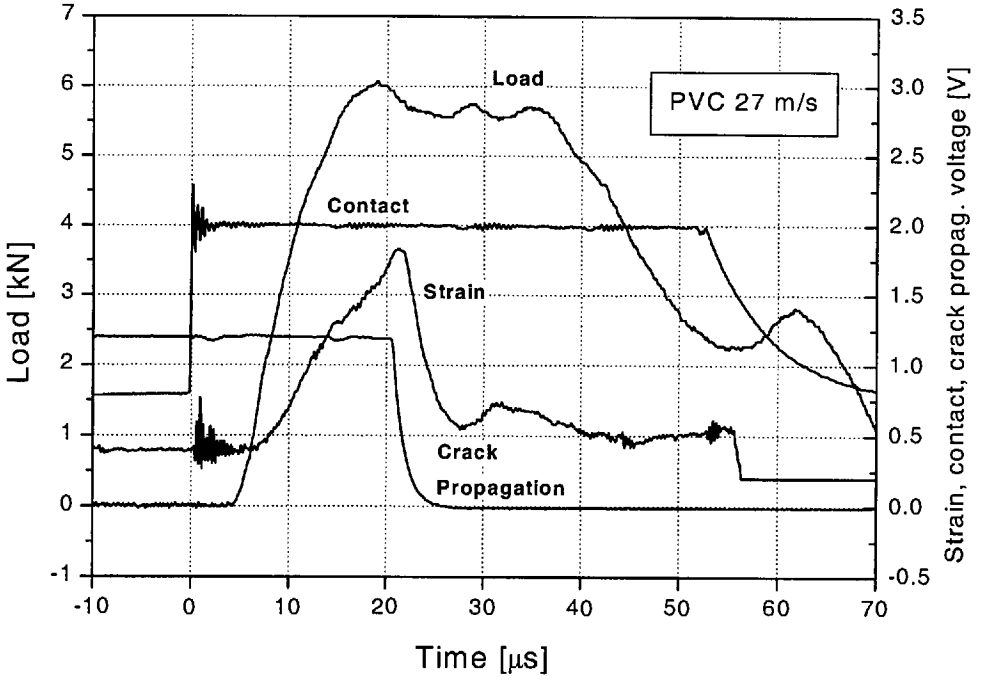

Figure 2.10: Test trace for PVC at 27m/s.

signal rises linearly with a rounded peak and decreases slowly. Due to a shorter time to fracture this decrease is even slower than the loading of the crack at 27m/s in Figure 2.14.

The signal from the gold line in front of the crack, whose signal is called crack propagation in the graphs agrees quite well with the peak of the strain gauge signal for PVC and PE. The time from the gold lines, t_g, as it was called, is measured from the rise of the contact strip signal to the drop in the signal from the gold line in front of the crack. The problem arising is that the time t_s, which is the time within which the stress at the crack tip reaches the initiation value, is measured from the point when the strain rises to the peak point before the final drop. Part of the difference between t_s and t_g is the traveling time of the stress wave to the crack tip. This assumes that the drop of the crack propagation signal coincides with the peak in the strain gauge signal. Another issue is the determination of the point where the crack propagation signal from the gold strip indicates crack initiation. For PMMA and PVC, which are quite brittle, a line was extrapolated from the linear falling part of the curve up to the extension of the constant value. The intersection of the two lines was taken as the point of initiation. In a ductile material as PE, the curve is much more rounded and therefore it is more difficult to determine the point of initiation with this method. A parabolic fit of the rounded part of the curve intersecting with the extension of the constant value would be a possible answer. The rounded part is thought to be due to two reasons. First the ductile nature of PE resulting in a plastic zone, which also affects the surface and can

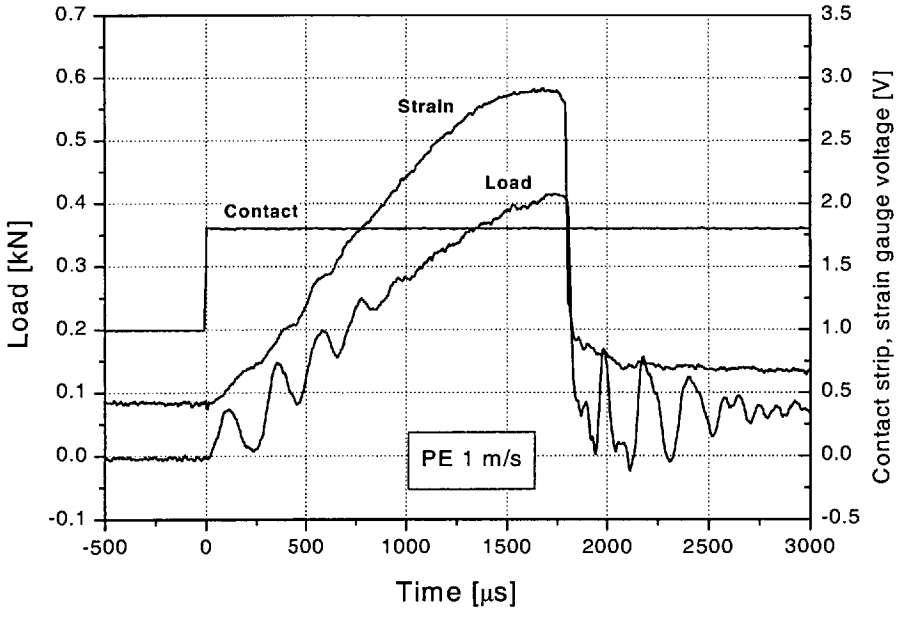

Figure 2.11: Test trace for PE at 1m/s.

lead to a slow breakdown of the very thin gold line. The other reason is the growth of shear lips on the surface of the specimen, which can be seen on the fracture surface. If the crack first grows inside the specimen and then subsequently the shear lips fail, this could explain the observed curve. This behaviour of PE was reported by Leevers in [62]. It can be seen from the graphs presented that the more brittle the material (e.g. PMMA), the bigger the dynamic effects. In a ductile material such as PE most of the energy is absorbed in the comparatively large plastic zone while in brittle materials stress waves are reflected backwards and forwards in the specimen without being immediately absorbed.

In this work the gold lines on the side of the specimen were only used to compare initiation times determined from them to the results obtained with strain gauges to evaluate the potential of avoiding expensive strain gauges on the specimen and replace them with a gold line ahead of the crack tip. In order to be able to obtain t_s from t_g it would be necessary to subtract the time from the first contact to the time when the strain at the crack tip rises, but this time can only be calculated roughly. This time is basically the time for the transverse stress wave to reach the crack tip [13], but surface unevenness can cause electrical contact between the striker and the gold line before any significant load transfer. This could be the reason that the difference between the contact strip signal rise and the strain rise in the crack tip strain gauge is not equal to the time of the transverse stress wave to reach the crack. A further indication for

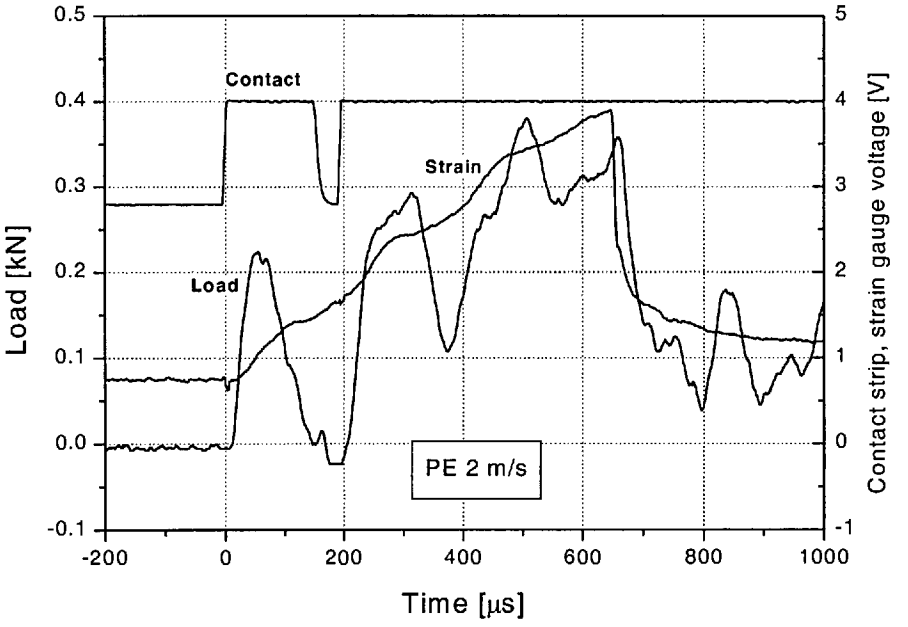

Figure 2.12: Test trace for PE at 2m/s.

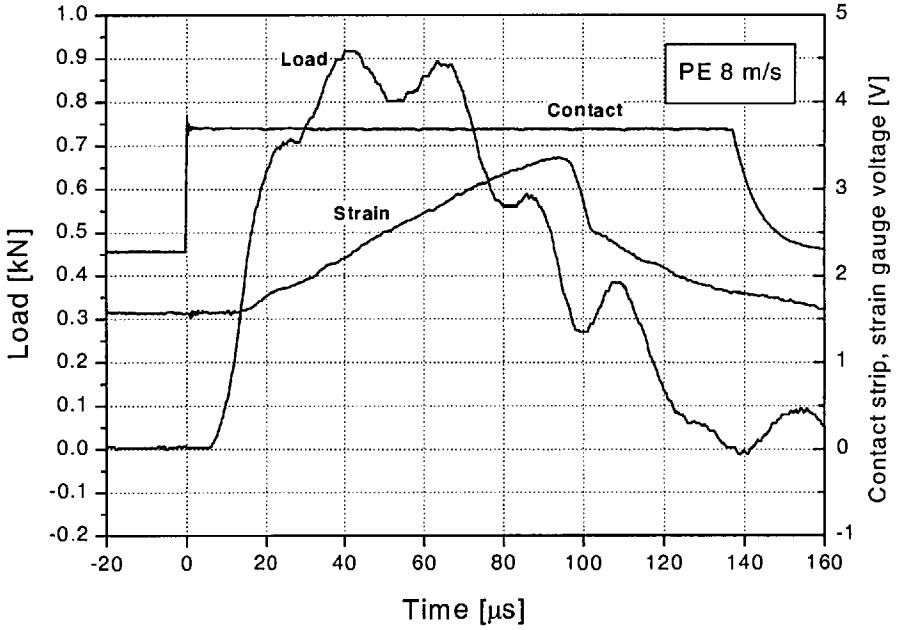

Figure 2.13: Test trace for PE at 8m/s.

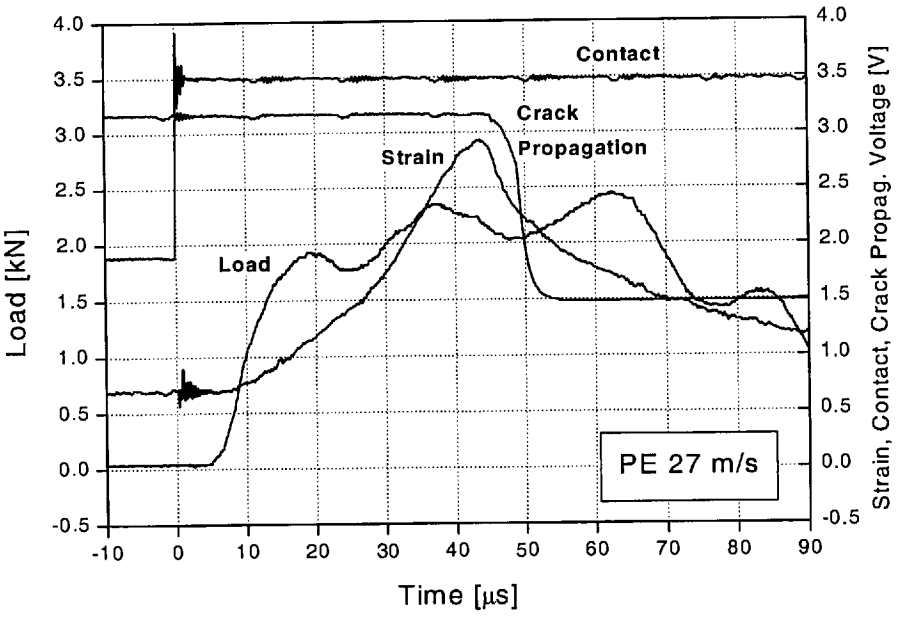

Figure 2.14: Test trace for PE at 27m/s.

surface unevenness as a cause of this difference is its velocity dependence. For higher velocities significantly smaller time differences between electrical contact of striker and specimen and the rise in the crack tip strain are observed.

For lower testing rates the difference between the assumed point of initiation between the crack propagation line signal and the strain gauge peak are relatively small, making it possible, cheap and easy to use as an alternative to crack tip strain gauges. Also the difference between the rise in the contact strip signal and the rise in the strain gauge signal is small compared to t_s for low velocities, but if necessary a correction for the time for the transverse wave to reach the crack tip can be applied. Gold lines on top of the specimen as well as on the sides of the specimen are then preferable.

Fracture times for the three materials tested versus test velocity are displayed in Figure 2.15. Data for an Epoxy from [40] was added also. The specimen dimensions for the tests on Epoxy were $6.5 * 13 * 71.5$mm so that the absolute values of fracture time are lower due to the smaller specimens. PMMA has the lowest time to fracture values of all three materials tested. The fracture time values for PMMA fall almost linearly in the double logarithmic plot with a slope of around -1.3. The slope of the decrease is leveling off at around 10m/s. The t_s values for PVC are in between those of PMMA and PE. Like PMMA, PVC also exhibits a slope of around -1.3 and a leveling off at around 10m/s. PE, which is the toughest polymer tested, exhibits the highest fracture time values for all velocities. Again, the slope is about -1.3 up to 10m/s. A prediction

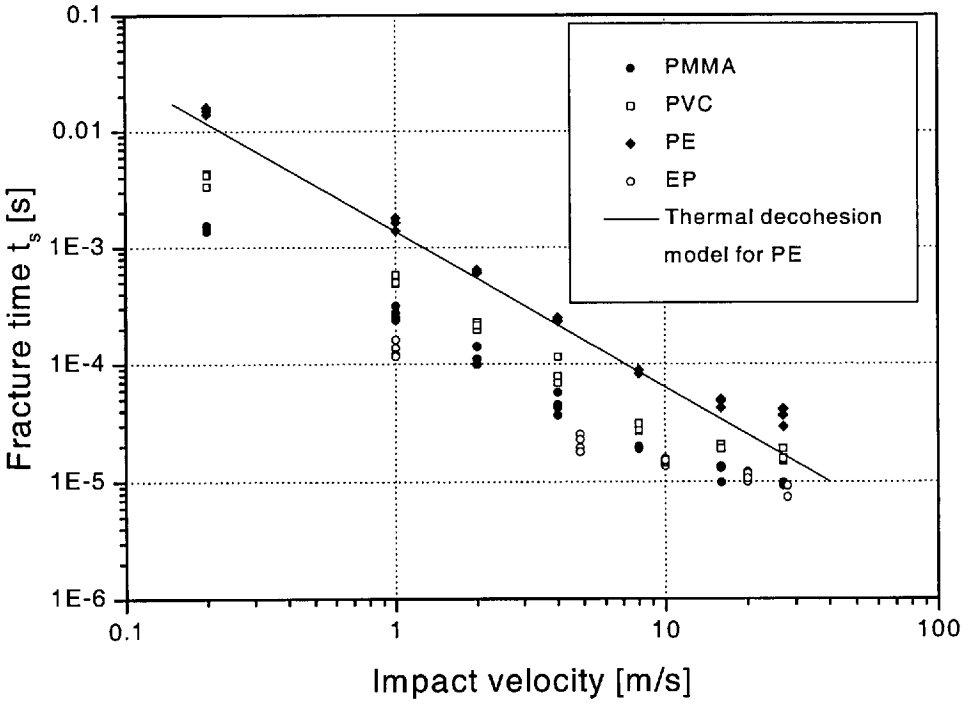

Figure 2.15: Fracture time versus impact velocity.

with a thermal decohesion model from [63] for the initiation time for PE was added in Figure 2.15. It shows quite good agreement with the experimental data, not only for the slope, but also for the absolute value. The slope is predicted by the model as $-4/3$. In Figure 2.16 all materials are displayed with shifted t_s values. This demonstrates that the $-4/3$ velocity dependence of the initiation time is valid for a wide range of materials and velocities. This is especially interesting as data from three thermosets is displayed as well in Figure 2.16. Epoxies C and D are rubber toughened Epoxies (15phr) with different curing temperatures [64]. They also show the same velocity dependence. Epoxy data from [40] is again added in this graph. At high velocities above 10m/s the slope becomes lower for all materials. The velocity when the values leave the $-4/3$ line varies with the material. This characteristic $-4/3$ slope can be explained from thermal considerations. At high impact velocities it is possible that the heat is trapped in a small zone around the crack tip due to the low thermal conductivity of polymers. For a given temperature rise, ΔT, in a small zone around the crack tip [65] and for G equal to G_c it is possible to write

$$G_c \propto \Delta T t_s^{\frac{1}{2}} \propto (Vt)^2 \tag{2.1}$$

and from that a proportionality between t_s and V can be derived as

$$t_s \propto V^{-\frac{4}{3}} \tag{2.2}$$

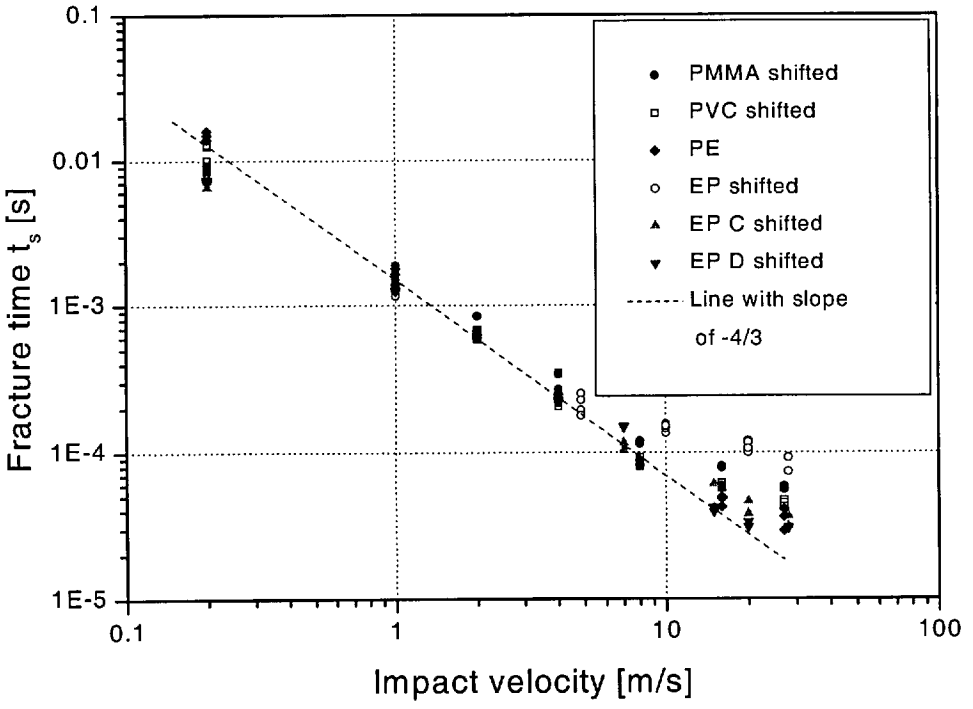

Figure 2.16: Shifted fracture time versus impact velocity.

which is the slope observed in the test data. This means that there are indications that the fracture of the tested polymers could be a thermal phenomenon at high impact velocities. At a certain material dependent threshold value the slope reduces. This could be due to a different process becoming dominant.

For the t_s results shown above a maximum standard deviation of 28% of the mean value was found for PVC at 4m/s. The typical value for the standard deviation of fracture time was found to be about 10% of the mean t_s value. In Chapter 7 the time to fracture results will be used to calculate K_d and G_d.

2.5 High rate round robin test results

The round robin test results are presented in Figure 2.17 to 2.20. The results from the author, which were presented in the previous section are denoted as IC in the round robin results. Results for PMMA are displayed in Figure 2.17. There are two sets of UOL results denoted as UOLA-s and UOLA-f. They were obtained with a slow strain gauge amplifier with 50kHz upper frequency bound in the case of UOLA-s and with a fast strain gauge amplifier with 1MHz upper frequency bound in the case of UOLA-f. There is a remarkable difference between these two. The slow amplifier increases the fracture time at high rates by more than 50%. This shows the necessity

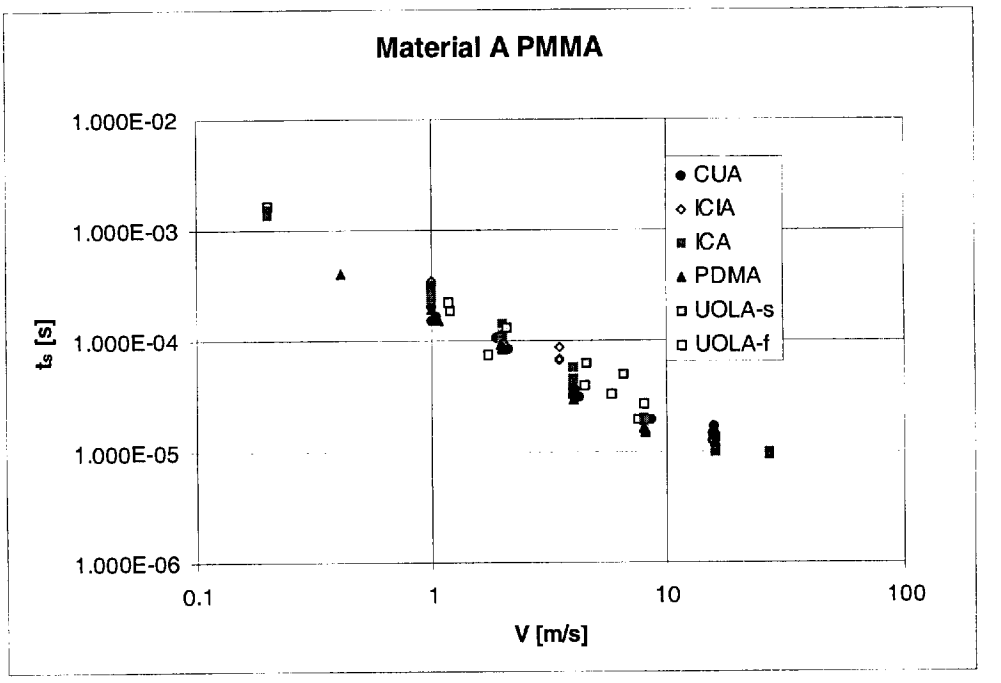

Figure 2.17: Fracture time versus impact velocity for PMMA.

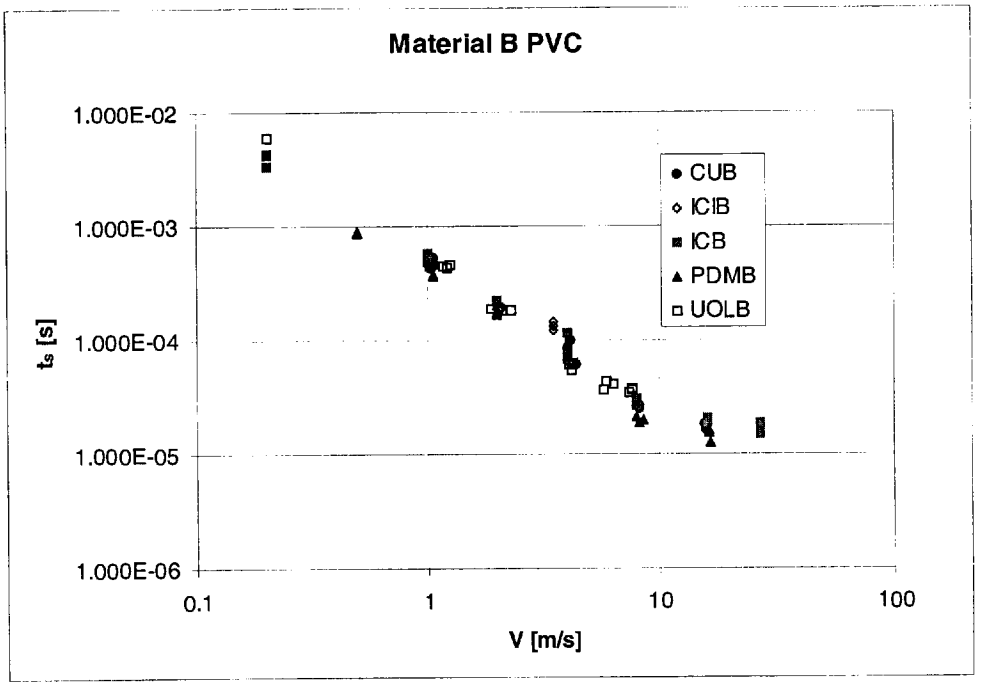

Figure 2.18: Fracture time versus impact velocity for PVC.

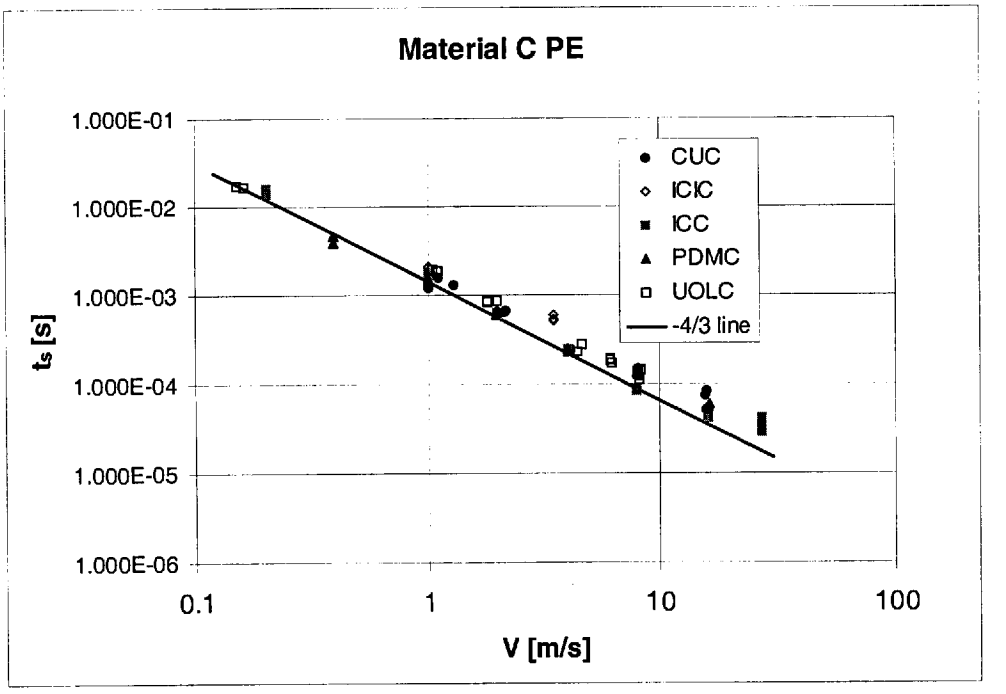

Figure 2.19: Fracture time versus impact velocity for PE.

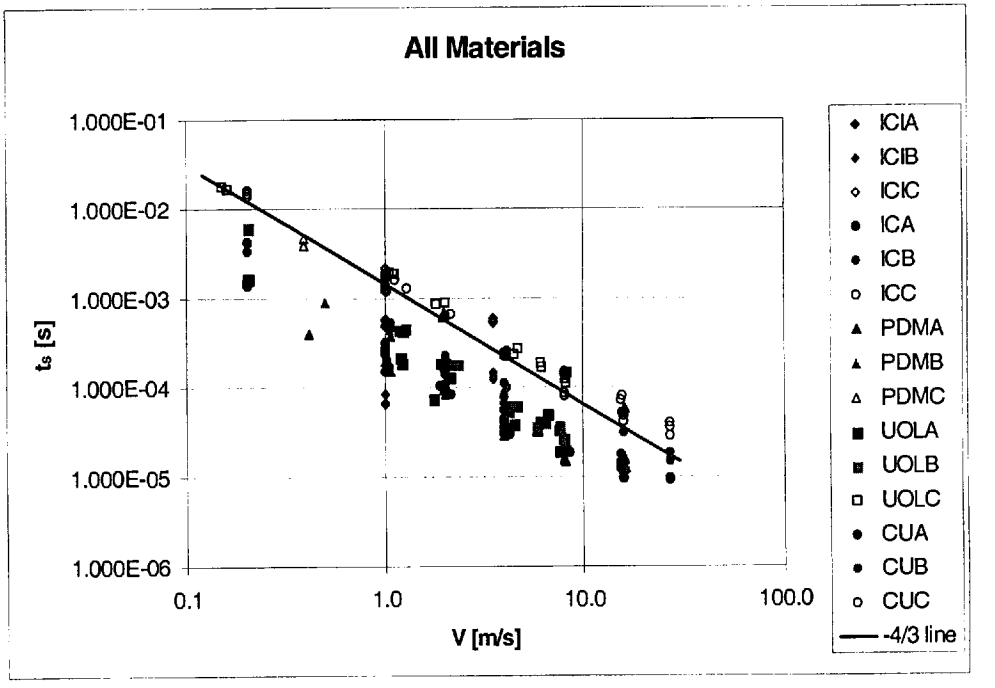

Figure 2.20: Fracture time versus impact velocity for all materials.

of fast equipment to obtain accurate results. The IC results for PMMA are in good agreement with the results from the other labs. The scatter for PVC (Figure 2.18) is lower than for PMMA. The values from ICI for PVC at 3.5m/s are slightly higher than the rest. PDM has the lowest values for t_s whereas the IC results are higher. The lowest scatter is observed for PE (Figure 2.19). The ICI results at 3.5m/s are higher, which is probably due to the way t_s is determined (from the gold lines). In comparison to the other labs the IC results for PE are low, especially at 8 and 16m/s and higher. All materials together are displayed in Figure 2.20. Again, it is remarkable that they all follow the $-4/3$ slope.

The results from the round robin are quite promising and the scatter is not too big for the second iteration loop i.e. the second round robin. It should be noted that there are usually 6 iterations necessary to obtain a test protocol which can be the basis for a ESIS standard [66]. The typical standard deviation for all materials was about 11% of the mean t_s value. The minimum standard deviation observed in the round robin for t_s was 1.2% of the mean value and the maximum was 29%. The results from the author were found to match well with the results from the other labs.

Chapter 3

Finite Volume Analysis Methods

3.1 Introduction

To attain a deeper understanding of the dynamics of the TPB test it is important to model the test accurately. With a dynamic contact procedure recently developed for the finite volume (FV) program used, the FV method is a powerful tool to analyze the TPB test, especially as one of the aims of this work is to investigate the influence of the contact stiffness on the test. The additional advantage of the FV program used is that the program allows full access to the code and therefore it is possible for the user to implement his own routines e.g. for the calculation of the SIF. As the main focus of this work is on the analysis of the TPB test, only a brief outline of the principles of the FV method is given here. Following that, the methods used in the FV analysis are described.

3.2 The FV method

The FV method is usually employed in computational fluid dynamics. Demirdzic [67, 7] applied the FV method for stress analysis and Ivankovic [68, 69, 70] applied it for the analysis of dynamic fracture problems.

The conservation of linear momentum is the basis of the FV method for stress analysis. In the case of dynamic equilibrium of an arbitrary part of a solid body of volume V bounded by a surface S the momentum equation expresses the balance of surface, acceleration and body forces. The momentum balance can be expressed as [69]

$$\frac{\partial}{\partial t}\int_V \rho\frac{\partial \boldsymbol{u}}{\partial t}\,dV = \int_S \boldsymbol{\sigma}\cdot\boldsymbol{n}\,dS + \int_V \rho\boldsymbol{f}\,dV \tag{3.1}$$

where t denotes time, $\boldsymbol{\sigma}$ is the stress tensor, $\boldsymbol{u}$ is the displacement vector and $\boldsymbol{f}$ is the body force vector. $\boldsymbol{n}$ is the unit vector of the outward normal to the surface S and ρ is the material density. The material is assumed to be homogeneous and isotropic. It is also assumed that the material is linear elastic and obeys Hooke's law

$$\boldsymbol{\sigma} = 2\mu\boldsymbol{\varepsilon} + \lambda tr\boldsymbol{\varepsilon}\boldsymbol{I} \tag{3.2}$$

where λ and μ are the Lamé constants and $\boldsymbol{I}$ is the identity tensor. The strain tensor $\boldsymbol{\varepsilon}$ is defined for small strains as

$$\boldsymbol{\varepsilon} = \frac{1}{2}\left[\nabla\boldsymbol{u} + (\nabla\boldsymbol{u})^T\right]. \tag{3.3}$$

With Equations 3.2 and 3.3 the momentum equation can be entirely expressed in terms of the unknown displacement vector $\boldsymbol{u}$ as

$$\frac{\partial}{\partial t}\int_V \rho\frac{\partial \boldsymbol{u}}{\partial t}\,dV = \int_S \left\{\mu\left[\nabla\boldsymbol{u} + (\nabla\boldsymbol{u})^T\right] + [\lambda\nabla\cdot\boldsymbol{u}\,\boldsymbol{I}]\right\}\boldsymbol{n}\,dS. \tag{3.4}$$

Equation (3.4) is still exact and the body forces are neglected.

Boundary conditions have to be specified at all boundaries of the solution domain. They can be either of Dirichlet type, which is a displacement boundary condition, specifying the displacement at the boundary, or of Von Neumann type, which is a traction boundary condition, where the boundary traction $\boldsymbol{t} = \boldsymbol{n}\cdot\boldsymbol{\sigma}$ is specified [67]. A mixed boundary condition is often required, where the normal component of the boundary displacement and the tangential component of the traction vector is prescribed [71].

In the FV method the solution domain is subdivided into a finite number of N contiguous non-overlapping control volumes or cells, with a computational node placed at its centre, where the value of the displacement vector components as well as the physical properties of the material are stored. This process is called spatial discretization. The control volume is defined by the coordinates of its vertices and it can be of arbitrary polyhedral shape with an arbitrary number of cell faces where faces of the i^{th} cell are denoted by $S_j, (j = 1, 2, ..., n_i)$.

The global conservation of momentum can now be expressed summarily for the entire solution domain as [70]

$$\sum_{i=1}^{N}\frac{\partial}{\partial t}\int_{V_i}\rho\frac{\partial \boldsymbol{u}}{\partial t}\,dV_i = \sum_{i=1}^{N}\sum_{j=1}^{n_i}\int_{S_j}\left\{\mu\left[\nabla\boldsymbol{u} + (\nabla\boldsymbol{u})^T\right] + [\lambda\nabla\cdot\boldsymbol{u}\,\boldsymbol{I}]\right\}\boldsymbol{n}_j\,dS_j. \tag{3.5}$$

To solve Equation (3.5), a coordinate system must be chosen and the displacement vectors have to be resolved into their components along the chosen coordinate directions. Cartesian coordinates are the best option. They offer a simple form of constitutive re-

lations and a strong conservative form of the momentum equations [67]. Furthermore, the integrals in Equation (3.5) have to be approximated and distributions of dependent variables and physical properties in space and time have to be assumed. A piecewise linear second order accurate approximation is adopted for the spatial distribution of the displacement field and the material properties. Like the space domain, the time domain is also discretized. The time is subdivided into an arbitrary number of time steps. An unconditionally stable first order accurate fully implicit temporal differencing scheme is employed. The integrals in Equation (3.5) are usually approximated by the second order accurate mid-point rule.

As a result of the FV discretization 3 mutually coupled sets of N nonlinear algebraic equations with 3 unknown displacement components are obtained for 3D problems. The equations are linearized and sets of equations for each dependent variable are temporarily decoupled. A system of linear algebraic equations is obtained for each displacement component. A segregated solution procedure is used to solve these equations iteratively [67].

Due to the equation segregation and the iterative solver the FV method is well suited for solving nonlinear problems efficiently [72]. This is important, as the contact between a cylinder and a flat body, which needs to be modeled in this work, introduces nonlinearity into the formulation.

3.3 The FV program: FOAM

A commercial FV package called FOAM (Field Operation And Manipulation) [73] is used in this work. FOAM is a C++ library of discretization routines, used primarily to create executables, which are called applications, that are designed to solve a specific problem in continuum mechanics [74]. FOAM is supplied with pre- and post-processing environments. One of the advantages of FOAM is that new applications can be created by its users, which gives it a high degree of flexibility. FOAM is programmed in an object-oriented manner. Provided the required objects and their functions and properties [75] are known to the user, they can be used to write specific routines efficiently.

3.4 The contact procedure

A newly developed contact procedure is used in this work, which was developed by V. Tropsa and A. Ivankovic, both from the Strength of Materials section of Imperial College. The procedure has been implemented in FOAM and it is based on fully implicit updating of the contact parameters: i.e. contact surfaces and forces. Due to its implicit nature the contact procedure is very accurate. The contact surfaces and

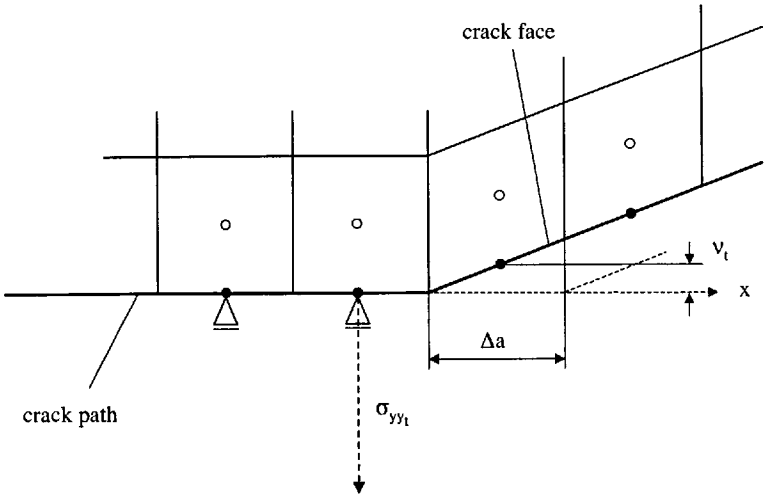

Figure 3.1: The crack tip closure method in FV.

forces are updated within each time step until convergence is achieved. A fine mesh in the contact regions is needed to obtain an accurate contact stress distribution. Local mesh refinement is therefore necessary. The procedure was used successfully in the dynamic analysis of the impact wedge peel test [76].

3.5 Local mesh refinement

A local mesh refinement procedure [77] was used within FOAM to increase the resolution at certain places, e.g. around the crack tip to obtain the SIF from the local stress field. The mesh refinement was also necessary for the contact procedure in order to have enough cells in the contact zones. The procedure used splits up a cell into four cells in a defined region. Repeated use of the procedure at certain places allows refinement of the mesh to the extent required.

3.6 Numerical methods for K and G calculation

3.6.1 The determination of G with the crack tip closure integral

The crack tip closure integral was introduced in Chapter 1. As mentioned there, this method is well suited for numerical routines and was used successfully in FE programs

[6, 8]. In the FV representation the crack tip closure integral is a work per unit area done by the forces which, if applied to 'cracked' cell faces, would close them back to their original position [7]. For computational purposes a cell size Δa is selected. It is convenient to keep the elements of the same size [6], which is easily achieved in the FV method. As the variation of the local stress field is small when the crack advances a short distance Δa, it can be assumed that the forces required to close the crack faces back are equal to the force at the crack tip cell and one can obtain [7]

$$G \approx \sigma_{yy_t} \nu_t \tag{3.6}$$

where σ_{yy_t} is the stress component in y-direction at the crack tip and ν_t is half of the crack tip opening displacement at the cell next to the tip (Figure 3.1). One of the big advantages of this method is the simplicity of the calculation. It also offers good accuracy even for coarse meshes [6, 7] i.e. the method is reasonably mesh insensitive. This saves computation time and it makes the crack tip closure integral a fast and economic method for the calculation of G. Equation (3.6) was implemented into FOAM to obtain G and, via Equation (1.4), the SIF.

3.6.2 The determination of G with the J integral

The dynamic J integral is a widely used method for the calculation of G in FE studies [78, 79, 8]. The J integral has the physical meaning of the energy release rate in elasticity. The advantage of the dynamic J integral is that it is path independent. For dynamic loading conditions and a stationary crack G can be calculated with a path independent J integral as [79]

$$G = J = \int_{\Gamma_0} \left(U n_1 - \sigma_{ji} n_j \frac{\partial u_i}{\partial x} \right) d\Gamma + \int_{A_0} \rho \frac{\partial^2 u_i}{\partial t^2} \frac{\partial u_i}{\partial x} dA \tag{3.7}$$

where the area A_0 is enclosed by the paths Γ and Γ_0 and the crack faces whereby Γ is shrunk on the crack tip (Figure 3.2). $\boldsymbol{n}_i$ is a unit vector normal to Γ or Γ_0 and that points away from the crack tip. n_1 is the component of $\boldsymbol{n}_i$ in x-direction. U is the strain energy density and $\boldsymbol{u}$ is the displacement vector. The material density is denoted as ρ and $\boldsymbol{\sigma}$ is the stress tensor. This form of the dynamic J integral is well suited for computational purposes, as it can be evaluated around any curve encircling the crack tip.

In a discretized form suitable for a FV program Equation (3.7) can be written as

$$G = \sum_{\Gamma_0} \left[\frac{1}{2} (\boldsymbol{\sigma} : \boldsymbol{\varepsilon}) (\boldsymbol{n} \cdot \boldsymbol{i}_x) - (\boldsymbol{\sigma} \cdot \boldsymbol{n}) \cdot (\boldsymbol{i}_x \cdot grad\boldsymbol{u}) \right] \Delta\Gamma + \sum_{A_0} \left[\rho \frac{\partial^2 \boldsymbol{u}}{\partial t^2} \cdot (\boldsymbol{i}_x \cdot grad\boldsymbol{u}) \right] \Delta A \tag{3.8}$$

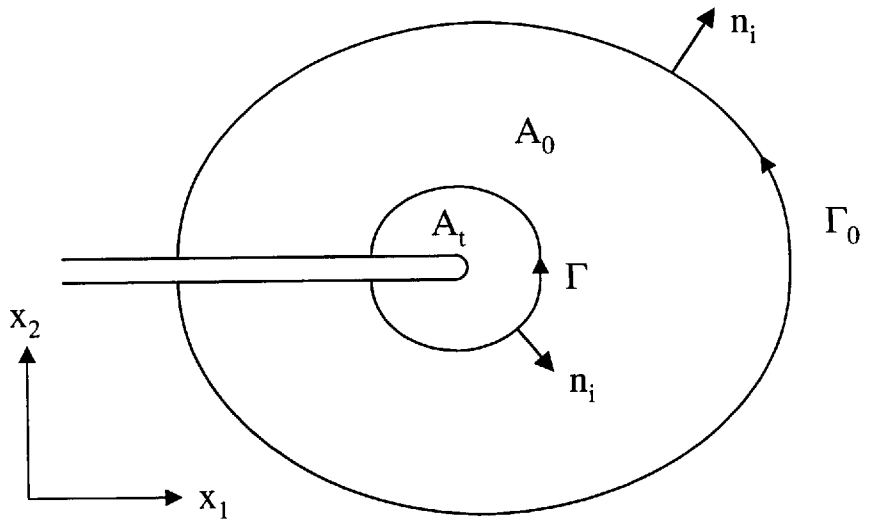

Figure 3.2: The J integral paths Γ, Γ_0 and the area A_0.

where $\Delta\Gamma$ is the length of a cell face along the path, ΔA is the area of a cell face in the xy-plane and ε is the strain tensor. i_x is the unit vector in the x-direction. Equation (3.8) was implemented in the FV program FOAM by using FOAM operators [75] for the spatial and temporal derivatives. The integral path was chosen to run along internal face centers, as the field quantities needed are easily available there. The cells are of square shape in the xy-plane and hence a rectangular path is convenient. The size of the rectangle can be varied to check the path independence.

3.6.3 The determination of K from the local stress field

From the definition of the SIF in Equation (1.1) it can be seen that, in the vicinity of the crack, for small values of r and in the crack path plane with $\theta = 0$, K is proportional to the product of σ_{yy} and $r^{1/2}$. This dependence can be exploited to calculate K directly from the local stress field [7] for a TPB impact test. This is useful as it allows the comparison of the SIF from this direct method with results from indirect methods. In a log scale plot (plotting $\log \sigma_{yy}$ versus $\log r$) the 'K' dominant region shold exhibit a slope of $-1/2$ (Figure 3.3). With a linear fit of the region with $r^{-1/2}$-dependence in the log scale plot, a SIF value can be obtained. This direct method requires a very fine mesh in order to model the local stress field accurately.

After identifying the region with the $r^{-1/2}$-dependence in the log scale plot, the selected cell faces (Figure 3.3) were fitted with a least squares procedure and a linear fitting function in MATHCAD. The cell face at the crack tip was excluded from the fit, as the

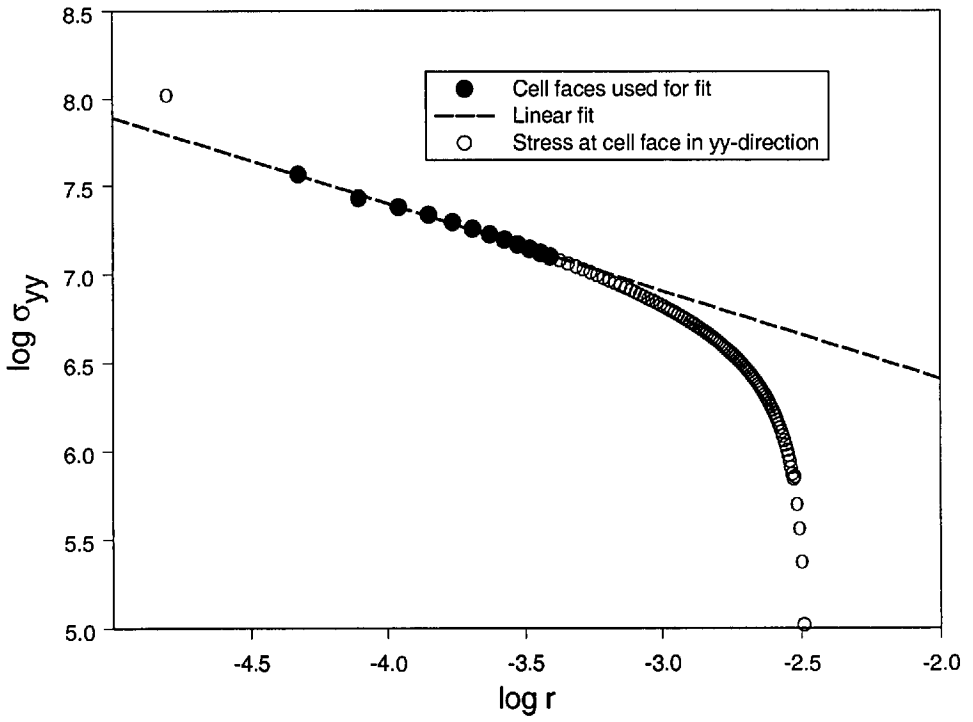

Figure 3.3: The stress at the crack tip as a function of *logr* for a TPB impact test.

singularity cannot be modeled accurately. K was then obtained from the intercept of the linear fit.

3.6.4 The determination of K from the bending moment

Several authors [16, 20, 40], who propose 1D analytical models of the TPB test, calculated the dynamic SIF from the bending moment. The underlying assumption for the validity of the proportionality of the SIF with the bending moment is that the stress profile at midspan in the dynamic case is the same as in the static case. At short times, when stress wave effects are dominant [24], it would be expected that deviations from the static stress distribution occur. One way of checking the accuracy of the assumption of the proportionality of the SIF with the bending moment is to compare the SIF from the bending moment with the SIF calculated with a different method such as the crack closure integral.

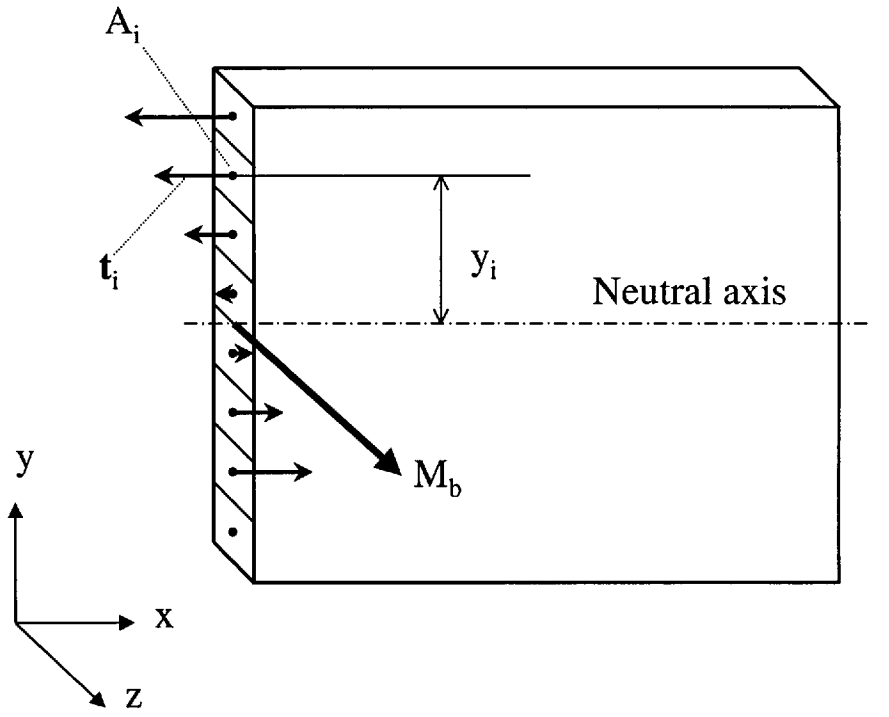

Figure 3.4: Determination of the bending moment.

In a symmetrical beam aligned along the x-axis under pure bending the bending moment can be calculated from [80]

$$M_b = \int_A \sigma_x y \, dA \tag{3.9}$$

where y is the distance from the neutral axis in y-direction and A is the total area of the cross section. Equation (3.9) is only valid if the deformation is sufficiently small.

In order to calculate the bending moment from FV results, a discretized form of Equation (3.9) is necessary. This allows the bending moment to be calculated from a summation over the cell faces on the boundary at midspan with

$$M_b = \sum_{i=1}^{N} (\boldsymbol{t}_i \cdot \boldsymbol{n}_i) \, y_i A_i \tag{3.10}$$

where N is the number of cell faces within the boundary patch for which the moment is calculated and A_i is the area of each cell face (Figure 3.4). The boundary traction vector for each cell face is denoted as $\boldsymbol{t}_i$, $\boldsymbol{n}_i$ is the face normal and the distance of the cell center from the neutral axis is y_i. Due to the fact that the boundary at midspan is a symmetry plane, there is no shear component of the traction i.e. the traction vector has only a component in the x-direction.

With Equation (1.12) and $M_b = P \cdot S/2$, where P is the load and with the span $S = 4W$ it is possible to express K as a function of the bending moment

$$K = f\frac{M_b}{2BW^{1.5}} \tag{3.11}$$

where f is a geometry factor, which can be calculated with Equation 1.13 and B is the specimen thickness. The calculations of K from the bending moment were done in MATHCAD, where the stress distribution for the boundary at midspan was imported for each time step. For each time step Equation (3.10) was evaluated to yield the bending moment. The dynamic SIF from the bending moment was then obtained via Equation (3.11).

3.7 The calculation of the dynamic correction functions k_d and g_d

The dynamic correction function k_d determines the amount of dynamic correction which needs to be applied to K evaluated quasistatically from time to fracture to correct for the dynamic behavior at the crack tip. With the applied displacement

$$u = V \cdot t \tag{3.12}$$

where V is the impact velocity and t is time and by using Equation 1.21 which assumes a linear contact stiffness

$$K \propto u \tag{3.13}$$

and with Equation 1.19 it is possible to write

$$k_d(t) = \frac{K_d(t)}{K_{st}(u_1)} \cdot \frac{t_1}{t} \tag{3.14}$$

where K_{st} is evaluated quasistatically at the displacement u_1, which is the displacement reached at the time t_1 in the dynamic calculation. t_1 can be chosen arbitrarily for small deformations and a linear contact stiffness and u_1 can then be calculated with Equation 3.12. For convenience half of the maximum displacement of the dynamic analysis was used to calculate K_{st}. For a FV analysis of a big epoxy specimen with $W = 0.1$m and an impact velocity of 1m/s the maximum displacement was 0.002m, which corresponds to a time of 2ms. Therefore the displacement $u_1 = 0.001$m was used for the determination of K_{st} and the dynamic FV analysis was performed from 0 to 2ms. Then k_d was calculated for each time step t_i with $K_d(t_i)$, $K_{st}(u_1)$ and $t_1 = 1$ms via Equation 3.14.

In the case of a nonlinear contact stiffness Equation 3.13 is only a first order approximation and the displacement at which K_{st} is evaluated is important. k_d was calculated the same way as for the simple model with a linear contact stiffness, as half of the maximum

displacement yields an average contact stiffness. This is a reasonable approximation and leads to an average value for K_{st}.

The dynamic correction function for G, g_d, can be calculated from k_d via Equation 1.4 as

$$g_d = k_d^2. \tag{3.15}$$

Dynamic effects can be expected to be higher for g_d than for k_d due to squaring of the k_d curve and the fact that both curves oscillate around unity.

Chapter 4

Finite Volume Analysis of the TPB Impact Test

4.1 Introduction

Modeling of the TPB test is important to enhance understanding and to obtain dynamic correction functions for specific test conditions. In this chapter a simple FV model of the TPB test is presented, which shows good agreement with the experiment. The simplicity of the model lies in the way the boundary conditions are applied.

4.2 The simple model

The simple model uses point loads as a boundary condition at the contact points of striker and anvil with the specimen (Figure 4.1). The experiment analyzed is a displacement controlled test with a constant applied velocity. The displacement is applied on a single boundary face center on the top patch of the specimen to approximate the effect of a rigid striker. The assumption of a rigid striker is a reasonable approximation for a metal striker (usually Aluminium or Titanium) in contact with a polymer specimen. The simple model shows a linear contact stiffness change with increasing load and bouncing is allowed at the striker contact point. In a real contact between a cylinder and a flat surface the contact stiffness will be nonlinear with the applied displacement due to the change in the contact area, whereas in the simple model the area on which the displacement is applied remains constant. Similarly the anvil is modeled as a boundary face center which is allowed to move up to allow bouncing, but is constrained in its downwards movement. The specimen modeled was a big SENB specimen with a width, W, of 0.1m, a span to width ratio, S/W, of 4 and a length to width ratio, L/W, of 5.5. The notch depth ratio, a/W, was 0.3 and the thickness, B, was 0.01m. The elastic

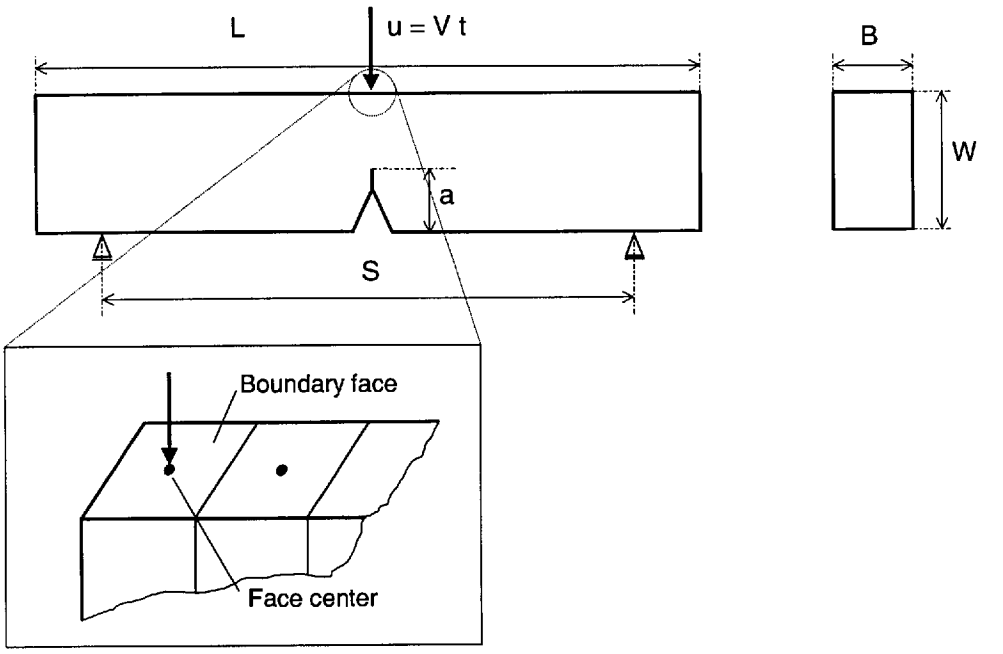

Figure 4.1: The simple FV model.

modulus, E, was 3.38GPa, the density, ρ, was 1216kg/m^3 and the Poisson's ratio was 0.33. These values were taken from Böhme [24] to allow a direct comparison between model and experiment. In all the results shown in this chapter the impact velocity V was 1m/s as in the experiment, except for one FV analysis with $V = 10$m/s. The FV program was operated in a 2D plane stress mode. In the initial FV simulation a mesh of 1100 (20×55) square cells was used. Subsequently the cell length in each direction was halved, which resulted in a mesh with 4400 cells. The number of cells was then again increased by a factor of 4 to 17600 cells. This mesh was subsequently used for the rest of the calculations, except for the results obtained by the local stress field method, where a local mesh refinement was performed to increase the resolution of the analysis close to the crack tip resulting in a mesh with 32576 cells. Two levels of local mesh refinement had to be used and to have fine enough cells in the area around the crack tip it was also necessary to make the width 10 times smaller and $W = 0.01$m was the result, whereby a/W, L/W and S/W were held constant. This is the size of a Charpy V-notch specimen [81], but the a/W ratio is 0.3 instead of 0.2 in the case of the Charpy V-notch specimen. The time step for the model with 1100 cells was 1μs, for the model with 4400 cells 0.5μs and for the model with the fine mesh a time step of 0.1μs was utilized. In the model of the small specimen with $W = 0.01$m a time step of 10ns was used.

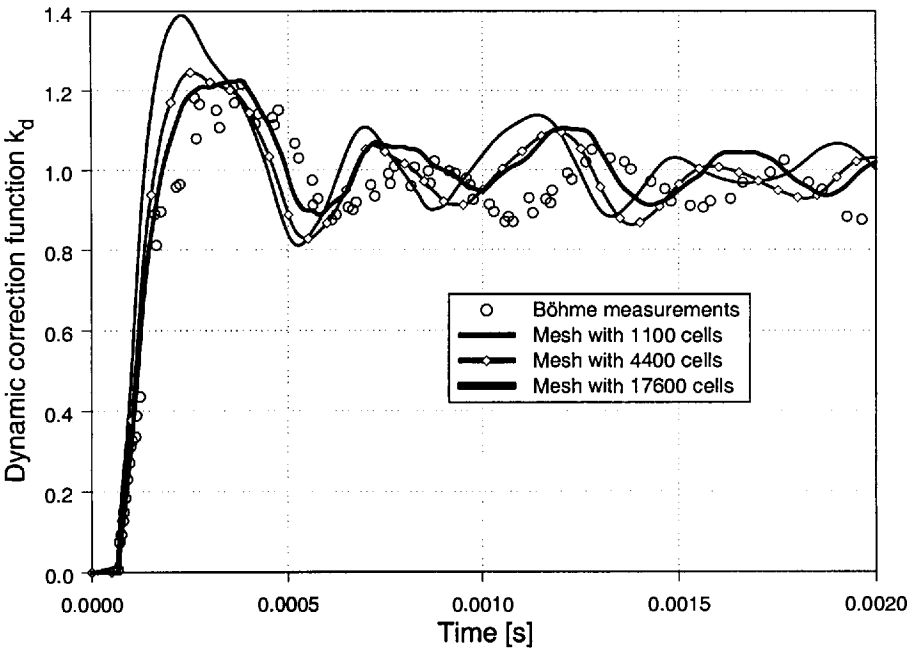

Figure 4.2: The dynamic correction function k_d for three different meshes with increasing mesh size.

4.3 FV analysis results

In Figure 4.2 k_d results for three meshes with increasing mesh density are displayed together with k_d measurements from Caustics by Böhme [24] for large specimen with $W = 0.1$m. The k_d values from the FV analyses were calculated employing the crack tip closure integral method. The striker and anvil loads are shown in Figure 4.3 and 4.4 respectively. Looking at the striker load it is apparent that it converges towards the experimental results with increasing mesh size. The initial slope of the striker load curve decreases with increasing mesh size. The reason for that is that the contact stiffness is lowering with increasing mesh size. The contact stiffness is determined in this model by the stiffness of the cell where the displacement is applied. The smaller the cell, the smaller the stiffness and hence the lower the initial slope will be. The best fit with the measured striker load was observed with the fine mesh with 17600 cells. One of the reasons for differences between the fine mesh and the experiment lies in the fact that the actual contact stiffness is nonlinear, as a cylindrical striker is in contact with a flat surface, the upper side of the specimen. This means that in the experiment the contact stiffness actually changes with the applied displacement. The anvil load in Figure 4.4 shows big differences between the FV results and the experiment. It seems to be more sensitive to the contact stiffness than the striker load. None of the

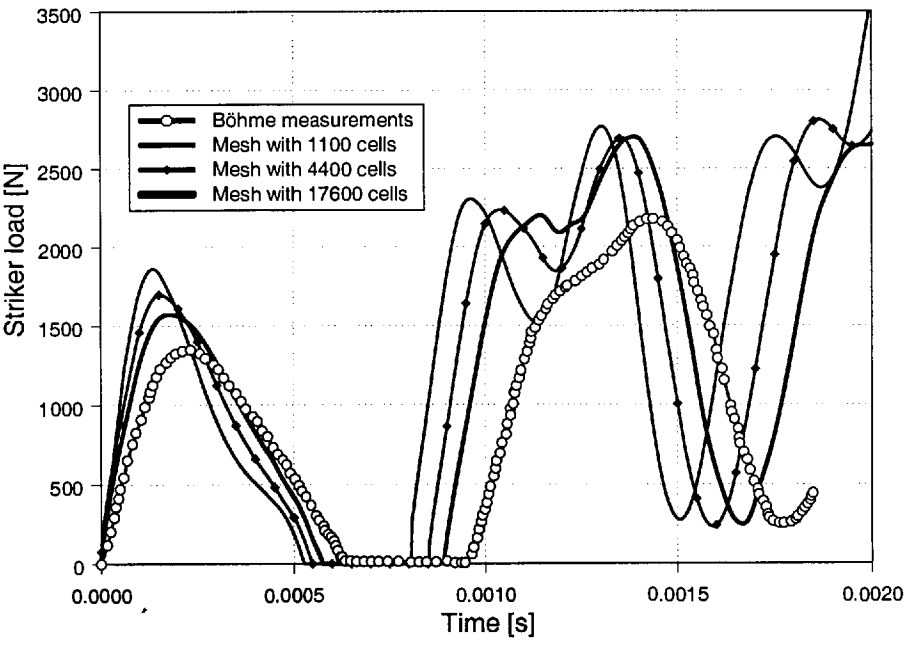

Figure 4.3: The striker load for three different meshes with increasing mesh size.

three different meshes models the anvil load well. This is due to the fact that in the experiment the anvil was machined from epoxy to make it more compliant in order to allow the anvil load to be measured with strain gauges [24]. This results in a soft anvil with a low contact stiffness. The assumption of a negligible deformation of the anvil cannot be applied in this case. The lower contact stiffness at the anvil is reflected in the lower force and the longer period of oscillation. The oscillation period in the experimental results would suggest that the anvil contact stiffness in the experiment is about half of the contact stiffness for the fine mesh. The anvil reaction is not too important for the k_d results, as it affects the SIF at the crack tip only at a late stage of the test.

In Figure 4.2 the first peak of the k_d curve changes with different meshes used. Also the initial slope of the k_d curve changes. The slope gets lower with increasing mesh size, which is due to the lower striker force, which changes the loading pattern at the crack tip. This shows that contact stiffness affects the shape of the k_d curve. The subsequent oscillations are also affected by the contact stiffness, as the natural frequency of the whole system is altered with a change in contact stiffness [19]. The change in natural freqency is reflected in the change of the oscillation period for different meshes in Figure 4.2. With increasing mesh size the k_d curves from the FV analysis approach the measurements. For the FV results shown later on in this chapter the fine mesh with 17600 cells was used, as it gave the closest fit with the experiment.

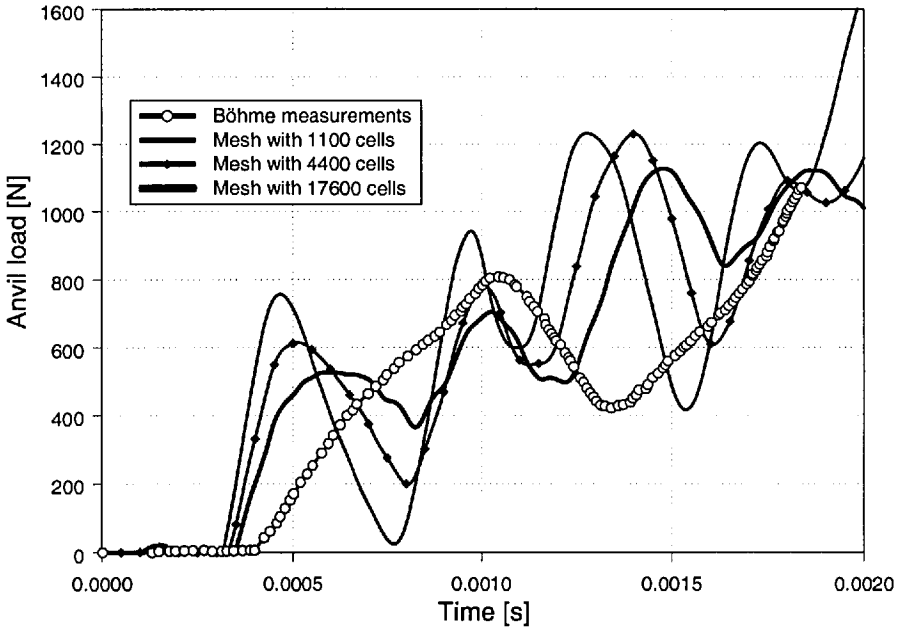

Figure 4.4: The anvil load for three different meshes with increasing mesh size.

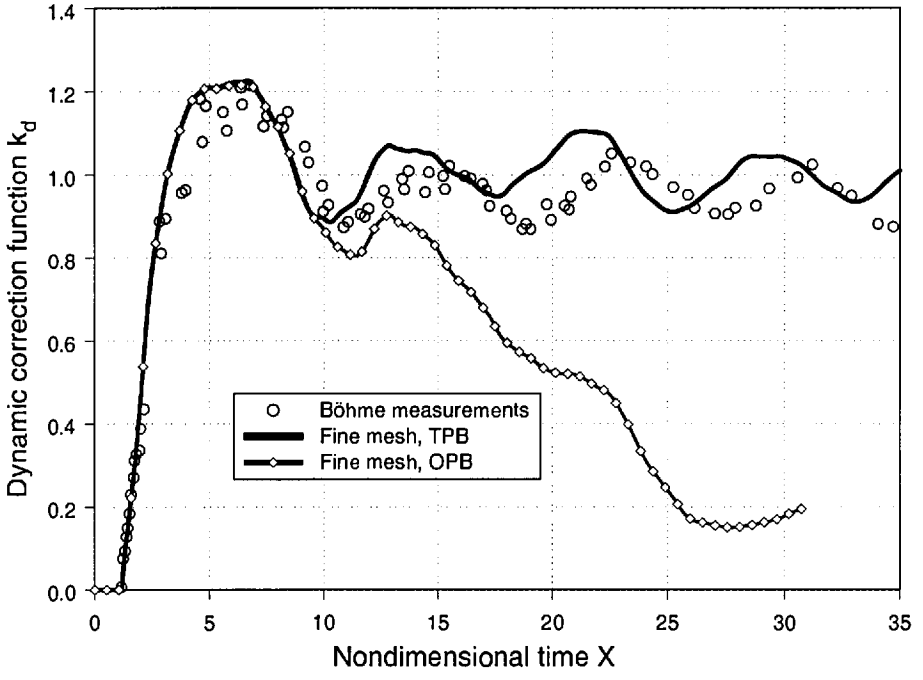

Figure 4.5: The dynamic correction function k_d for the three point bend (TPB) test and the one point bend (OPB) test versus nondimensional time.

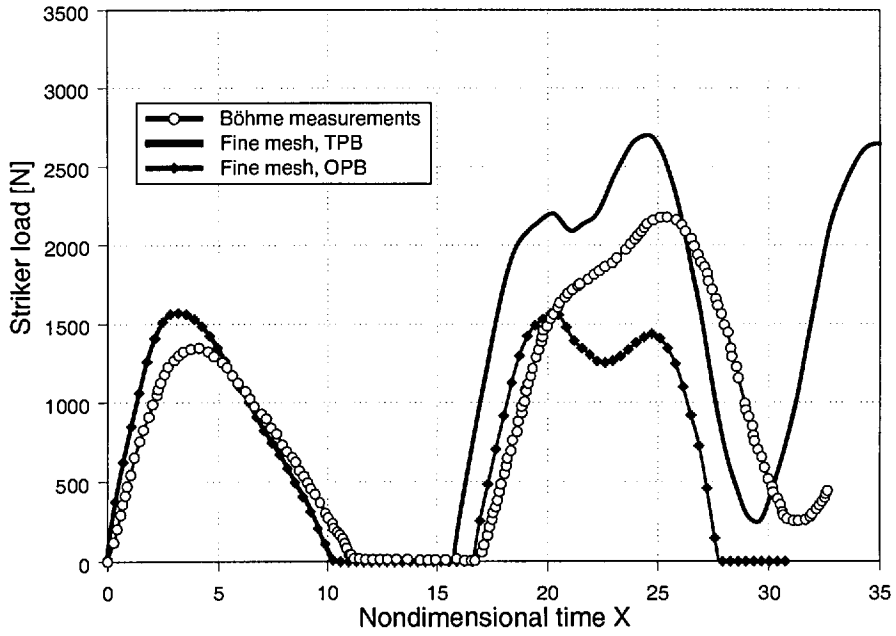

Figure 4.6: The striker load for the three point bend (TPB) test and the one point bend (OPB) test versus nondimensional time.

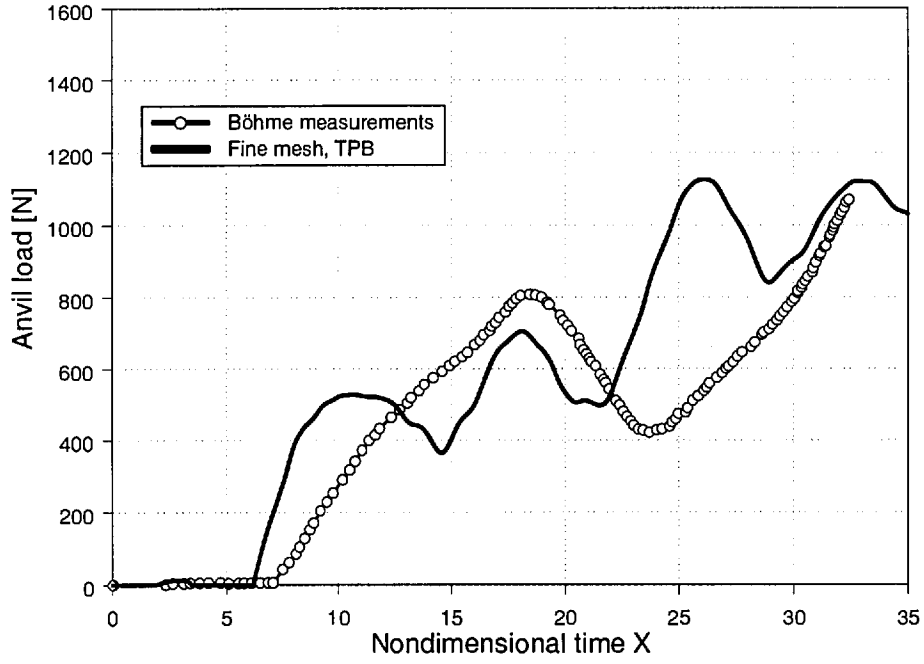

Figure 4.7: The anvil load for the three point bend (TPB) test versus nondimensional time.

In Figure 4.5 the results for the fine mesh and Böhmes measurements are again displayed, now versus the nondimensional time X, where $X = c_l t/W$. Also plotted is a curve for k_d from FV analysis of a one point bend (OPB) test. In the OPB test there are no anvils, which results in dynamic loading only, as inertia is the only load in this test and the quasistatic response of the specimen is a simple translation. This can be seen in the graph for increasing X, where k_d goes towards 0 for $X > 9$. For $X < 9$ a three point bend (TPB) test is, as far as the crack is concerned, essentially a OPB test for this specimen configuration and test setup. This is due to the delayed response from the anvils, the reasons for which are twofold. First there is some delay due to the time needed for the longitudinal stress wave to reach the anvil and then come back to the crack tip. It takes $X \approx 2.2$ for the wave to reach the anvil from the point of impact, which can be seen in Figure 4.7, where a small rise in the anvil force is observed at this time. A longitudinal wave needs $X = 2$ to travel a distance of $2W$ from the middle of the specimen, but due to the fact that the point of impact is on the top of the specimen and the anvil is on the bottom, the time needed for the wave to reach the anvil from the point of impact is $X = \sqrt{5}$, which is around 2.2. In addition to the time for the stress waves to travel to the anvil and back the specimen bends away from the anvils in the first instance due to the dynamics of the system. The specimen is, for a short time, in contact with the anvil and then moves away from the anvil. In the experiment this first peak is not recorded. This could be due to the fact that the anvils in the experiment were very compliant and hence the height of the first peak is very small and therefore remains undetected. The specimen regains contact with the anvil in the experiment only after $X > 7$. No change in the SIF at the crack tip is observed until $X \approx 9$, as it needs again $X = 2$ for the information of regained contact at the anvil to reach the crack tip. From Figure 4.5 it is obvious that the anvil reaction is not important at times up to $X \approx 9$ (for $a/W = 0.3$, $L/W = 5.5$ and $S/W = 4$). Böhme suggested [31] that for this specimen configuration k_d should be set to 1 in the quasistatic time range where $X > 9.2$, as k_d remains within a $\pm 10\%$ envelope in this time range. This means that either a dynamic procedure can be used, where k_d corrects for dynamic effects and there is no influence of the anvils, or for longer times a quasistatic procedure is applicable, where no dynamic correction is necessary. The explanations above show that in many cases the anvil reaction is not important in a high rate test for the given specimen dimensions.

4.4 K from the local stress field

The stress intensity factor K i.e. the dynamic correction function k_d was also calculated from the local stress field and the results are compared with the results from crack tip closure for the fine mesh with additional mesh refinement in Figure 4.8. The results show that k_d from the local stress field yields the same results as crack tip closure.

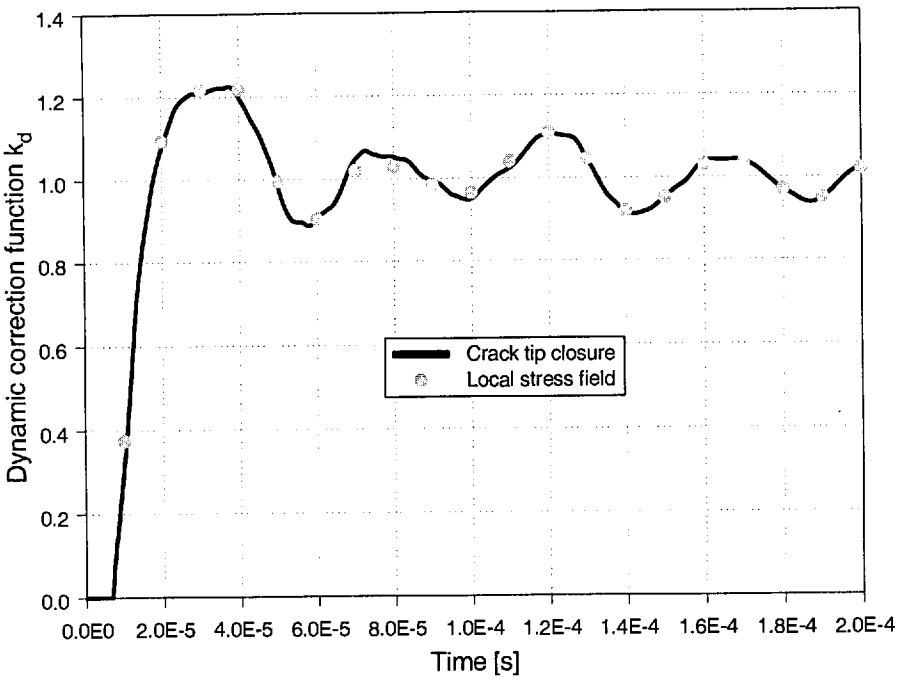

Figure 4.8: The dynamic correction function k_d from crack tip closure and from the local stress field.

This demonstrates that it is valid to calculate K from the dynamic energy release rate with Equation (1.4) in the case of a stationary crack in a transient stress field. As the crack closure integral is a fast and efficient method to determine K indirectly via G, it is preferable to the direct method of computing K from the stress field, which needs a very fine mesh and therefore more computation time and also a cumbersome evaluation procedure.

4.5 K from the bending moment at short times

Several 1D models of the TPB test use the bending moment, M_b, at midspan to calculate the SIF and k_d [16, 43, 40]. With a dynamic 2D FV analysis it is possible to check the validity of the assumption of $K \propto M_b$. The results in Figure 4.9 were calculated with the fine mesh and local mesh refinement around the crack tip for $W = 0.01$m, $a/W = 0.3$, $L/W = 5.5$ and $S/W = 4$. At times less than 40μs, which is equivalent to $X < 7$, the assumption of the proportionality of the bending moment at midspan and K is not valid, as K from the bending moment is not equivalent to the SIF at short times. A 1D model which uses the bending moment to calculate K will therefore not give accurate results at short times. Considering the fact that it is at short times with $X < 9$, where a model for the calculation of k_d is needed, as otherwise k_d can be

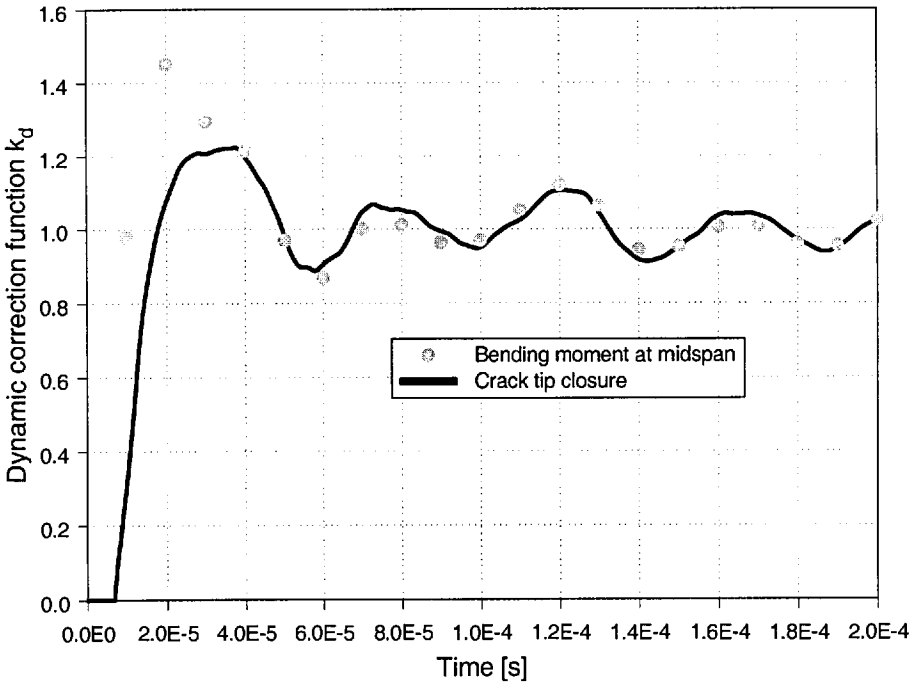

Figure 4.9: The dynamic correction function k_d from the bending moment at midspan and crack tip closure.

set to 1 with good accuracy, the presented data indicate that 1D models, which utilize the bending moment to calculate K, are not suitable for the prediction of the dynamic correction function k_d.

4.6 The limits of applicability of k_d curves in the case of a linear contact stiffness

Once a dynamic correction function is determined, it is important to know to which tests it can be applied, as it is very time consuming to obtain a separate k_d curve for each test. The dynamic correction function k_d can be used for other test conditions under certain circumstances.

4.6.1 Varying impact velocity

As the dynamic K is scaled with the static K, a change in impact velocity does not affect the shape of the k_d curve when the contact stiffness is linear. This can be seen in Figure 4.10, where both curves for $V = 1m/s$ and $V = 10m/s$ follow the same line. This is only true if all the stiffness components in the system are linear. This is the

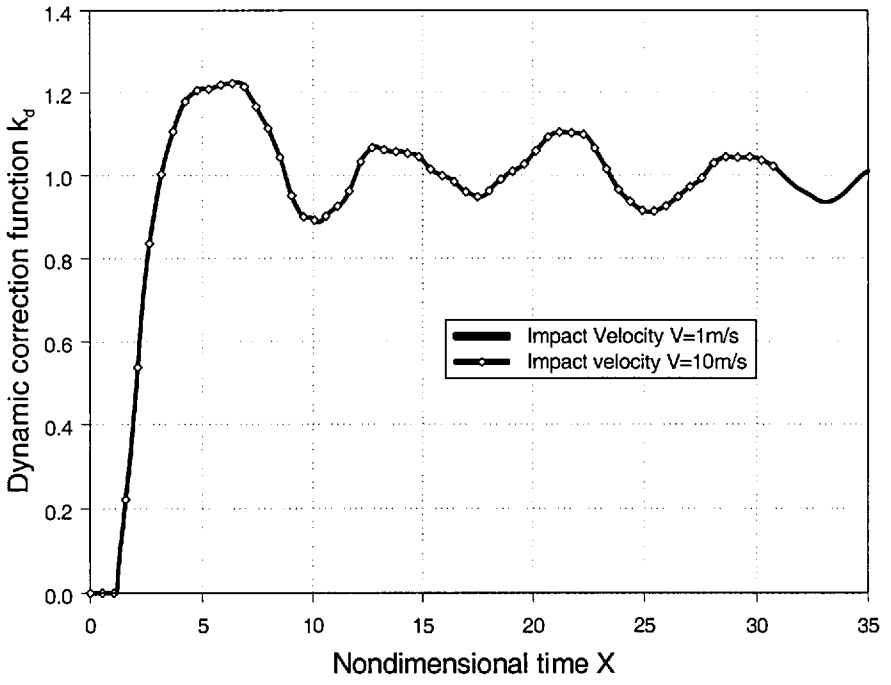

Figure 4.10: The dynamic correction function k_d for two different impact velocities.

case in the simple model, as the contact stiffness is determined by a single cell, which is compressed in a linear manner and the beam in bending is also linear.

In reality, the contact stiffness is nonlinear and this changes the shape of the k_d curve with velocity due to the fact that the actual forces are not linear with impact velocity. This means that, strictly speaking, a dynamic correction function is only valid for the velocity at which it was obtained, if a nonlinear contact stiffness is involved. This will be investigated further in Chapter 5.

4.6.2 Varying specimen width

The advantage of using a nondimensional time is that a change in specimen width does not affect the k_d curve if the contact stiffness is assumed to be linear. Figure 4.11 shows this and the curves for $W = 0.01$m and for $W = 0.1$m follow the same line. This demonstrates that it is possible to use k_d curves obtained from a big specimen with $W = 0.1$m to evaluate a test with a specimen width of 0.01m. It is therefore possible to use a k_d curve for any specimen width, provided that a nondimensional time is used and all other specimen dimension ratios, i.e. a/W, L/W and S/W, are held constant.

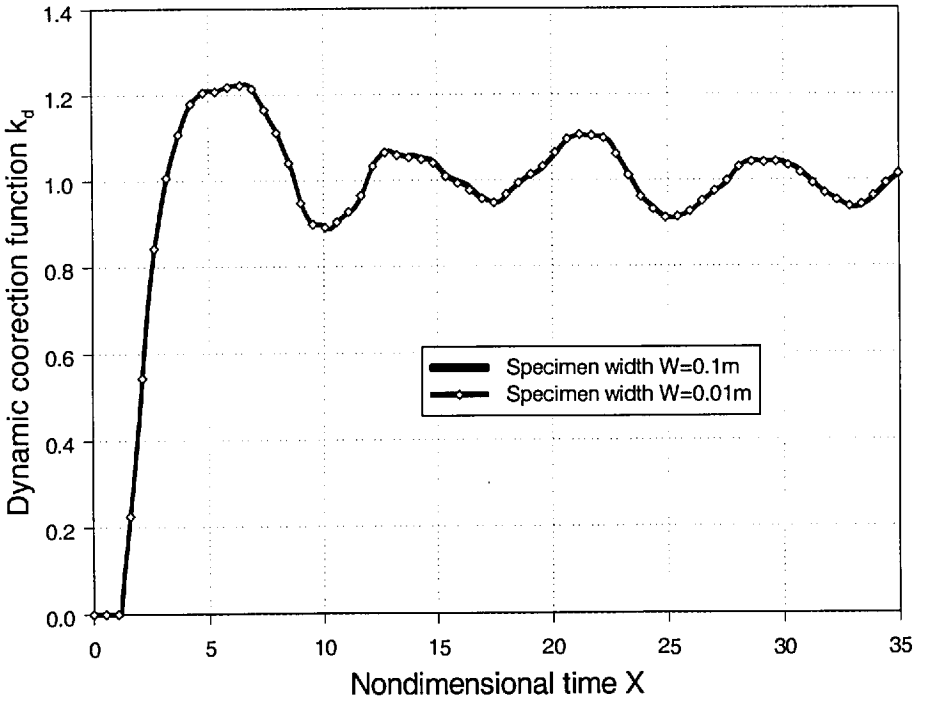

Figure 4.11: The dynamic correction function k_d for two different specimen widths.

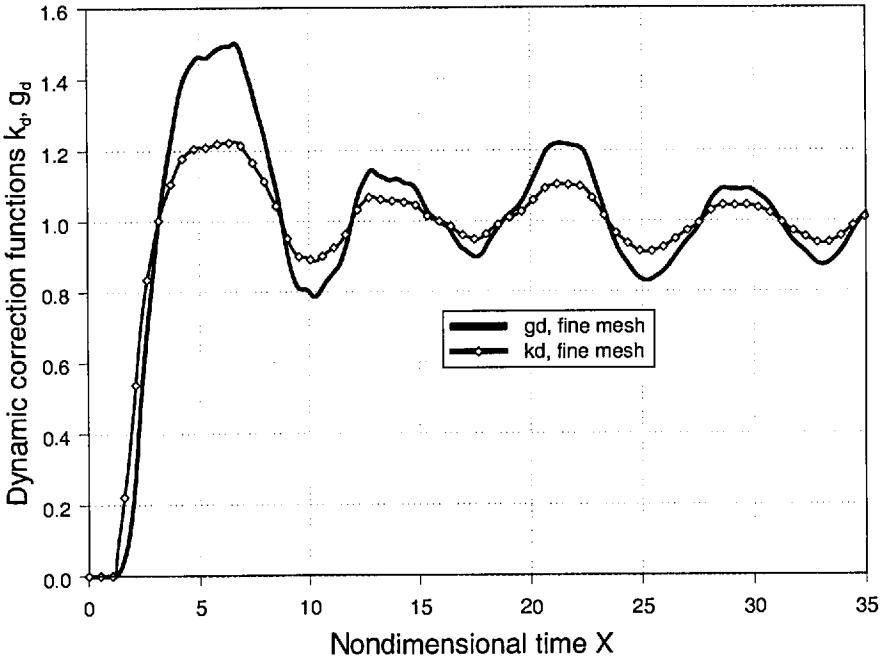

Figure 4.12: The dynamic correction function g_d in comparison with k_d.

4.7 The dynamic correction function g_d

With Equation (3.15) g_d can be easily calculated from k_d by squaring it. Figure 4.12 shows the dynamic correction function g_d for the fine mesh with 17600 cells in comparison with k_d. Overall, the amount of dynamic effects is higher for g_d than for k_d. The g_d curve from the simple model and the fine mesh oscillates within a $\pm 22\%$ envelope after the first peak. This is about twice as much as for k_d, which stays within a $\pm 10\%$ envelope after the initial peak.

Chapter 5

Finite Volume Analysis of the TPB Impact Test with a Contact Procedure

5.1 Introduction

Studies with analytical models [38, 40] have shown that the shape of the dynamic correction function k_d is strongly dependent upon the contact stiffness between specimen and striker. It is obvious that the eigenfrequency of a one mass two spring model is altered if the stiffness of the first spring, k_1, is changed. Although the specimen stiffness, k_2, remains constant, the change in k_1 alters the response of the whole system and hence affects the dynamic correction function k_d. The influence of the contact stiffness can also be expected in a more accurate numerical 2D model of the TPB impact test, but no 2D analysis on the effect of the contact stiffness on the dynamic correction function k_d was found in the literature. Furthermore, the contact between the striker and the specimen is nonlinear i.e. the contact stiffness varies with the applied displacement. A linear spring, as used in the mass spring model, is only an approximation of this nonlinear contact stiffness and will lead to errors. In this chapter an investigation of the influence of the contact stiffness on the TPB impact test is presented, where a contact procedure is used, which accurately models the contact between striker and specimen as well as between anvil and specimen.

5.2 The model with the contact procedure

In the model from Chapter 4 the boundary conditions were applied on single cells. The model presented in this chapter uses a FV representation of striker, anvil and specimen

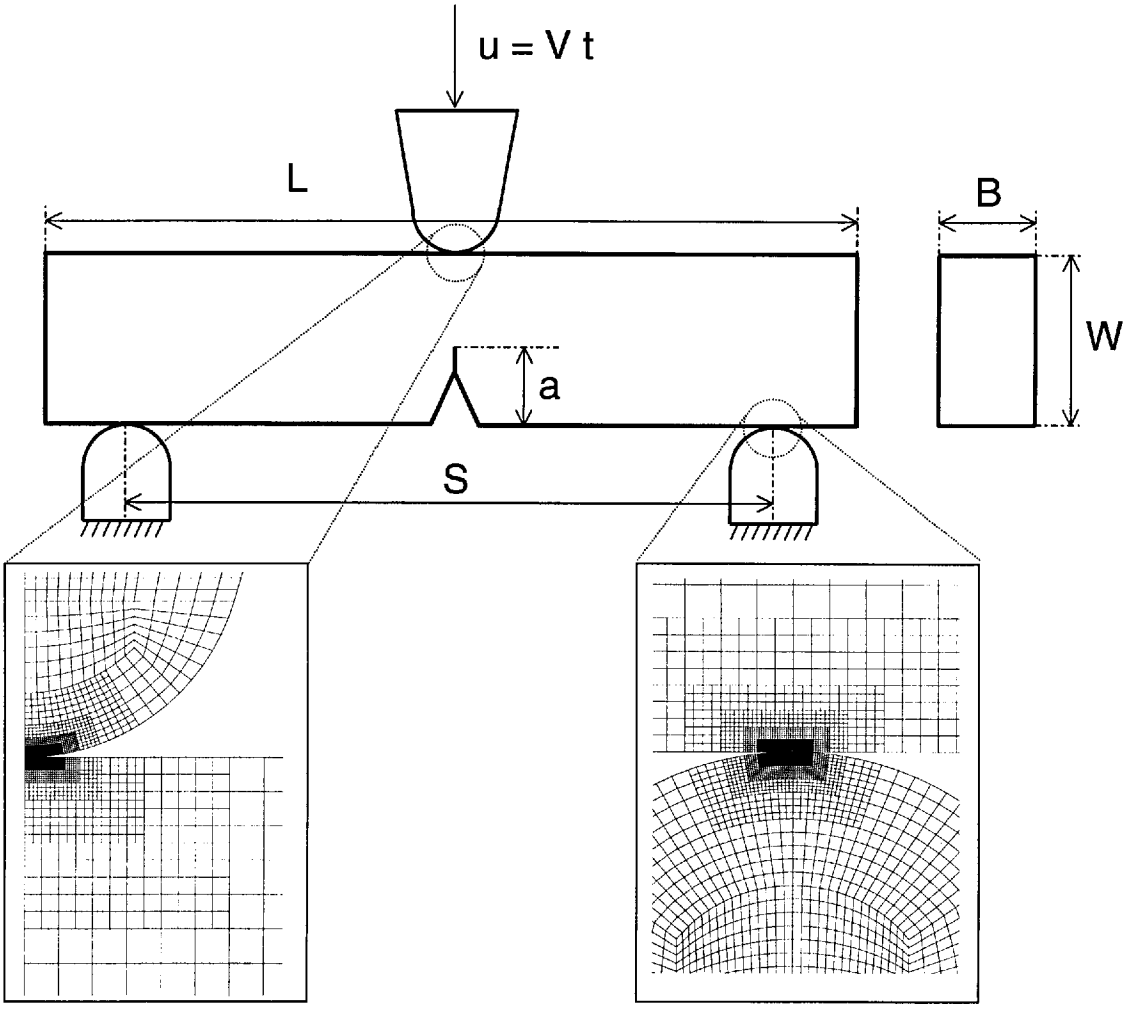

Figure 5.1: The model including contact effects.

in conjunction with a contact procedure to find the contact forces and areas for each time step. The model with the contact procedure is shown in Figure 5.1. The top of the striker was displaced with a constant velocity and the bottom of the anvil was fixed. Due to symmetry, only half of the specimen and the striker had to be modeled. As in Chapter 4, Böhmes experiment [24] with a big SENB epoxy specimen with $W = 0.1$m and $a/W = 0.3$, $L/W = 5.5$, $S/W = 4$ and $B = 0.01$m was modeled to allow a direct comparison between model and experiment. The material properties for epoxy [24] were taken as $E = 3.38$GPa, $\rho = 1.216$kg/m^3, and the Poisson's ratio as 0.33. The dimensions for striker and anvil, which were not given in [24] were determined from images of the test setup. The first tapered part of the striker in Böhme's setup was used in the model, which was 0.03m high and 0.03m long with a thickness of 0.01m, thereby matching the specimen thickness. The striker tip radius was 0.008m and the striker material was steel with a modulus of 210GPa, a density of 7800kg/m^3 and a Poisson's ratio of 0.3. The dimensions of the anvil were also taken from [24] with a

height of 0.03m, a length of 0.02m, a thickness of 0.01m and an anvil tip radius of 0.01m.

Local mesh refinement was necessary to have a sufficient number of similar sized cells at both sides of contact. The mesh refinement and modeling of striker and anvil increased the mesh size from 17600 (the mesh size previously used) to 25875 cells. Five levels of local mesh refinement were used at the striker and anvil contact areas of the specimen. Due to a finer mesh only four levels of local mesh refinement were needed for striker and anvil. The SIF was obtained with the crack tip closure integral method.

The material properties of epoxy were used for the anvil for one calculation, but due to numerical instabilities of the contact procedure for compliant anvils the properties of steel were used for the anvil for the other calculations. For the model of the steel specimen a steel striker was used with the material properties reported above and the anvil was set to be rigid, again to avoid numerical instabilities of the contact procedure. The time step in all the computations with the big epoxy specimen was 1μs. For the steel specimen a time step of 0.3μs was chosen.

One FV analysis was performed for a small epoxy specimen with $W = 0.01$m and $a/W = 0.3$, $L/W = 5.5$, $S/W = 4$ and $B = 0.01$m. A radius of 0.002m was used both for the anvil and the striker. Here the time step was set to 0.1μs. For the FV analysis of a small PE specimen with $W = 0.01$m the properties of a MDPE material with a modulus of 1GPa, $\rho = 940\text{kg/m}^3$ and a Poisson's ratio of 0.3 were used together with a time step of 0.16μs.

In all the results shown in this chapter the impact velocity V was 1m/s as in the experiment, except for the FV analyses on the velocity dependence of k_d, where V was set to 1, 10 and 30m/s. The FV program was used in a 2D plane stress mode for all the calculations in this chapter.

5.3 The results from the contact model with a steel anvil

In Figure 5.2 the dynamic correction function k_d is displayed for the model with the contact procedure together with Böhme's measurements from [24] and the results from the simple model from Chapter 4. For the contact model a steel striker, an epoxy specimen and a steel anvil were used. The steel anvil was chosen, as the contact procedure used experienced numerical instabilities for compliant anvils and furthermore steel is the most likely anvil material to be used in a test. A steel anvil in contact with an epoxy specimen shows only small deformation of the anvil, which the contact procedure can handle without instabilities. The analysis employing the contact procedure models the experiment considerably better than the simple model, especially in the initial part

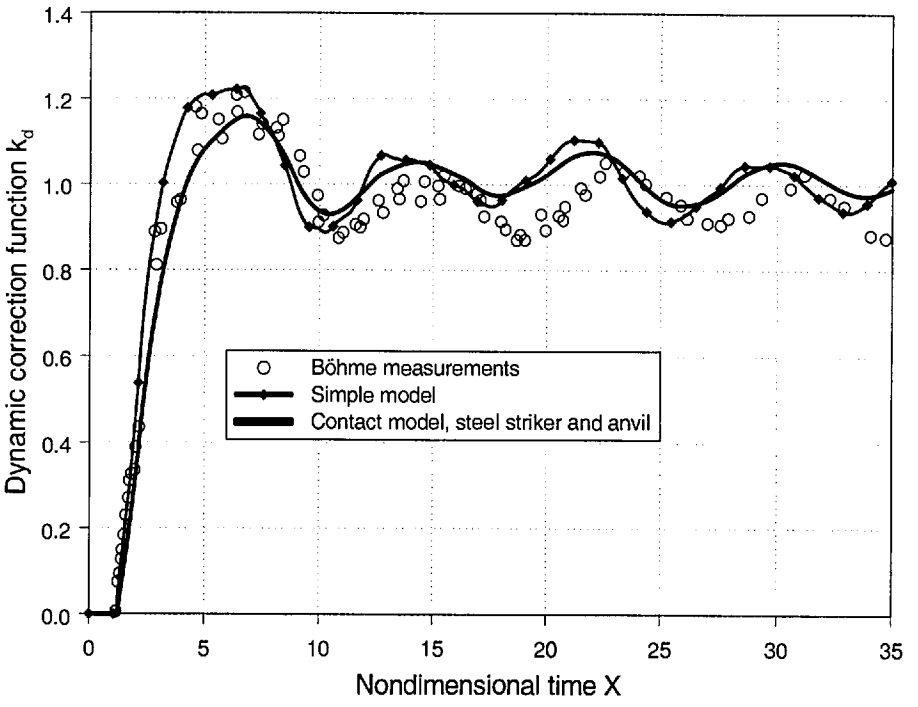

Figure 5.2: The dynamic correction function k_d for the contact model with a steel striker, epoxy specimen and steel anvil in comparison with the simple model and experimental data from [24].

for $X < 9$. As discussed in Chapter 4 the anvils start to influence k_d for $X > 9$ and the steel anvil in the model is considerably stiffer than the epoxy anvil in the experiment.

Looking at the striker load in Figure 5.3 very good agreement between the contact model and the experiment can be seen for $X < 16$. At $X \approx 11$ the striker loses the contact with the specimen i.e. the specimen bounces and the contact is established again at $X \approx 16$ in the contact model and for $X \approx 17$ in the experiment. From the striker load it is obvious that the contact model fits the experiment closer than the simple model i.e. it is a better model.

Figure 5.4 shows the anvil load from the contact model in comparison with the anvil load from the simple model and Böhme's measurements. Whereas it fits the experiment better than the simple model, the anvil load is still not satisfactorily modeled. As mentioned above, this is due to the fact that in the experiment a compliant epoxy anvil was used and the contact model employs a steel anvil. The stiffness of the latter is higher, which explains the higher initial slope of the anvil load.

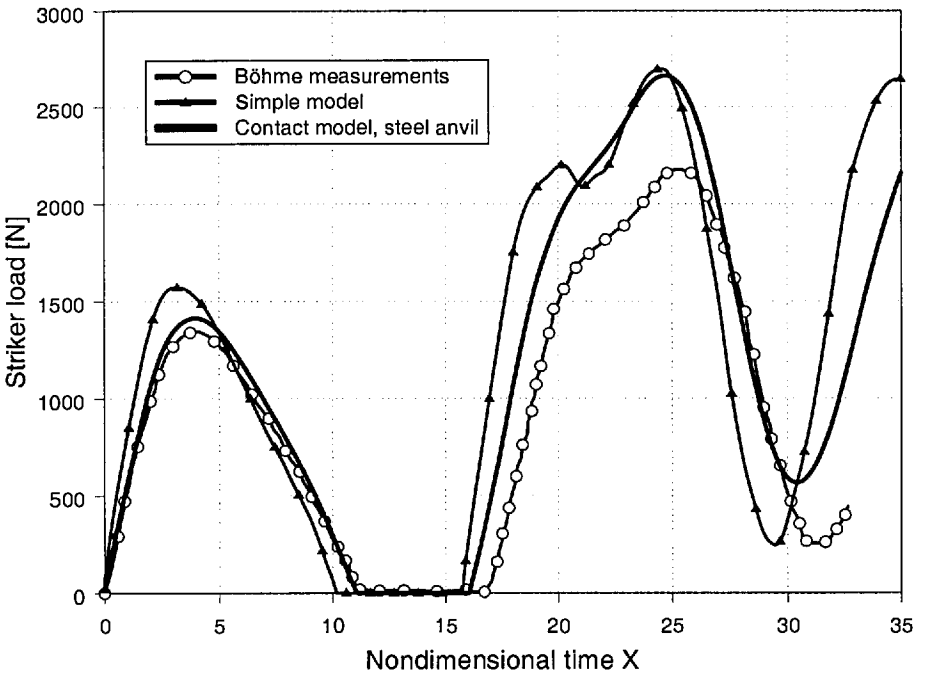

Figure 5.3: The striker load for the contact model with a steel striker, epoxy specimen and steel anvil in comparison with the simple model and the experiment.

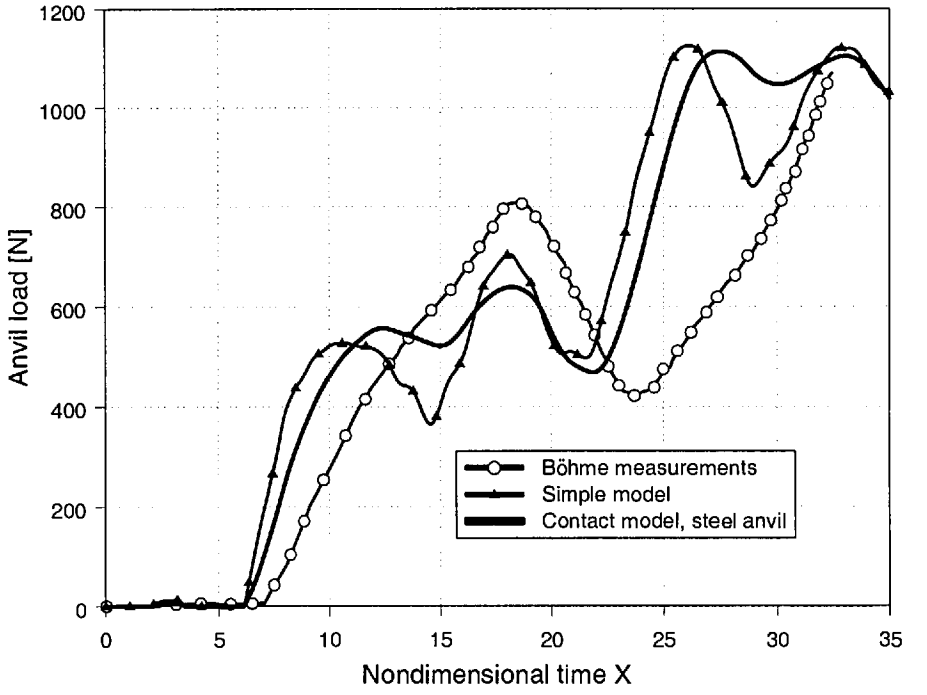

Figure 5.4: The anvil load for the contact model with a steel striker, epoxy specimen and steel anvil in comparison with the simple model and the experiment.

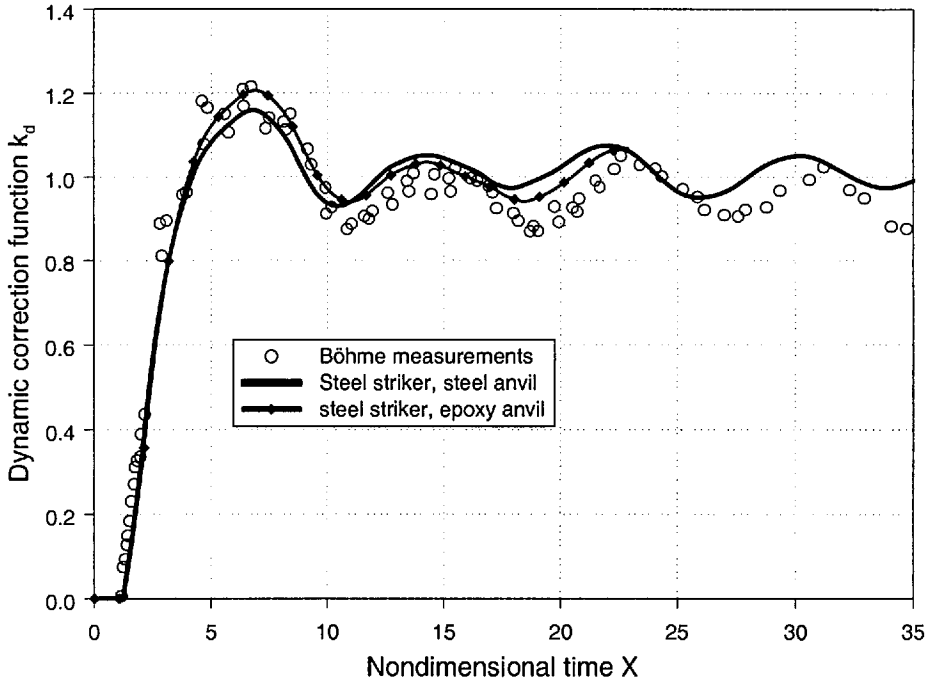

Figure 5.5: The dynamic correction function k_d for the contact model with an epoxy anvil in comparison with results for the steel anvil and the experiment.

5.4 The results from the contact model with an epoxy anvil

To investigate the influence of the anvil on k_d, a FV model with the contact procedure, an epoxy anvil, as used in Böhme's experiment, and a steel striker was analyzed (Figure 5.5). Despite the fact that numerical oscillations at the anvil contact point occurred during the computation, the k_d curve is closer to the experiment. Especially the second peak of the k_d curve is predicted better by the model with the epoxy anvil. This is due to the influence of the anvil at this time and the fact that the anvil force in this model is close to the one observed experimentally (Figure 5.6). The anvil force from the model with the epoxy anvil in Figure 5.6 exhibits oscillations, which are purely numerical and at $X = 23$ the calculation was terminated. Further improvement of the contact procedure to account for 'soft' contacts in a more stable manner was beyond the scope of this work and therefore was not attempted. The results nevertheless show that the epoxy anvil does change the forces at the anvil and that a model with a compliant anvil is capable of reproducing the experimental forces recorded there. The results also show that the epoxy anvil does change the behaviour of the system and therefore alters the k_d curve. The difference in k_d for $X < 9$ between the model with an epoxy and a steel anvil is due to the way the k_d curve was normalized. Although the K_d values at times

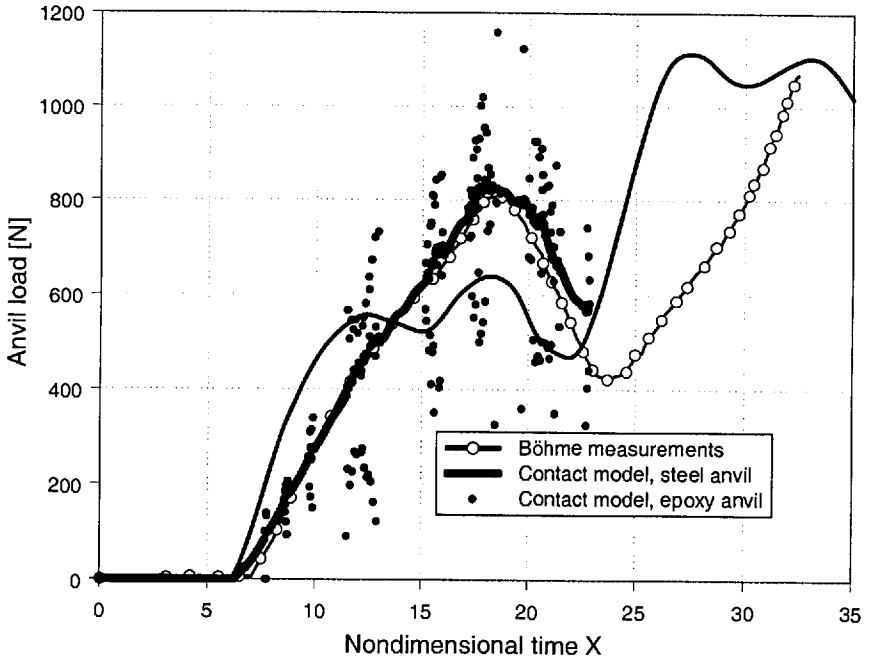

Figure 5.6: The anvil force for the contact model with an epoxy anvil in comparison with results for the steel anvil and the experiment.

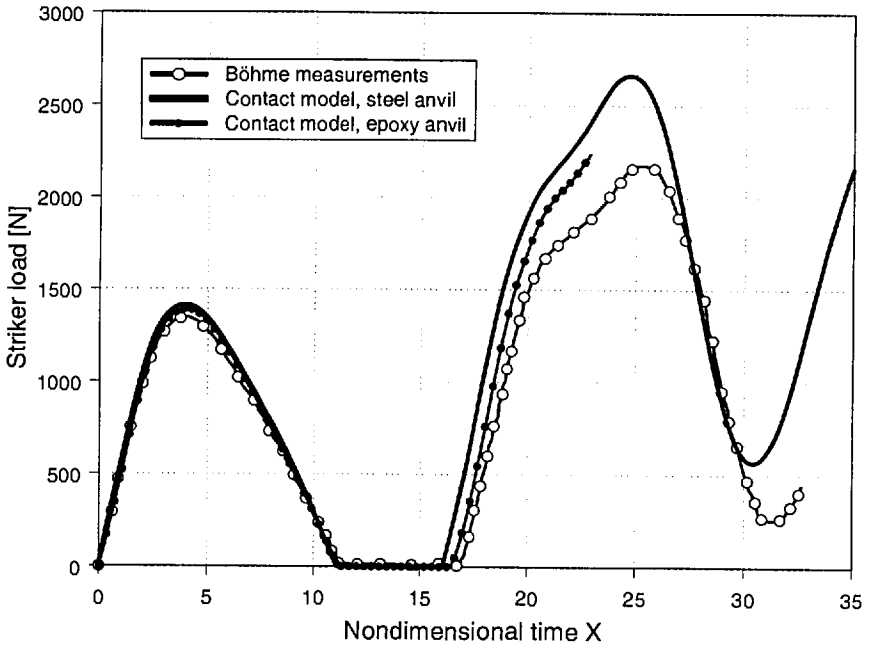

Figure 5.7: The striker force for the contact model with an epoxy anvil in comparison with results for the steel anvil and the experiment.

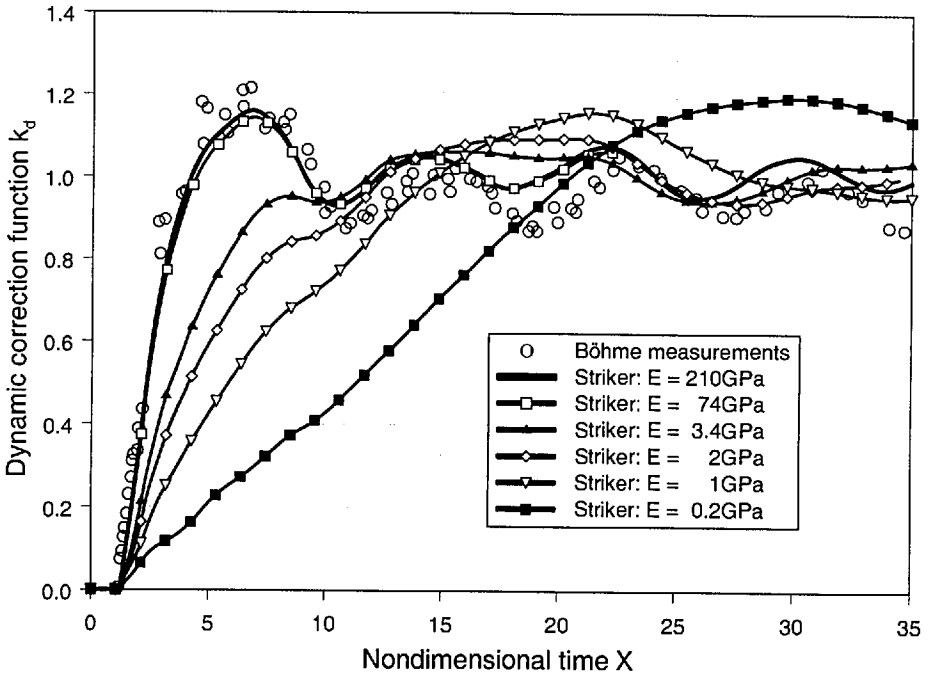

Figure 5.8: The influence of the striker stiffness on the dynamic correction function k_d.

$X < 9$ are not affected by the anvil (Chapter 4), the static stress intensity factor K_{st} is and hence, due to the normalization of K_d with K_{st}, k_d is different in this region for the model with the epoxy anvil. This means that the difference only arises from the way k_d was calculated. The striker force for the model with the epoxy anvil in Figure 5.7 demonstrates that the good fit of the anvil force has an impact on the striker force and the agreement with the experiment until $X \approx 20$ is very good.

5.5 The influence of the striker stiffness on k_d

Studies with analytical models [38, 40] show that the dynamic correction function k_d is dependent on the contact stiffness between specimen and striker. Experimentally k_d curves were measured for the combination of a steel striker, an epoxy specimen and an epoxy anvil, as reported in [24] and [31]. A numerical study [48] used only a rigid striker and a rigid anvil to model the k_d curves reported in [31]. The effect of the contact stiffness was not investigated. Following the results from the mass spring model studies and by using the contact procedure a study of the influence of the contact stiffness was performed. The contact stiffness was varied in a wide range by varying the striker stiffness i.e. the elastic modulus of the striker from 210GPa to 0.2GPa (Figure 5.8). The influence of the contact stiffness on k_d is apparent. For metallic materials like steel

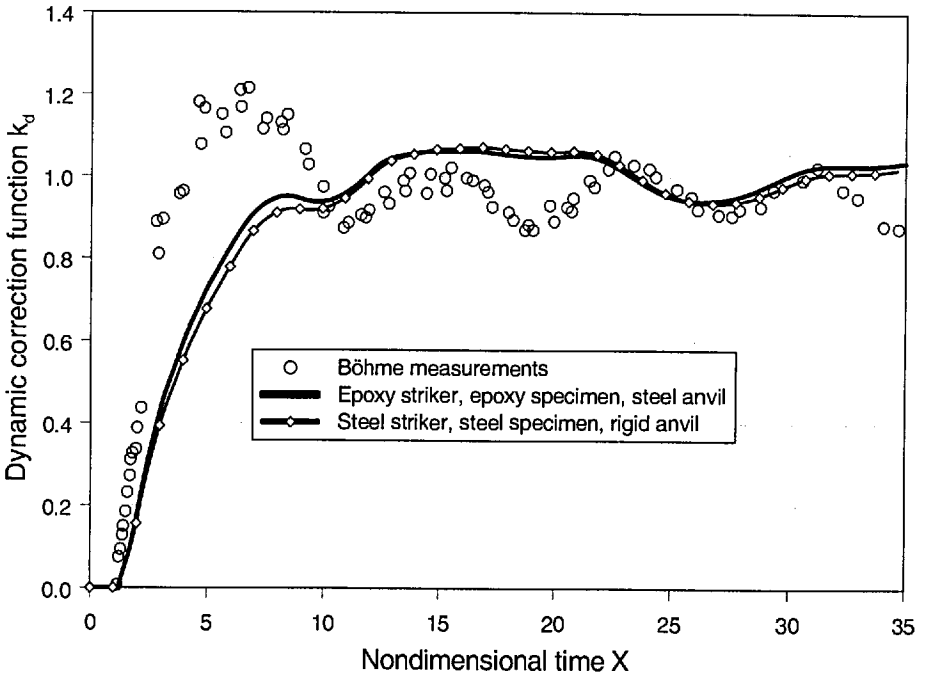

Figure 5.9: The dynamic correction function k_d for a steel specimen with a steel striker and an epoxy specimen with a steel striker compared to Böhme's measurements with a steel striker, epoxy specimen and epoxy anvil.

($E \approx 210$ GPa), titanium ($E \approx 130$ GPa) or aluminum ($E \approx 70$ GPa) with a modulus 20 or more times higher than the epoxy specimen ($E = 3.38$GPa) the curve remains virtually the same. If the specimen material properties are also used for the striker, which is the curve with $E = 3.4$GPa, the shape of the curve changes considerably. Especially the initial rising part of the curve is substantially lower and no pronounced initial peak is observed. This makes sense, as due to the lower contact stiffness the load increase will be slower and this limits the rise of the SIF at the crack tip. By decreasing the contact stiffness further this effect becomes more pronounced and the initial slope decreases steadily. For a striker modulus of 0.2GPa the initial slope is only about a fifth of the initial slope for a steel striker. It is apparent from the results that the k_d curve from Caustics [24] is only valid for the striker contact stiffness for which it was determined.

Figure 5.8 showed that if the same material was used for striker and specimen, here epoxy, a very different k_d curve can be expected. This has implications on testing metals. If a steel specimen is tested with a steel striker, the ratio of the contact stiffness to the specimen stiffness will be similar to the ratio for an epoxy striker and specimen and therefore a similar curve could be expected. Figure 5.9 shows both curves and their similarity is striking. The amount of dynamic effects in k_d curves in case of the

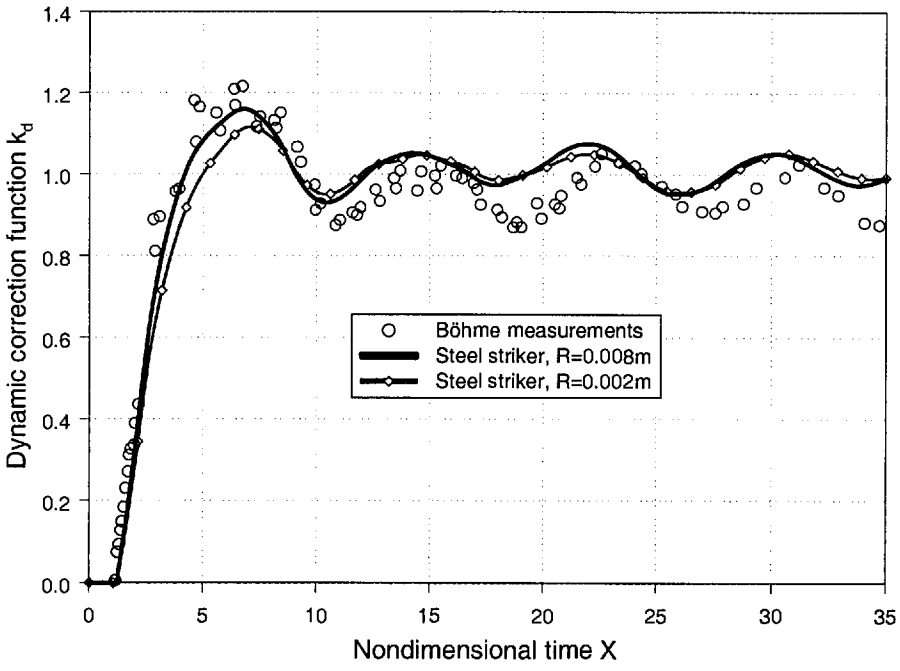

Figure 5.10: The dynamic correction function k_d for striker radii of 0.008 and 0.002m compared to Böhme's measurements.

same material for specimen and striker is drastically reduced in comparison with a rigid striker. The steel specimen with the steel striker combination had a rigid anvil to avoid the problem of numerical instability at the anvil. From Figure 5.9 it is obvious that the application of a k_d curve measured with a comparably rigid striker and an epoxy specimen to a test with a steel specimen and a steel striker leads to wrong results. It should also be noted that the stiffness of a steel specimen is about 50 times higher than a polymer specimen for the same specimen size. Therefore the stiffness of the testing machine is in many cases no longer negligible in comparison with the contact stiffness. This will affect the shape of the k_d curve and the initial slope of the curve will become even lower.

5.6 The influence of the striker radius on k_d

The influence of the striker radius on k_d is not so important for practical applications of the k_d concept, as this radius can be prescribed in a test protocol. The striker radius in a Charpy test for polymers [82] is prescribed as 0.002m by ISO 179-1 and for metals ASTM E23 [81] prescribes a striker tip radius of 0.008m. Böhme used a striker tip radius of 0.008m for a big specimen with $W = 0.1$m and the k_d curve for these dimensions was presented in Figure 5.2. In addition to that a TPB test with a

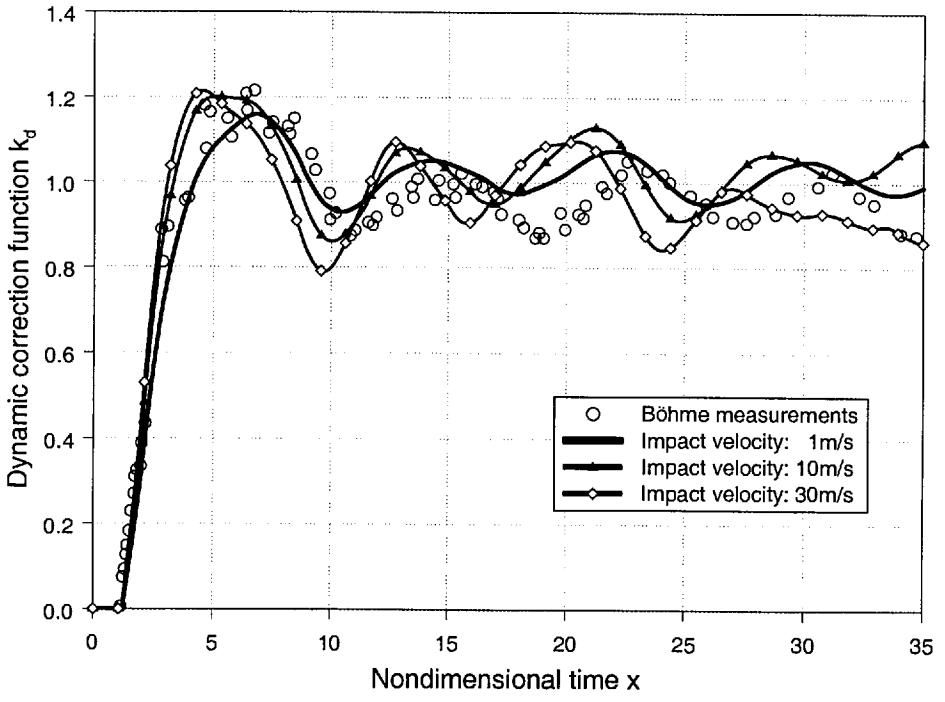

Figure 5.11: The dynamic correction function k_d for impact velocities of 1, 10 and 30m/s compared to Böhme's measurements.

striker radius of 0.002m was analyzed with the FV program for the big specimen with $W = 0.1$m and the k_d curve for this striker radius can be seen in Figure 5.10 together with the curve for a striker radius of $0.008m$ and measurements from [24]. There is some influence of the striker radius, but although the radius was changed by a factor of 4, the impact on the k_d curve is not very high and the initial peak is lowered only by about 5%. Therefore it is obvious that changes in the striker radius in the order of 10%, 20%, or even 50%, as they could happen in practical applications e.g. due to machining inaccuracies or wear of the striker tip, have a negligible effect on k_d.

5.7 The influence of the impact velocity on k_d

Due to the fact that the contact stiffness is nonlinear, the impact velocity can influence the shape of the k_d curve. FV calculations were performed at 10 and 30m/s in addition to the results for 1m/s to investigate the influence of the impact velocity. Figure 5.11 shows these curves and a noticeable influence of the impact velocity on the k_d curve is apparent. A change in impact velocity changes the contact stiffness and therefore the natural frequency of the system. With increasing velocity the load increases and therefore a rise in contact stiffness is observed. This contact stiffness rise makes the system stiffer and increases the natural frequency, which can be seen in the oscillations

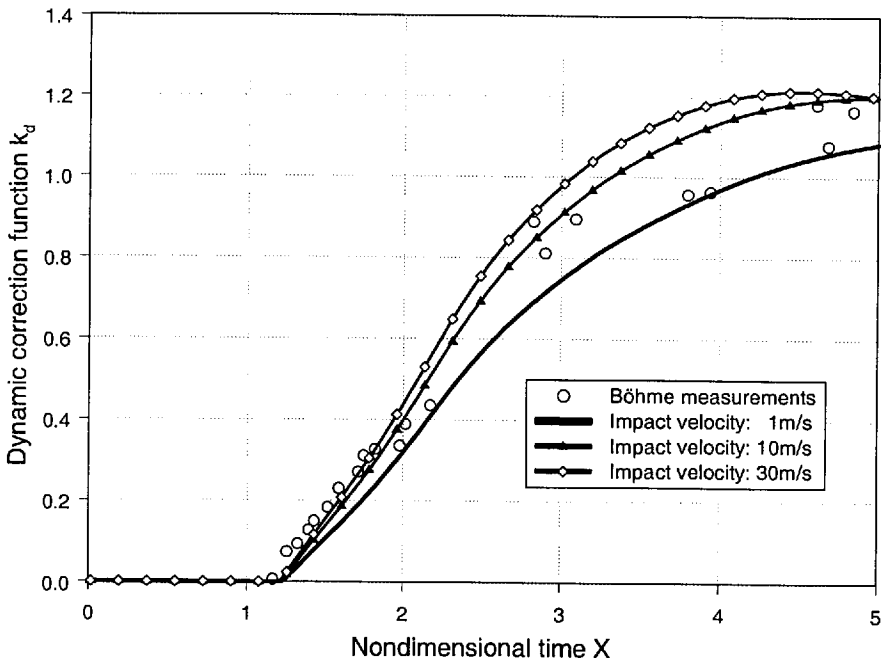

Figure 5.12: The dynamic correction function k_d for impact velocities of 1, 10 and 30m/s compared to Böhme's measurements for $X < 5$.

in Figure 5.11, which shows a shorter oscillation period with rising impact velocity. Furthermore, as a direct effect of the increasing contact stiffness the initial rising part of the k_d curve becomes steeper with impact velocity. Figure 5.12 shows a close-up of the region for $X < 5$. It should be noted here that the measurements for $X < 2.5$ were taken at an impact velocity of 8m/s [24] and these measured points are closer to the k_d curve for 10m/s than the curve for 1m/s. Although the measured k_d values are higher than the results from the FV model, the slope of the measured k_d curve is very similar to the slope of the 10m/s calculation. This shows the velocity dependence of the k_d curve in the experiment.

The impact velocity dependence of the k_d curve implies that one curve determined at a specific impact velocity is, strictly speaking, only valid for this particular velocity. This is similar to an impact response curve [29], which is also only valid for a particular velocity. If a certain amount of error is accepted, a k_d curve can be used for velocities close to the velocity at which it was determined and the bigger the velocity difference, the bigger this error will be.

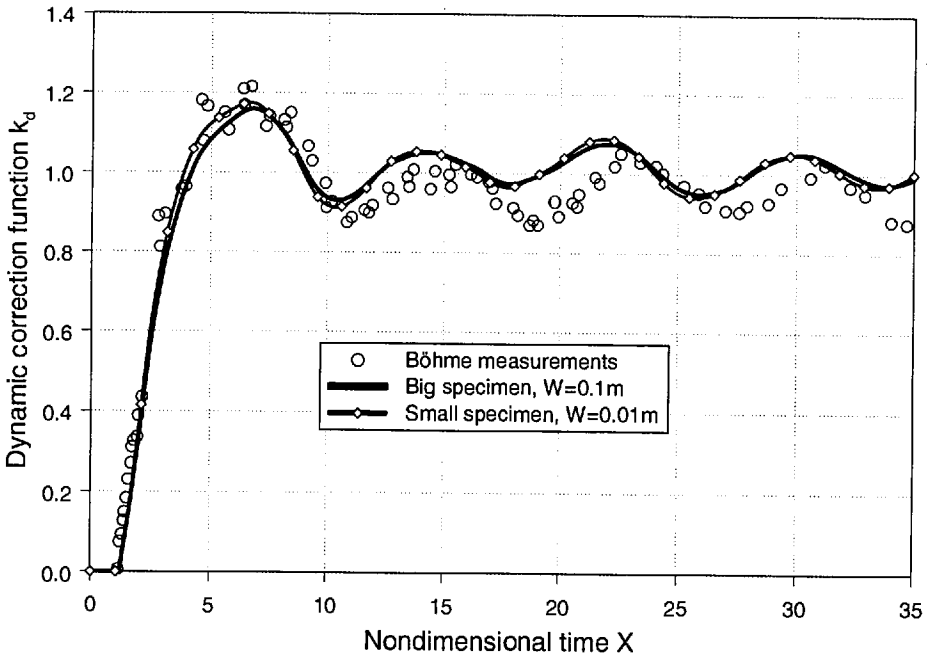

Figure 5.13: The dynamic correction function k_d for two different specimen widths compared to Böhme's measurements.

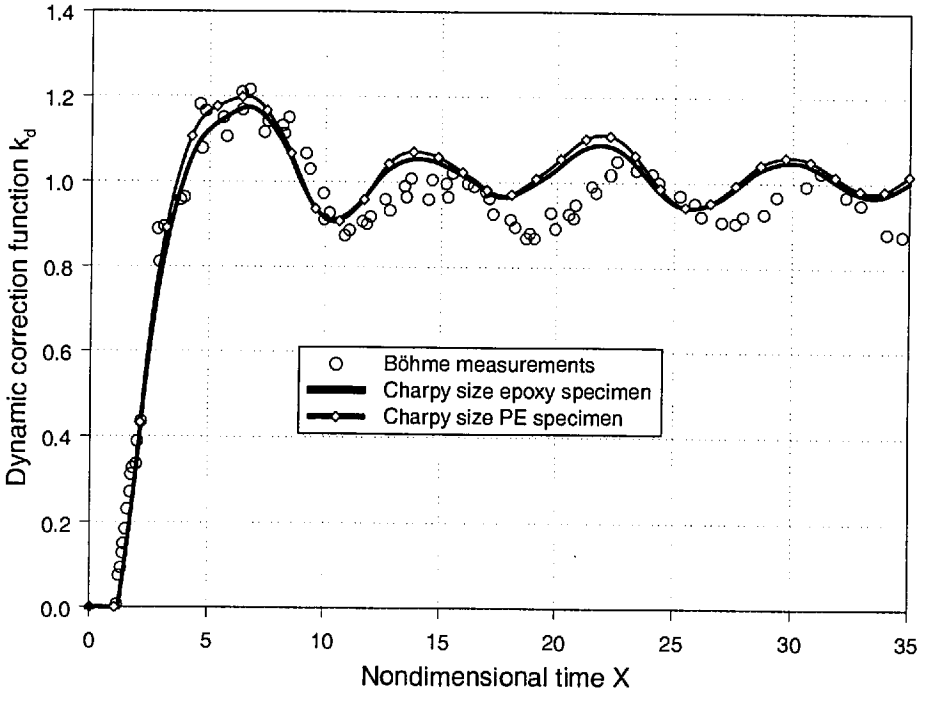

Figure 5.14: The dynamic correction function k_d for two different specimen materials compared to Böhme's measurements.

5.8 The influence of the specimen width on k_d

As discussed in Chapter 4 a k_d curve is not dependent upon the actual specimen width, W, if plotted versus nondimensional time and if a linear contact stiffness is assumed, prevailed that the specimen dimension ratios, a/W, L/W and S/W, are held constant. Even with a nonlinear contact stiffness, the k_d curve is almost independent of the specimen width as can be seen in Figure 5.13. The specimen width is varied here by a factor of 10 and the difference between the two curves is at its maximum 3%. It should be noted that in the case of the big specimen with $W = 0.1$m the striker radius is 0.008m and for the small specimen with $W = 0.01$m the striker radius is 0.002m. The small specimen is of the same size as a Charpy specimen with $a/W = 0.3$ and the big specimen is the specimen size which Böhme used in his experiments, which was 10 times larger than a Charpy specimen in order to make the measurements easier and more accurate. Most practicable specimen sizes lie between the Charpy specimen and the big specimen and hence one k_d curve can be used for these specimen widths with good accuracy.

5.9 The influence of the specimen material on k_d

In most cases a steel, titanium or aluminum striker is used for TPB impact tests on polymers. Therefore the influence of the striker stiffness is negligible as most polymers have an elastic modulus which is of the same order of magnitude as epoxy and hence much lower than the striker modulus. PE is on the lower side of the spectrum of elastic moduli for polymers and therefore it was chosen to show the influence of the elastic modulus of the specimen on the k_d curve. In Figure 5.14 the plots of k_d from a FV analysis of a Charpy size epoxy specimen and a PE specimen are compared. The maximum difference between k_d from the epoxy and the PE specimen is about 3% for a modulus difference of 340%. The impact of the specimen modulus on k_d is therefore fairly small, hence the curve for the epoxy specimen can be used for tests with a 'rigid' striker on different polymers with good accuracy.

5.10 The dynamic correction function g_d from the contact model

As mentioned in Chapter 4 the dynamic correction function g_d can be calculated by squaring k_d (Equation (3.15)). Figure 5.15 compares k_d and g_d from the contact model, which were obtained for the big epoxy specimen ($W = 0.1$m) with steel striker and anvil. In Section 4.7 the dynamic correction function g_d was shown to exhibit a higher degree of dynamic effects than k_d. This is also true for the results from the contact

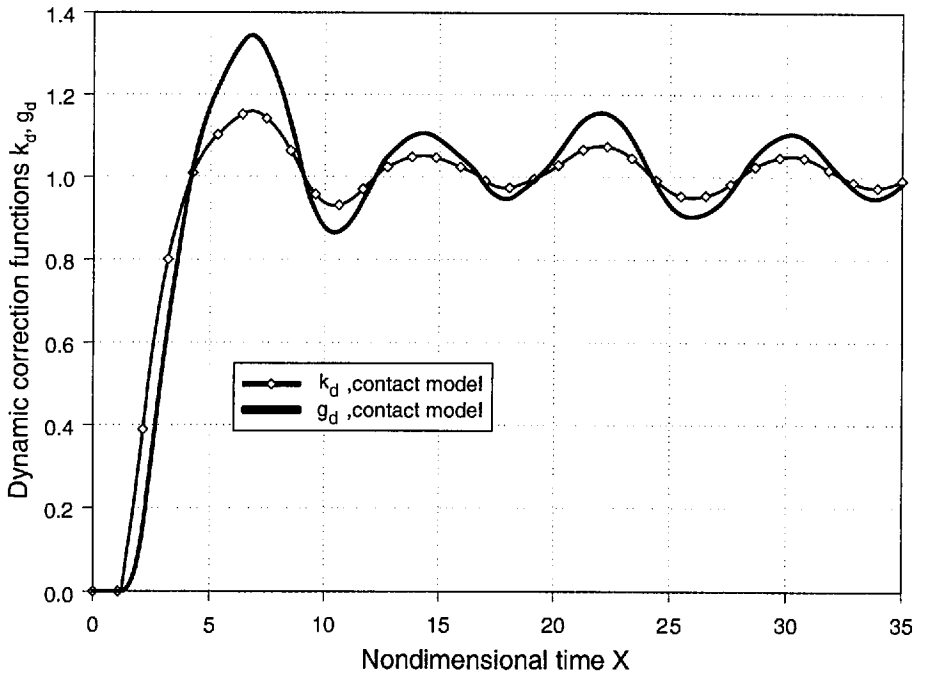

Figure 5.15: The dynamic correction functions k_d and g_d versus nondimensional time for a big epoxy specimen with $W = 0.1$m and steel striker and anvil.

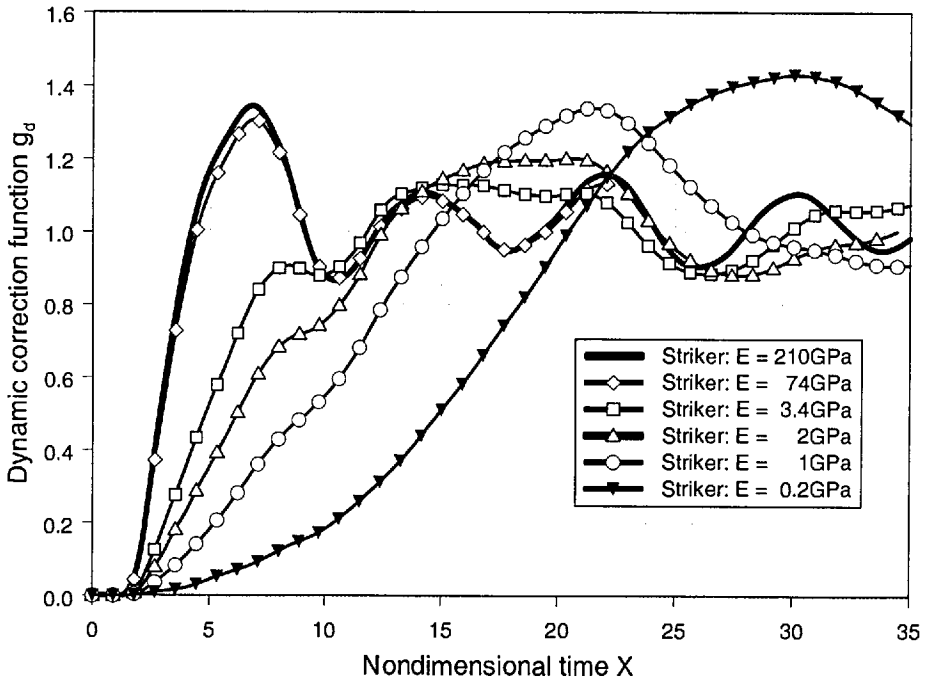

Figure 5.16: The influence of the striker stiffness on the dynamic correction function g_d for a big epoxy specimen with steel anvil.

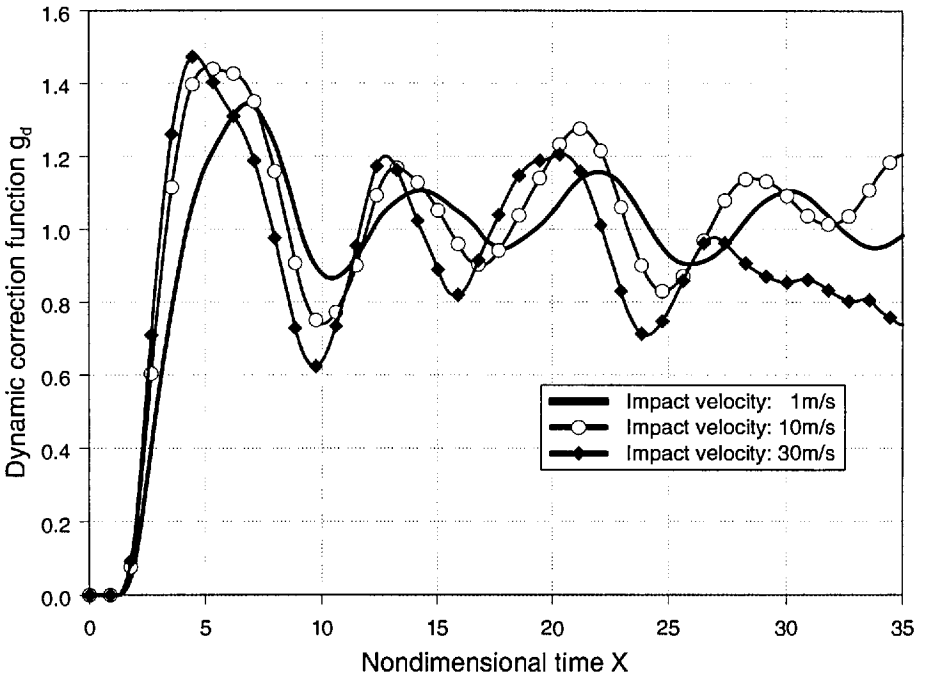

Figure 5.17: The dynamic correction function g_d for impact velocities of 1, 10 and 30m/s and a big epoxy specimen with steel striker and anvil.

model. Due to the fact, that g_d is k_d squared, and that k_d oscillates around unity, the oscillations of the k_d curve are amplified in g_d. For $X < 4.2$ g_d is lower than k_d, but after that g_d shoots up to 1.35 at $X = 6.9$. The slope of g_d for $X < 4.2$ is initially lower than k_d, but then higher, due to the nature of the k_d-g_d conversion. The Figures 5.16 and 5.17 show the influence of the contact stiffness and the impact velocity on g_d. They were calculated from the results shown in Figures 5.11 and 5.8. The dynamic effects are amplified in all the cases and therefore one can say that g_d is more sensitive to a change in the test setup than k_d.

Chapter 6

Finite Volume Analysis of the Center Cracked Panel

6.1 Introduction

In Chapter 1 it was mentioned that the energy release rate G can be defined in a global or a local way. G can be calculated with a global method like the global energy balance and this method was applied to moving cracks in [4]. If there is no crack advance i.e. in case of a stationary crack, the global energy balance cannot be applied. In the case of a stationary crack G is the energy which would be available if the crack would advance. The crack tip closure integral is, in comparison to the global energy balance, a local method and can be used for a stationary crack. It is based on the assumption that if a crack is extended by a small amount, the energy absorbed in the process is equal to the work required to close the crack back to its original length. To find out whether the global and the local energy release rate calculations agree, the dynamic J integral can be used. The dynamic J integral can be applied to any path surrounding the crack, whether there is a crack advance or not. Depending upon the path along which the integral is evaluated this method can be seen either as a global method, when the path coincides with the boundary of the domain, or as a local method, if the path is close to or shrunk onto the crack tip. Therefore the J integral is an appropriate method to show that the global and the local calculation indeed yield the same results, independent of the chosen path. Due to the fact that even the simple model of the TPB test from Chapter 4 has a large number of cells and since it is a bending problem it takes a long time to converge. Nevertheless the mesh was found not to be fine enough to give good results when the J integral was applied. Therefore a different test case was sought to compare the J integral method with the crack closure integral method. A center cracked panel with a stress step applied was chosen, as this problem is easy to solve and there are also results available in the literature for comparison. In this chapter g_d curves for

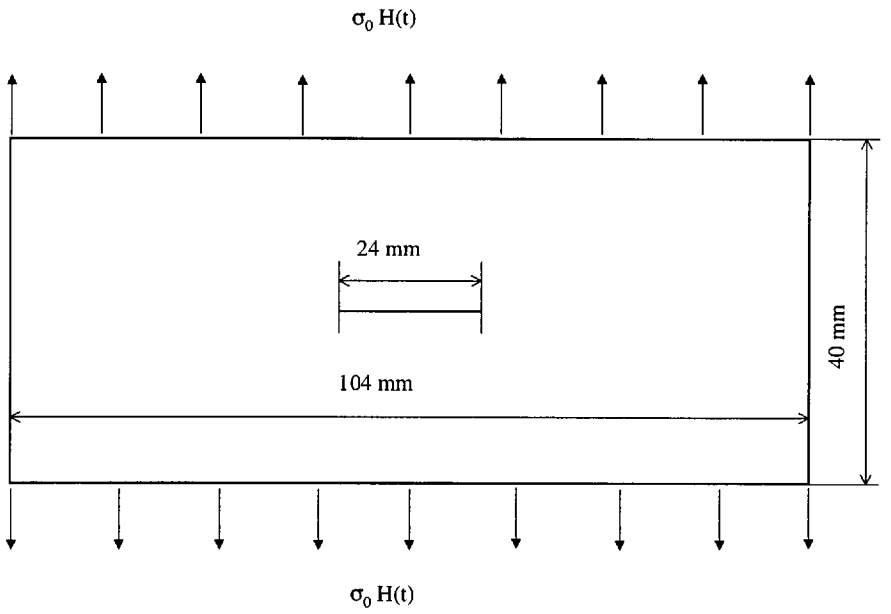

Figure 6.1: The center cracked panel.

the center cracked panel from three different paths are compared with g_d from crack tip closure and a comparison with results from the literature is also performed.

6.2 The finite volume model of the center cracked panel

Results for a center cracked panel were found in [83, 8] and in order to allow comparison with these results the same panel size and material properties were chosen. The panel is shown in Figure 6.1 and only a fourth of the panel had to be modeled for symmetry reasons. The part of the panel which was modeled is displayed in Figure 6.2 together with the three paths, which were chosen for the J integral evaluation. The panel had a length of 0.104m, a height of 0.04m and a crack length, a, of 0.024m. The material properties were taken from [8] as $E = 75.61\text{GPa}$, $\nu = 0.286$ and $\rho = 2450\text{kg/m}^3$. Four different meshes were used and the first, the coarse mesh, had 260 square cells. Then each cell of the coarse mesh was split into four cells for the medium mesh with a total number of cells of 1040. This mesh was then refined again by a factor of four to the fine mesh with 4160 cells. By applying another refinement step a very fine mesh with 16640 cells was generated. For all these meshes a dynamic FV analysis was performed for the duration of $20\mu\text{s}$ after a uniformly distributed stress step $\sigma_0 H(t)$, where $H(t)$ is the Heavyside function, with $\sigma_0 = 1\text{MPa}$ was applied on the top and bottom ends of the panel parallel to the crack. The crack was assumed to be stationary under this time-dependent loading. The time step for the FV analysis with the coarse mesh was

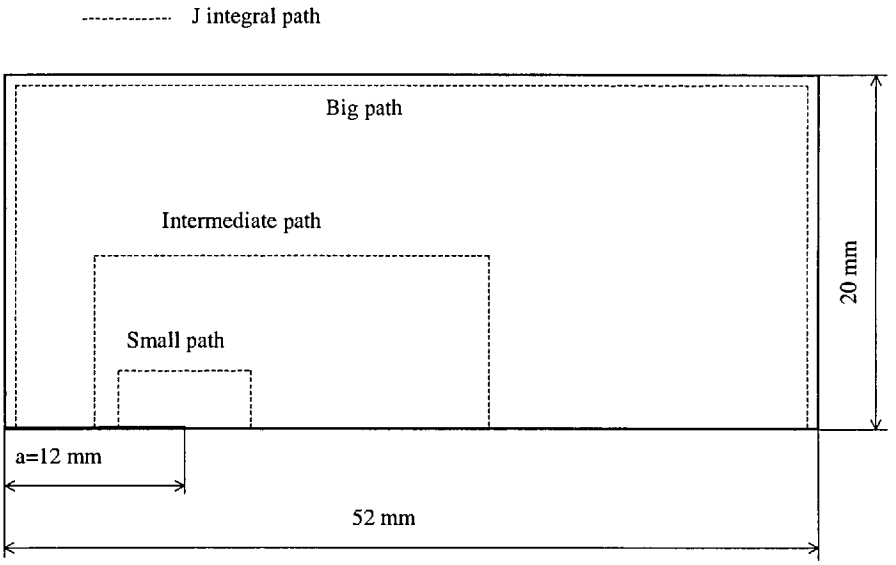

Figure 6.2: The three different paths used for the J integral evaluation.

0.1μs. For the FV analysis with the medium mesh the time step was halved to 50ns, the fine mesh had a time step of 25ns and for the very fine mesh a time step of 12.5ns was used. The FV program was operated in a 2D plane stress mode, where the front and back faces were defined as stress free.

6.3 Comparison of g_d from the dynamic J integral and the crack closure integral

In Figures 6.3 to 6.6 the g_d curves from the crack closure integral and the dynamic J integral for the four different meshes with increasing mesh refinement are presented. For the coarse mesh (Figure 6.3) it is immediately obvious that different J integral paths yield very different results. The further away the path is from the crack tip, the bigger the differences are. Obviously this mesh is too coarse for an accurate result of the J integral method. This is only a numerical problem, as the J integral method is apparently quite mesh sensitive. The crack closure integral results are already very accurate, even for this coarse mesh, which will be discussed later. The small path, which is closest to the crack tip, gives the best results and follows the crack tip closure results closely in the first third of the curve. The results from the medium mesh (Figure 6.4) show improvement and approach the crack tip closure results. Only the big path close to the edge of the domain yields values, which are initially far too high. The intermediate

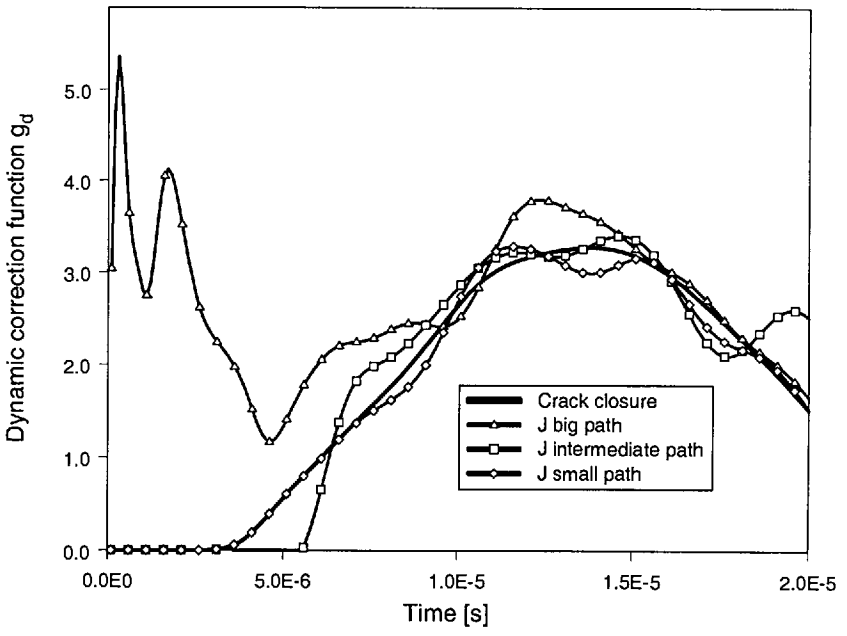

Figure 6.3: The dynamic correction function g_d for the coarse mesh from the crack closure integral method compared with results from the dynamic J integral from three different paths.

path shows some oscillations as well. The curve for the small path is already very close to the crack tip closure curve. Moving on to the fine mesh in Figure 6.5 there is almost complete agreement of all J integral path solutions with the crack tip closure result. For the very fine mesh in Figure 6.6 all four curves agree very well. Therefore one can say that the dynamic J integral yields the same result as the crack tip closure in this case of a stationary crack with transient loading. Figure 6.7 shows the crack tip closure results for all four different meshes. The difference between the results for different meshes is very small. The coarse mesh shows some higher results between 12 and 17μs, but even there the difference is only about 3%. The curves for the other three meshes are very close. The conclusion that one can draw is that the crack closure integral method is quite a mesh insensitive method for calculating K and G, whereas the J integral is very demanding in this respect. The mesh insensitivity together with the fact that the crack tip closure integral method is very easy to implement in a computer program makes this method superior to the dynamic J integral.

The results demonstrate that the crack tip closure integral yields valid results for G, which agree with the dynamic J integral and further, that the dynamic J integral yields the same results, whichever path is chosen, as long as the mesh is fine enough. Therefore no difference between local G and global G was found.

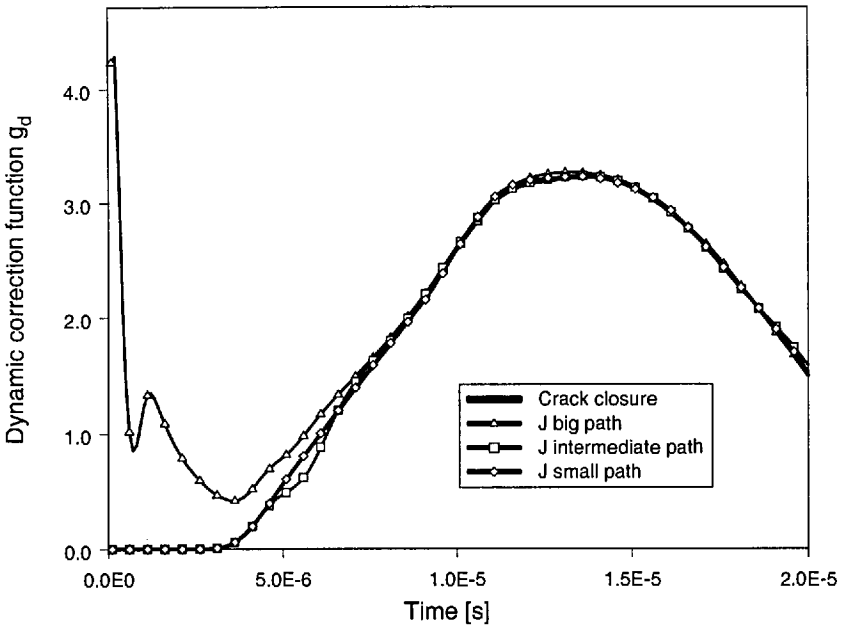

Figure 6.4: The dynamic correction function g_d for the medium mesh from the crack closure integral method compared with results from the dynamic J integral from three different paths.

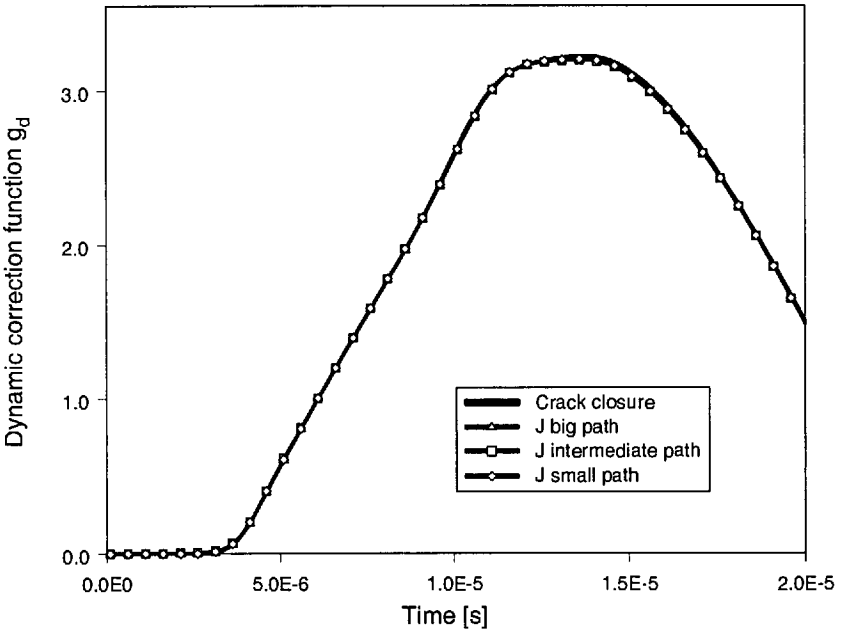

Figure 6.5: The dynamic correction function g_d for the fine mesh from the crack closure integral method compared with results from the dynamic J integral from three different paths.

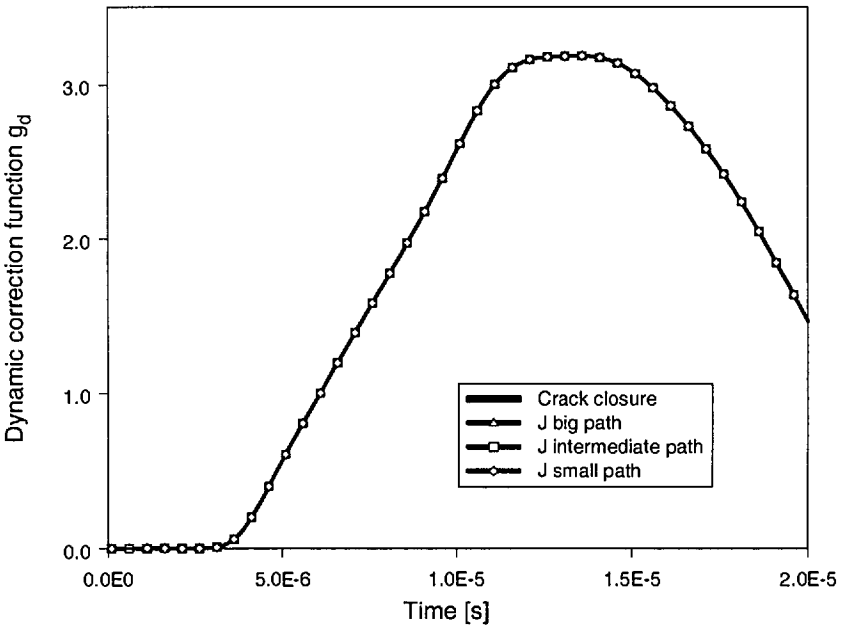

Figure 6.6: The dynamic correction function g_d for the very fine mesh from the crack closure integral method compared with results from the dynamic J integral from three different paths.

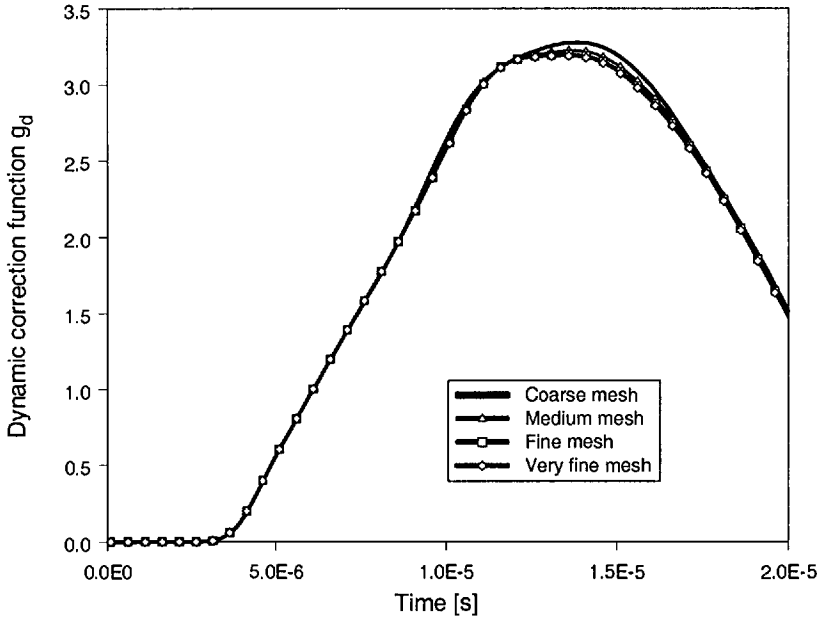

Figure 6.7: The dynamic correction function g_d from the crack tip closure integral method for all four meshes.

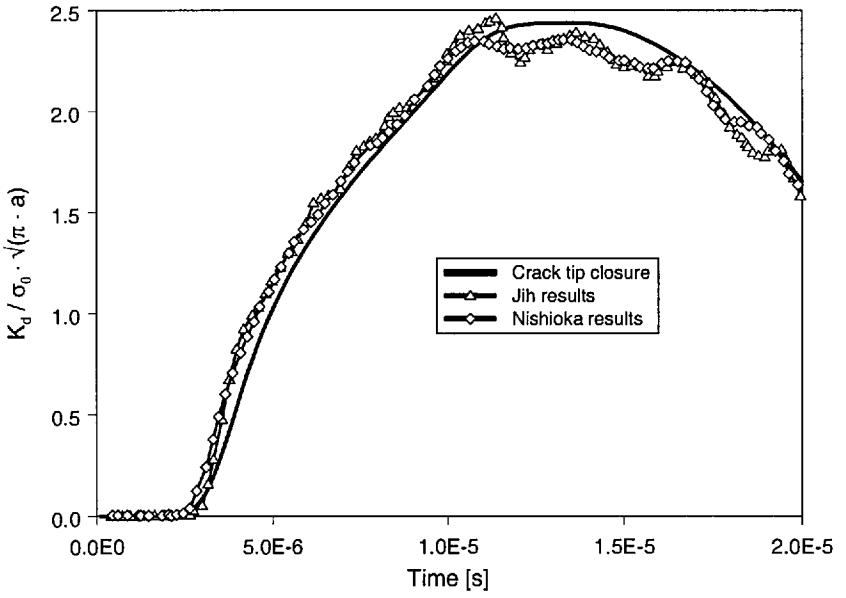

Figure 6.8: The dynamic stress intensity factor K_d divided by the static infinite plate solution for the results from crack tip closure compared with results from Jih [8] and Nishioka [83].

6.4 Comparison between K_d from the crack closure integral with results from the literature

The dynamic SIF from the crack closure integral normalized with the SIF for the infinite plate is shown in Figure 6.8. Also shown in this graph are two previous solutions by Nishioka [83] and Jih [8], obtained by employing the finite element method with an implicit Newmark time integration scheme. The curve from Nishioka [83] was calculated from a singular element method and Jih [8] calculated K from the crack closure and the dynamic J integral method, which was evaluated with a small path close to the crack tip. The FV results are quite close to the FE results, although a bit lower in the initial rising part of the curve. In the FE results high-frequency oscillations are visible, whereas the FV results are very smooth. The oscillations in the FE results are thought to be of numerical nature, as the smallest possible physical oscillation period would be 6.9μs for a longitudinal wave reflected between the edge of the panel and the crack surface. The oscillation period for a wave being reflected between the top and bottom of the plate would be 13.8μs. The FE results rise faster, but show ringing, whereas the FV results exhibit more numerical damping.

Chapter 7

K_d and G_d from Time to Fracture

7.1 Introduction

A test series of three materials tested at impact velocities ranging from 0.2m/s to 27m/s was presented in Chapter 2. These results were presented there as time to fracture, t_s, versus impact velocity. Although this led to some interesting conclusions, the main aim of the TPB impact test is the determination of the dynamic fracture toughness, K_d, and the dynamic critical energy release rate, G_d. Based on the finite volume results from Chapter 4 and 5, this chapter describes a procedure to obtain K_d and G_d from time to fracture.

7.2 The calculation of K_d and G_d from t_s

Although most equations necessary for the calculation of K_d and G_d were presented in Chapter 1 they are shown again here for clarity.

The quasistatic fracture toughness can be calculated from the time to fracture t_s with (Equation 1.21)

$$K_{st} = \frac{f}{\psi} \frac{E}{W^{\frac{1}{2}}} \frac{V t_s}{\left(1 + \frac{1}{\alpha}\right)} \tag{7.1}$$

where E is the elastic modulus of the specimen, V is the impact velocity and α is the stiffenss ratio

$$\alpha = \frac{k_1}{k_2} \tag{7.2}$$

with the contact stiffness k_1 and the specimen stiffness k_2. f is a geometry factor and for a SENB geometry with a span, S, to width, W, ratio of $S/W = 4$ and for a crack

length ratio a/W between 0 and 1 we find

$$f = \frac{6\left(\frac{a}{W}\right)^{\frac{1}{2}}\left(1.99 - \left(\frac{a}{W}\right)\left(1 - \left(\frac{a}{W}\right)\right)\left(2.15 - 3.93\left(\frac{a}{W}\right) + 2.7\left(\frac{a}{W}\right)^2\right)\right)}{\left(1 + 2\left(\frac{a}{W}\right)\right)\left(1 - \left(\frac{a}{W}\right)\right)^{\frac{3}{2}}}. \tag{7.3}$$

ψ is the dimensionless specimen compliance after Bucci [32] with

$$\begin{aligned}\psi = 0.24\left(\frac{S}{W}\right)^3 &\left(1.04 + 3.28\left(\frac{W}{S}\right)^2(1+\nu)\right) + 2\left(\frac{S}{W}\right)^2\left(\frac{a}{W}\right) \\ &\left(4.21\left(\frac{a}{W}\right) - 8.89\left(\frac{a}{W}\right)^2 + 36.9\left(\frac{a}{W}\right)^3 - 83.6\left(\frac{a}{W}\right)^4 + 174.3\left(\frac{a}{W}\right)^5\right. \\ &\left. -284.8\left(\frac{a}{W}\right)^6 + 387.6\left(\frac{a}{W}\right)^7 - 322.8\left(\frac{a}{W}\right)^8 + 149.8\left(\frac{a}{W}\right)^9\right)\end{aligned} \tag{7.4}$$

where ν is the Poisson's ratio. Equation 7.1 yields the fracture toughness value before any dynamic correction. It is linearly dependent on E and t_s and it also depends on α. As discussed in Chapter 5 the contact stiffness changes nonlinearly with the applied displacement. Previous studies [84, 40] yielded values for α between 9 and 11.4 for an epoxy specimen with $W = 0.013$m and a titanium striker with a tip radius of 2mm. A variation of α between 9 and 12 affects K_{st} only by about 2%. For polymers with different modulus α can be expected to be fairly similar, as k_1 as well as k_2 are affected by a change in modulus. The comparison between the epoxy and the PE specimen from Figure 5.14 shows the similarity of the curves for the different specimen materials, which means a similar stiffness ratio α. A value of $\alpha = 10$ was used in this study for the three tested polymers.

From the fracture time from the strain gauge t_s, a nondimensional time X can be calculated with

$$X = X_0 + \frac{c_l t_s}{W} \tag{7.5}$$

where X_0 is the starting point of the k_d curve on the x-axis, W is the specimen width and c_l is the longitudinal wave speed with

$$c_l = \left(\frac{E}{\rho(1-\nu^2)}\right)^{\frac{1}{2}} \tag{7.6}$$

where ρ is the density and ν is the Poisson's ratio. X_0 is determined by the time a transverse wave needs to reach the crack tip from the point of the striker impact at midspan. X_0 can be obtained from a k_d versus X graph and we find $X_0 = 1.2$ for a SENB test and $a/W = 0.3$ in Figure 7.1.

With the nondimensional time at fracture, X, the dynamic fracture toughness can be calculated with

$$K_d = k_d(X) \cdot K_{st} \tag{7.7}$$

where k_d is a suitable dynamic correction function for the particular specimen geometry and test conditions (Section 3.7).

The static energy release rate G_{st} can be calculated from K_{st} via

$$G_{st} = \frac{K_{st}^2}{E} \tag{7.8}$$

and analog to Equation 7.7 G_d can then be calculated with

$$G_d = g_d(X) \cdot G_{st} \tag{7.9}$$

where g_d is the dynamic correction function for G, which was described in Section 3.7.

7.3 The elastic modulus

The elastic modulus of the specimen is important for the evaluation of K_d and G_d from time to fracture. Both K_{st} and G_{st} depend linearly on the specimen modulus E. The amount of dynamic correction is also affected by E, as X is a function of $E^{0.5}$ via the longitudinal wave speed and the X value affects the dynamic correction i.e. the position on the k_d curve. The elastic modulus of some polymers is known to be rate sensitive. In many cases the modulus increases with rate and this leads to an increase of K_d and G_d with rising impact velocity. Initial experiments to obtain values for the rate-dependent modulus during the ESIS TC4 round robin showed a large scatter between different laboratories and methods and were abandoned, as it was found that the accurate determination of the rate dependent modulus would need a separate research project. Therefore low rate modulus values were used for the calculation of K_d and G_d. Quasistatic TPB tests at 1.3mm/min were carried out on three specimen per material for PMMA and PVC and the mean values were taken. A modulus of 2.96GPa was found for PMMA and for PVC a modulus of 3.05GPa was obtained. From previous measurements by S. Hazra at Imperial College [85] the modulus of the pipe-grade PE was known to be 1GPa.

7.4 The determination of the dynamic correction

As discussed in Chapter 5 the shape of the k_d curve depends upon the contact stiffness. A k_d curve can be used for different specimen widths with good accuracy. A change in the specimen modulus also does not affect the k_d curve greatly if the specimen is a polymer specimen and a metal striker is used. However, the impact velocity has a significant influence on the k_d curve and some form of correction for this influence can be necessary to keep the error small. If there is a large difference between the impact

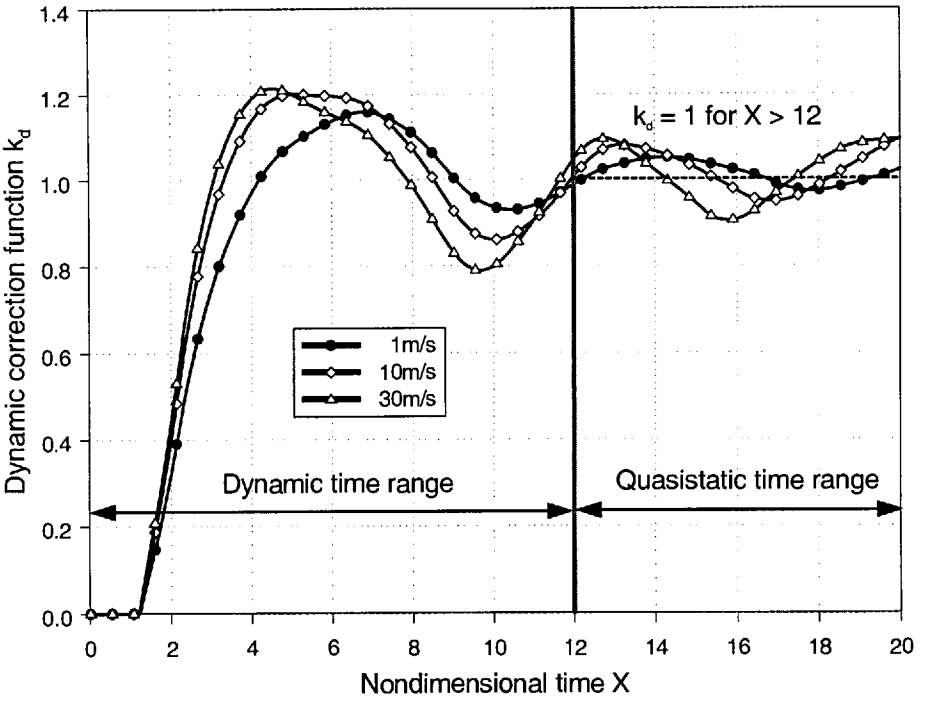

Figure 7.1: The dynamic correction function k_d for impact velocities of 1, 10 and 30m/s and the concept for the k_d determination.

velocity at which the k_d curve was determined and the impact velocity at which the test is performed, a correction is necessary. In the test series presented in Chapter 2 the impact velocity varies between 0.2 and 27m/s. We can see from Figure 7.1, which shows the curves presented in Section 5.7, that there is a big difference between the k_d curves for 1 and 30m/s and hence there is a need for a velocity dependent k_d curve. A simple concept was therefore used to obtain values for the dynamic correction for different impact velocities (Figure 7.1). For $X > 12$ a quasistatic time range is defined, where no dynamic correction is applied and hence $k_d = 1$. A dynamic time range is defined for $X < 12$ and a dynamic correction is applied. This dynamic correction takes into account the velocity influence on k_d with a linear interpolation for the actual test velocity between the k_d values for 1, 10 and 30m/s. For example for $V = 2$m/s and $X = 3$, a linear interpolation at $X = 3$ between the k_d values for 1 and 10m/s is performed, which yields an approximation of the k_d value for 2m/s.

Polynomial curve fits of the k_d curves for 1, 10 and 30m/s were performed with a least squares procedure for X between 1.22 and 12. These curve fits can be used to obtain a k_d value for a specific impact velocity and X value. The polynomials are of the form

$$f(X) = \sum_{i=0}^{N} b_i X^i \tag{7.10}$$

Table 7.1: Polynomial coefficients.

Coefficient	1m/s	10m/s	30m/s
b_0	1.39633163	1.35992392	1.18420293
b_1	-3.53165057	-3.47395435	-3.02602141
b_2	3.13176244	2.99267672	2.47642342
b_3	-1.25022024	-1.07780992	-7.37938420E-01
b_4	2.82569960E-01	2.01513620E-01	7.62253600E-02
b_5	-3.88005100E-02	-1.94281600E-02	7.45259516E-03
b_6	3.28060344E-03	6.53570264E-04	-2.79680250E-03
b_7	-1.66227978E-04	3.89838867E-05	3.00348303E-04
b_8	4.62332167E-06	-3.99235643E-06	-1.47652362E-05
b_9	-5.44038813E-08	9.62883560E-08	2.82499880E-07

where b_i are the polynomial coefficients, which are displayed in Table 7.1 for 1, 10 and 30m/s and $N = 9$. For sufficient accuracy a 9^{th} order polynomial had to be used. Between $2.2 < X < 12$ the curve fits do not deviate more than $\pm 1.2\%$ from the numerical curves from Figure 7.1. From $1.6 < X < 2.2$ the curve fit stays within a $\pm 3\%$ envelope. Only for very small times to fracture ($X < 1.6$), the curve fit does not yield accurate results, as the relative error becomes too high.

The scheme presented above is a modified version of Böhme's concept [31, 61], where the k_d curve was divided in a quasistatic and a dynamic time range and for the dynamic time range a polynomial approximation of the k_d curve for $V = 1$m/s was used. Böhme used $X = 9.2$ for the division between the dynamic and quasistatic time range, as his k_d curve was equal to 1 at this time and after this time the k_d curve stays within a $\pm$ 10% envelope. In this work, $X = 12$ was used, as the dip around $X = 10$ becomes deeper with impact velocity and hence a dynamic correction is also necessary in this region.

Figure 7.2 shows the test results from Chapter 2, now converted into nondimensional time X, plotted against impact velocity. Due to small times to fracture, the results for PMMA are in the dynamic time range for impact velocities greater than 3m/s. For high impact velocities of more than 6m/s the X values are in the dynamic time range for all three tested materials. This means that, although deviations from $k_d = 1$ are outside the $\pm$ 10% envelope for $X > 12$ and $V = 10, 30$m/s, they do not matter for the calculation of the results, as the materials tested fail at low X values ($X < 8$) at these velocities anyway.

Figure 7.3 shows the amount of dynamic correction for each test. Due to the nature of the correction, significant dynamic correction values are found only from 4m/s onwards. Due to the high fracture time, the dynamic correction for PE is greater than 1 at high

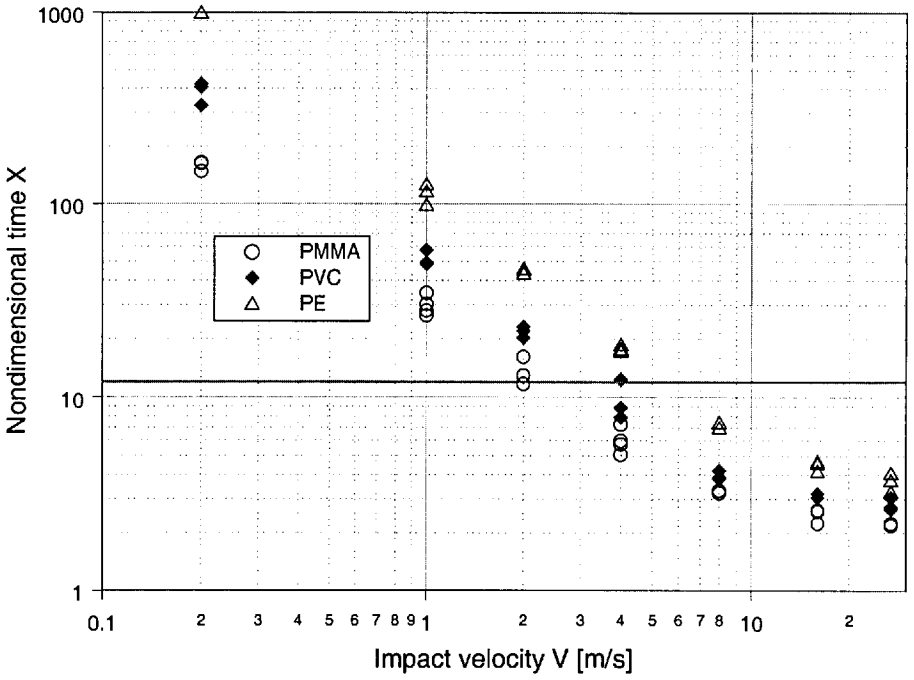

Figure 7.2: The nondimensional time X for the tests for PMMA, PVC and PE versus impact velocity.

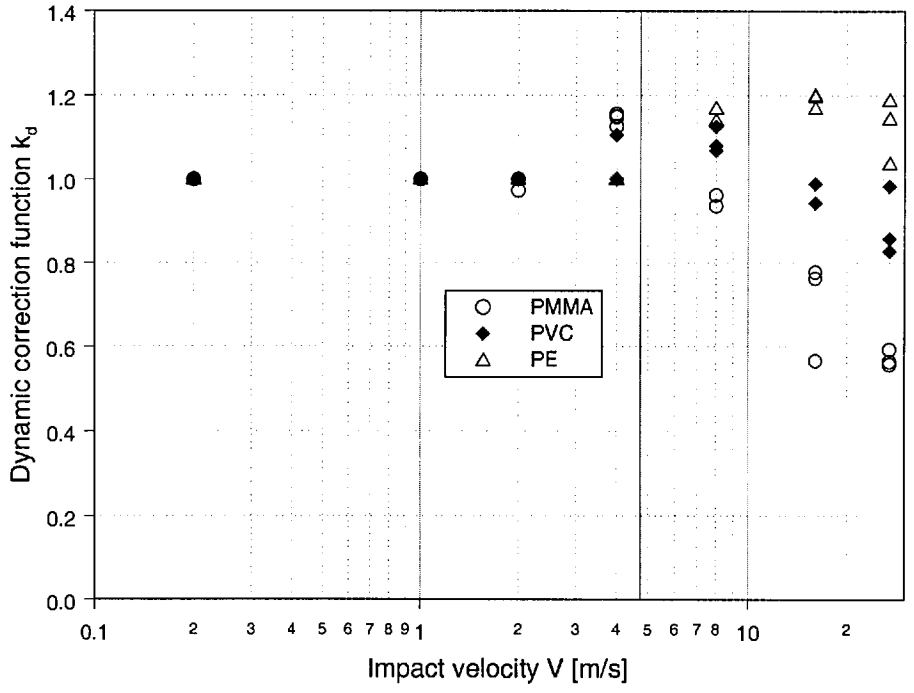

Figure 7.3: The value of dynamic correction for the tests for PMMA, PVC and PE versus impact velocity.

velocities, whereas PMMA and PVC show a reduction of K_{st} in K_d i.e. a dynamic correction with $k_d < 1$ at 16 and 27m/s.

7.5 The sensitivity of K_d and G_d to errors in t_s

Errors in t_s can arise from inaccuracies in the measurement of fracture time. A certain amount of error will therefore always be present in t_s and it is important to know the effect of the error of t_s on K_d and G_d. In Chapter 2 it was found that the average error of t_s can be considered to be about 10%. Due to the high slope in the initial part of the k_d curve, K_d is very sensitive to errors in t_s in this region. An error analysis showed that for $X = 2$, which is the worst case which can happen (the smallest time to fracture and the steepest part of the curve), and an error on t_s of $\pm 10\%$, the error on k_d will be $\pm 29\%$. K_{st} will also be affected, but as K_{st} is linear with t_s, the error on it will be $\pm 10\%$ also. The error on K_{st} and t_s together yield an error of $+41\%/-34\%$ on K_d. The total error is hence magnified from 10% to 41% in the worst case. This is quite a big error and clearly the method needs improvement. If the error is random error and not systematic, then taking several measurements at the same impact velocity and averaging them will clearly improve the accuracy of the K_d value. In this study three replications at most velocities were performed and from these a mean value was computed. As G_d is proportional to K_d^2, the error on it will be more pronounced than the error on K_d. The error on G_d for the $\pm 10\%$ error on t_s will be $+100\%/-59\%$, which is rather large. This is expected as it was found in Section 4.7 that g_d and hence G_d is a more sensitive parameter than K_d. We can conclude here that the error on t_s can be enlarged by a factor of 4 in the worst case for K_d and by a factor of 10 for G_d. Therefore a very accurate detection of the fracture time is needed in conjunction with averaging of several measurement points per velocity to obtain accurate K_d and G_d values.

7.6 The dynamic fracture toughness results

Figures 7.4 to 7.6 show the dynamic fracture toughness K_d for the three polymers tested. The graphs show the individual measurements as well as the mean toughness values for each velocity. The toughness values for PMMA in Figure 7.4 show quite a big scatter, especially from 1 to 4m/s. This scatter comes from the scatter in t_s, which is magnified by the data evaluation procedure, as discussed in Section 7.5. The averaging procedure brings more clarity in the results and we find a falling fracture toughness up to 8m/s, where K_d levels off at about 0.6MPam$^{0.5}$. For PVC in Figure 7.5 we find falling toughness values up to a minimum of 1.1MPam$^{0.5}$ at 8m/s and then the toughness rises again with impact velocity. The observed scatter is lower for PVC than for PMMA.

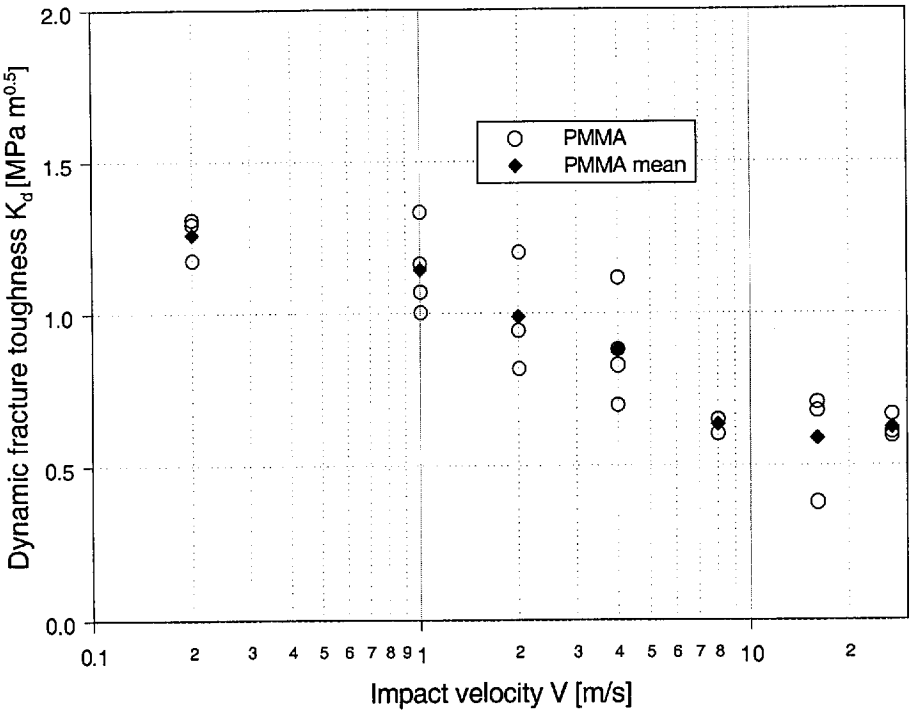

Figure 7.4: The dynamic fracture toughness K_d for PMMA with the mean value for each impact velocity.

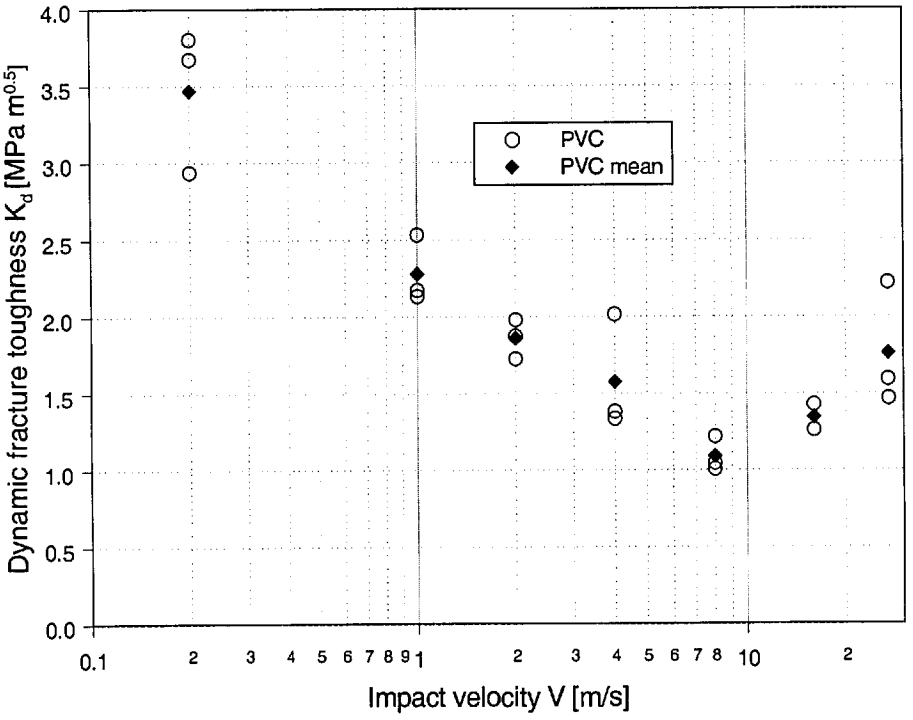

Figure 7.5: The dynamic fracture toughness K_d for PVC with the mean value for each impact velocity.

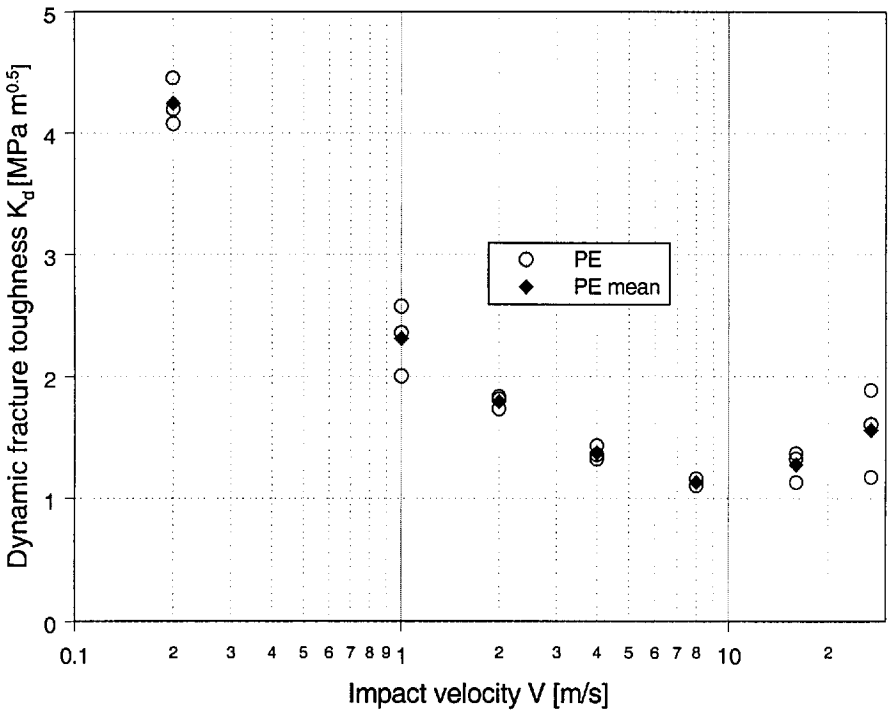

Figure 7.6: The dynamic fracture toughness K_d for PE with the mean value for each impact velocity.

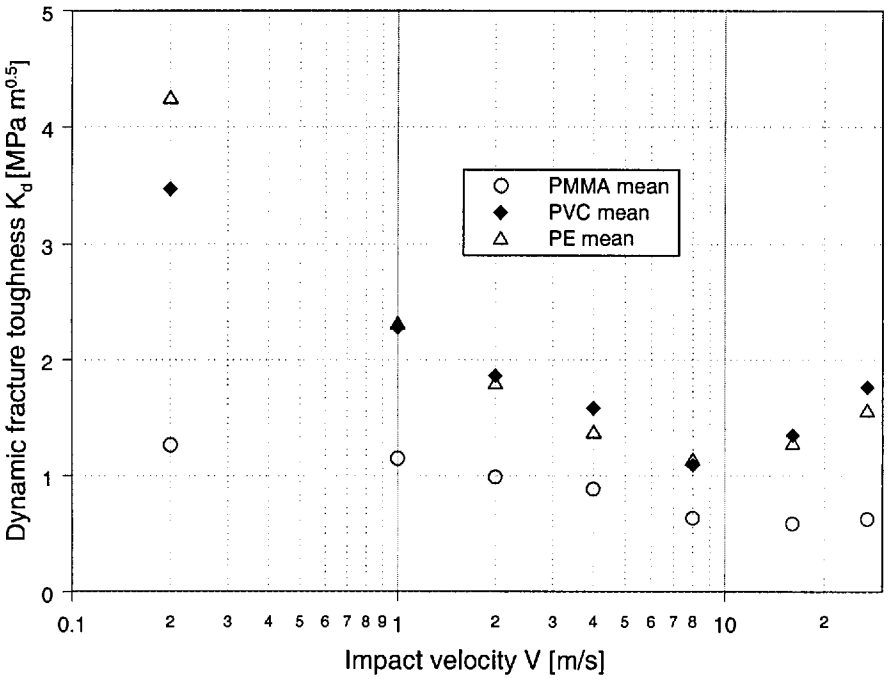

Figure 7.7: The mean dynamic fracture toughness K_d for each velocity and for all tested materials.

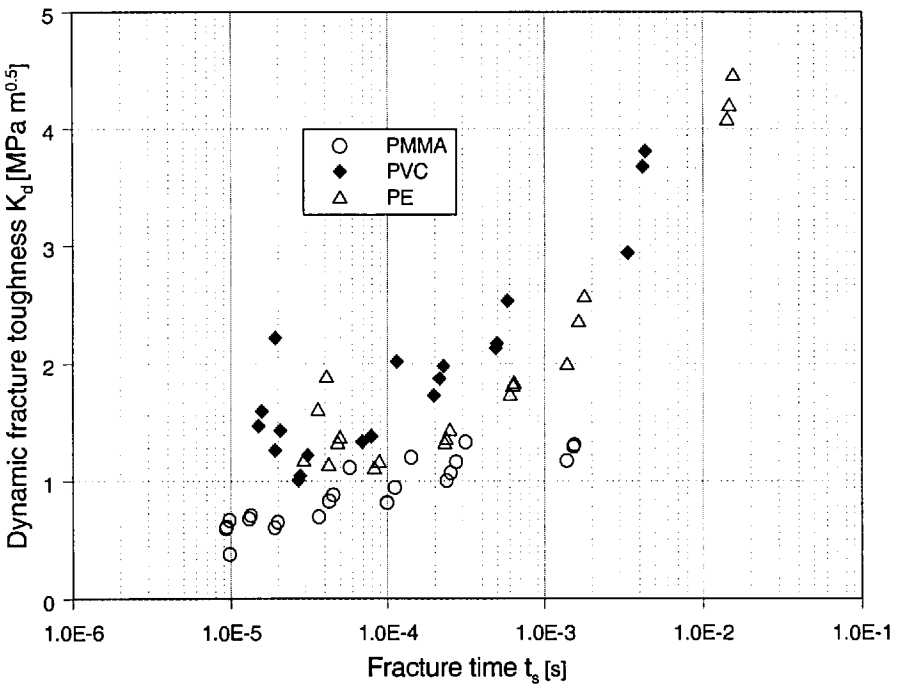

Figure 7.8: The dynamic fracture toughness K_d versus fracture time.

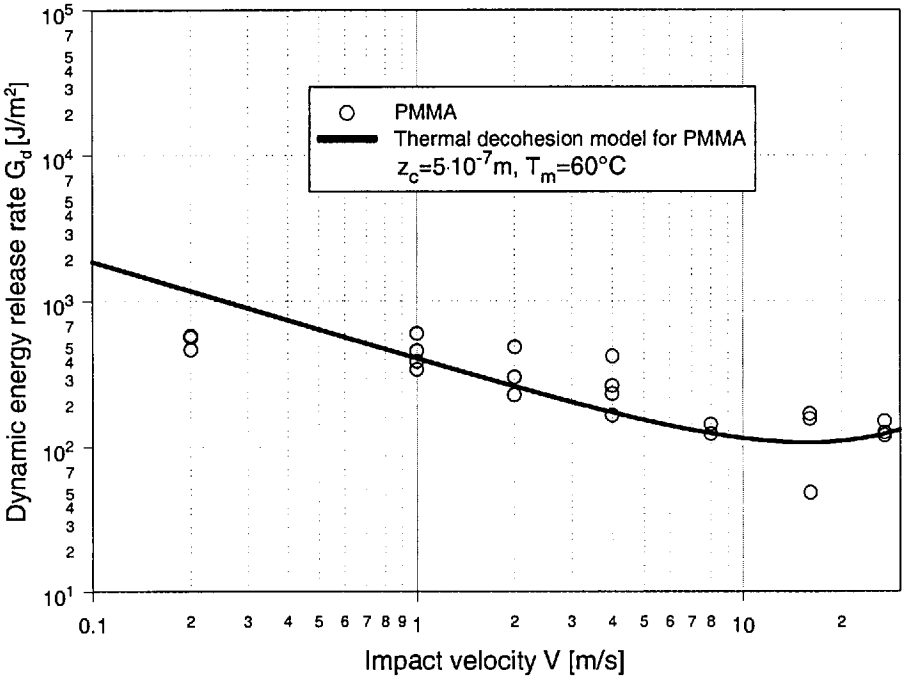

Figure 7.9: The dynamic energy release rate G_d for PMMA together with a fit with a thermal decohesion model.

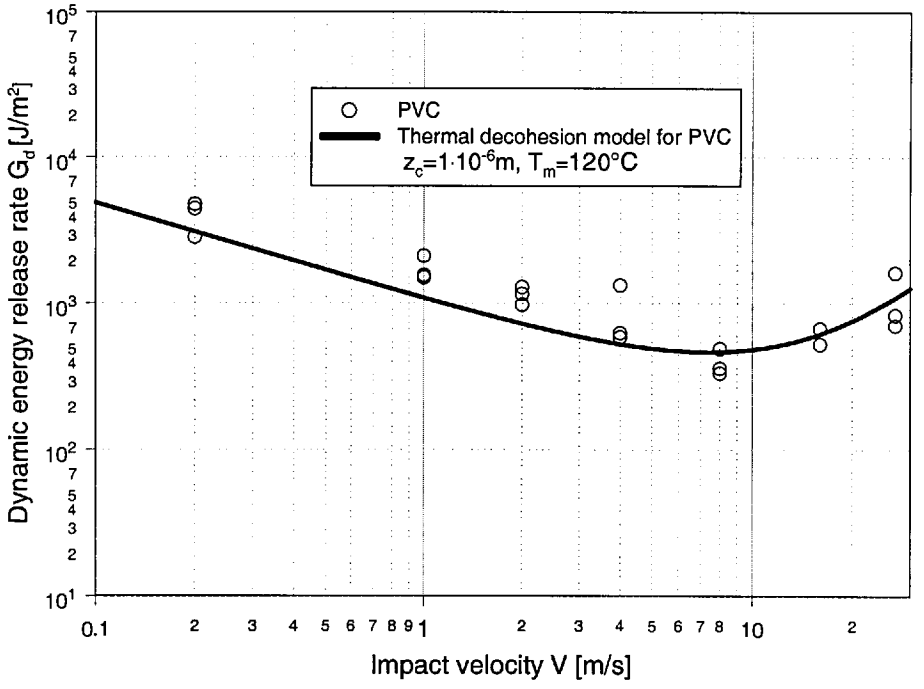

Figure 7.10: The dynamic energy release rate G_d for PVC together with a fit with a thermal decohesion model.

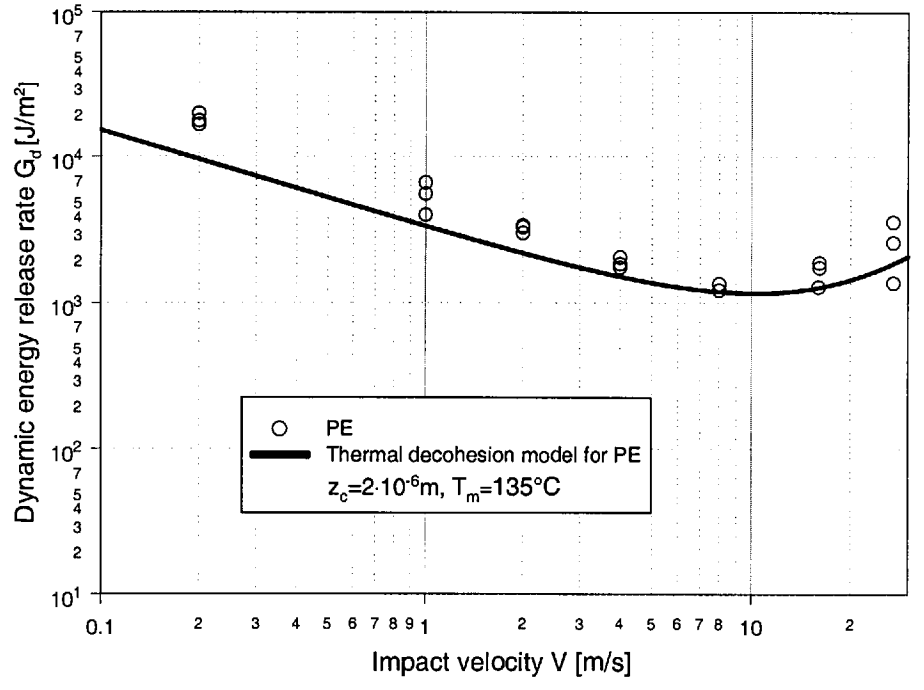

Figure 7.11: The dynamic energy release rate G_d for PE together with a fit with a thermal decohesion model.

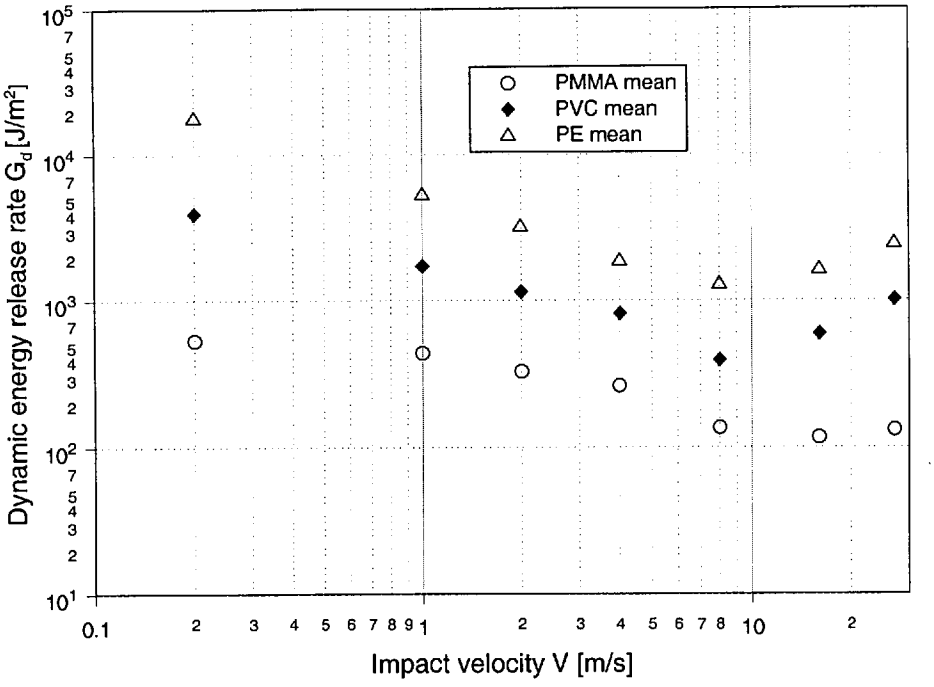

Figure 7.12: The mean dynamic energy release rate G_d for each velocity and for all tested materials.

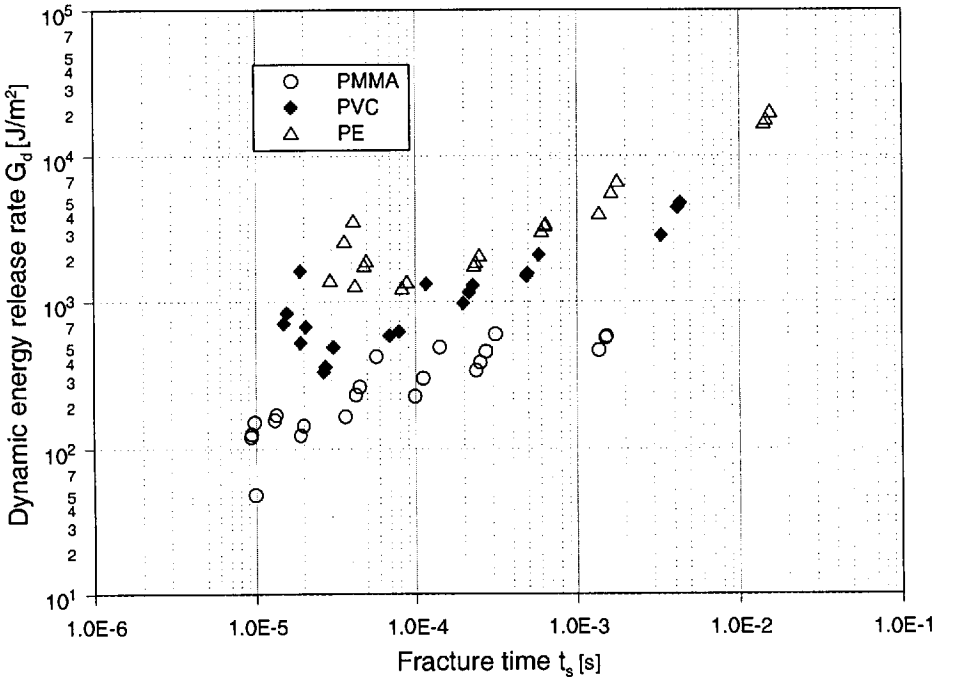

Figure 7.13: The dynamic energy release rate G_d versus fracture time.

For PE the scatter is even more reduced (Figure 7.6) and it also exhibits a tendency of a minimum toughness of 1.1MPam$^{0.5}$ at an impact velocity of 8m/s and then the toughness increases again for $V > 8$m/s. Figure 7.7 shows the mean toughness values for all three tested materials. PMMA exhibits the lowest toughness values, whereas the K_d values for PVC and PE are quite close. In Figure 7.8 the fracture toughness is displayed versus fracture time. The toughness of PMMA falls with decreasing fracture time, whereas for PVC and PE a minimum at 40μs (PVC) and 90μs (PE) is observed.

7.7 The dynamic energy release rate results

The dynamic energy release rate results for the three materials tested are presented in Figure 7.9 to 7.11. Due to the large changes the G_d values are plotted on a log scale. In comparison to K_d the scatter is increased in G_d due to the nature of the K_d-G_d conversion. A fit with a new thermal decohesion model [86] was added. The values for the fitting parameters, the critical distance, z_c, and a transition temperature, T_m, are given in the graphs. Except for the low T_m value for PMMA, the values for z_c and T_m are quite realistic. The results from the thermal decohesion model lead to the conclusion that the rise in G at high rates could be due to thermal effects. By calculating the mean value for each impact velocity Figure 7.12 is the result, which shows the tendency for the tested materials more clearly. For PMMA we find a slightly falling G_d value up to 8m/s, above which G_d then stays constant at about 1200J/m^2. For PVC and PE a tendency with a minimum at 8m/s is observed, as we found it for K_d for these materials. Up to 8m/s G_d drops by an order of magnitude for PVC and PE. Figure 7.13 shows a plot of the dynamic energy release rate versus the fracture time. Similar to Figure 7.8 G_d for PMMA decreases with falling fracture time and a tendency with a minimum energy release rate at 40μs for PVC and at 90μs for PE is observed.

Chapter 8

Summary and Conclusions

The aim of this work was to contribute towards a possible standard test method for K_d and G_d for polymers at high rates of loading. The understanding of the test was improved with numerical analysis and the results from this analysis were used to improve a previous test procedure and to calculate K_d and G_d for a series of tests.

A test series with PMMA, PVC and PE was performed and the time to fracture, t_s, was measured for a wide range of impact velocities. Data from a round robin within ESIS TC4 with these three materials, which was performed as a part of this project, is also presented. The observed time to fracture showed a relatively large scatter and a further round robin would be advisable to improve the accuracy of the measurements. The time to fracture was found to exhibit a $-4/3$ dependency with impact velocity in a double logarithmic diagram not only for the thermoplastics tested, but also for three epoxy materials. This tendency was explained with a thermal model, which indicates that the fracture process could be a thermal phenomenon caused by heat trapped in a small zone around the crack tip.

A simple finite volume (FV) model of the three point bend (TPB) test, where striker and anvil were modeled by special boundary conditions on single cell faces was analyzed. The analysis results showed reasonable agreement with experiments performed by Böhme [24] for the dynamic correction function k_d. The anvils were found not to be important in the initial stage of a high rate test, as they influence the k_d curve only at a late stage of the test, where in most cases with a high impact velocity fracture initiation has already occurred. In the initial stage a TPB test is therefore actually a one point bend test. From a FV analysis with the simple model it was further found that the dynamic stress intensity factor (SIF) from the crack tip closure integral method agrees with the SIF obtained from the basic definition of K, i.e. from the local stress field. An analysis of the method of calculating K with the bending moment at midspan showed that at short times this method does not agree with the SIF found at the crack tip and

hence 1D models of the TPB test using the bending moment to cacluate the SIF will not yield accurate SIF values at short times.

Investigations of the applicability of a k_d curve to other test conditions than the ones for which it was determined showed that for a linear contact stiffness the impact velocity, V, can be changed without affecting the k_d curve. The specimen width, W, can also be varied without a change in the k_d curve, if the specimen dimension ratios, a/W, which is the crack length to width ratio, L/W, the specimen length to width ratio and the span to width ratio, S/W, are held constant. The dynamic correction function for the energy release rate g_d was found to exhibit larger oscillations than k_d, because $g_d = k_d^2$.

A FV model of the TPB test with a contact procedure, which allows accurate modeling of the contact problem, gave a significantly better fit with the experiment. It was found that the contact stiffness at the anvil affects the k_d curve at a later stage of the test and that the model with a compliant epoxy anvil showed better agreement with the experiment than the model with a steel anvil, as in the experiment a compliant epoxy anvil was used to enable measurement of the anvil load. It was also found that the contact stiffness between striker and specimen plays an important role and affects the shape of the k_d curve. A change of the striker stiffness, which affects the contact stiffness, yielded a high degree of change in k_d, whereby a lower striker stiffness reduced the initial slope of the k_d curve. Virtually the same k_d curve was found for an epoxy striker and specimen and for a steel striker and specimen, which led to the conclusion that the application of a k_d curve determined with a steel striker and a polymer specimen to a test with a steel striker and specimen will lead to wrong results. From the FV model it was found that a change of the striker radius has only a small effect on the k_d curve. The striker radius is usually prescribed in a test protocol and hence minor striker radius variations, which can occur due to inaccuracies from machining or wear of the striker tip, will have a negligible effect on the k_d curve.

If the contact model was used, the impact velocity was found to have a significant influence on the k_d curve due to the nonlinear contact stiffness. The contact stiffness becomes higher with increasing impact velocity and hence the initial slope of the k_d curve increases. The initial peak and the subsequent oscillations of the k_d curve also increase with rising impact velocity. If a k_d curve is used for the evaluation of a test with an impact velocity different than the one at which the curve was determined, errors will occur. For small velocity differences these errors are negligible, but if the impact velocity is drastically changed, a correction is necessary to keep the error of k_d small.

The specimen width has only a small influence on k_d for the model including contact effects, as long as the specimen dimension ratios, a/W, L/W and S/W, are held constant. Therefore a k_d curve obtained with a particular specimen width can be used for tests with other specimen widths. The specimen material does not affect the k_d curve

significantly if the specimen is made from a polymer and if a metal striker is used, which can be considered as rigid in comparison. One k_d curve can therefore be used for a comparably rigid striker and different polymers with good accuracy.

A check of the energy release rate results from the crack closure integral method was performed by comparing the results from the crack closure integral method with the results from the J integral for a stationary crack in a transient stress field. A center cracked panel with a load step applied was used for this purpose. For a converged FV solution the results from the crack closure integral method agreed perfectly with the J integral method. It was further found that there is no difference between a global and a local G value by using different paths for the J integral. The converged FV solution was found to yield the same results for any path, whether close or far from the crack tip. The crack closure integral method is easy to implement and very mesh insensitive, which is a big advantage over the J integral method, which was found to be very mesh sensitive and also more difficult to implement in a FV program.

K_d and G_d for the test series for PMMA, PVC and PE were evaluated from time to fracture with a procedure based on that used in the data analysis of the previous round robin [61] and the results of this work. Some modifications of the procedure of the previous round robin were done in the light of the results of the numerical analysis of the test. Due to a large variation in impact velocity a correction was performed by interpolating between the 1, 10 and 30m/s k_d curves to obtain a dynamic correction for a particular impact velocity. This correction was applied in the dynamic time range for the nondimensional time, $X < 12$, whereas for $X > 12$ a quasistatic time range was defined, where no dynamic correction was applied. Polynomials fitting the numerically evaluated k_d curves for 1, 10 and 30m/s were presented, which can be used in the dynamic time range to obtain k_d. This dynamic correction procedure could be the basis for more improvements by performing another TC4 round robin on this subject and one step towards a possible test standard for TPB impact tests. An error analysis showed that K_d and G_d are very sensitive to errors in the time to fracture. In the worst case, for a small value of t_s in the steepest part of the k_d curve, the error on t_s can be magnified by a factor of 4 in the case of K_d and by a factor of 10 in the case of G_d. Taking the mean value of several measurements per impact velocity will drastically reduce the random error on K_d and G_d and hence is recommended. A rise in fracture toughness was found for PVC and PE at high velocities > 8m/s, whereas for PMMA only a small drop of the fracture toughness with a subsequent plateau from 8 to 27m/s is observed. The energy release rate shows the same tendency as the fracture toughness, but the changes with impact velocity are larger, as G_d is proportional to K_d^2.

Bibliography

[1] American Society for Testing and Materials. Standard Test Methods for Plane Strain Fracture Toughness and Strain Energy Release Rate of Plastic Materials. Test Standard D5045-91a, ASTM, 1991.

[2] J. G. Williams. A Linear Elastic Fracture Mechanics (LEFM) Standard for Determining K_c and G_c for Plastics. Testing Protocol, ESIS TC4, 1990.

[3] A. Pavan. A Linear Elastic Fracture Mechanics (LEFM) Standard for Determining K_{Ic} and G_{Ic} for Plastics at High Loading Rates. Testing Protocol, ESIS TC4, 1997.

[4] A. Ivankovic and J.G. Williams. *Dynamic Fracture Mechanics*, chapter The Finite Volume Analysis of Linear Elastic Dynamic Fracture Problems. Computational Mechanics Publications, Southampton, 1995.

[5] G. R. Irwin. *Elasticity and Plasticity*, volume 6, chapter Fracture. Springer, Berlin, 1958.

[6] E. F. Rybicki and M. F. Kanninen. A Finite Element Calculation of Stress Intensity Factors by a Modified Crack Closure Integral. *Engineering Fracture Mechanics*, 9, 1977.

[7] I. Demirdzic and A. Ivankovic. Finite Volume Stress Analysis. Lecture notes, Imperial College, Department of Mechanical Engineering, 1999/2000.

[8] C. J. Jih and C. T. Sun. Evaluation of a finite element based crack-closure method for calculating static and dynamic strain energy release rates. *Engineering Fracture Mechanics*, 37(2), 1990.

[9] L. B. Freund. *Dynamic Fracture Mechanics.* Cambridge University Press, 1989.

[10] L. M. Brock, M. Jolles, and M. Schroedl. Dynamic Impact over a Subsurface Crack: Applications to the Dynamic Tear Test. *Journal of Applied Mechanics*, 52(2), 1985.

[11] A. C. Eringen and E. S. Suhubi. *Elastodynamics*, volume 2. Academic Press, 1975.

[12] J. D. Achenbach. *Wave Propagation in Elastic Solids.* North-Holland Publishing Company, Amsterdam, 1973.

[13] W. Böhme. The Influence of Stress Waves on the Dynamic Crack Tip Loading in Three-Point Bend Impact Testing. In *Impact Loading and Dynamic Behaviour of Materials*, Oberursel, Germany, 1988. Deutsche Gesellschaft für Metallkunde.

[14] J. E. Srawley. Wide Range Stress Intensity Factor Expressions for ASTM E 399 Standard Fracture Toughness Specimens. *International Journal of Fracture*, 12, 1976.

[15] F. Körber and A. A. Storp. Über den Einfluss der Probenbreite und der Temperatur auf den Kraftverlauf beim Kerbschlagbiegeversuch. *Mitteilungen aus dem Kaiser Wilhelm Institut für Eisenforschung*, 8, 1926.

[16] G. E. Nash. An Analysis of the Forces and Bending Moments Generated During the Notched Beam Impact Test. *International Journal of Fracture Mechanics*, 5(4), 1969.

[17] G. E. Nash and E. A. Lange. Mechanical Aspects of the Dynamic Tear Test. *Journal of Basic Engineering*, 91(4), 1969.

[18] H. J. Saxton, D. R. Ireland, and W. L. Server. Analysis and Control of Inertial Effects During Instrumented Impact Testing. *Instrumented Impact Testing, ASTM STP 563*, 1974.

[19] C. E. Turner, L. E. Culver, J. C. Radon, and P. Kennish. An Analysis of the Notched Bar Impact Test With Special Reference to the Determination of Fracture Toughness. In *Practical Application of Fracture Mechanics of Pressure Vessel Technology*, number C6/71, London, 1971. Institute of Mechanical Engineers.

[20] K. Kishimoto, S. Aoki, and M. Sakata. Simple Formula for Dynamic Stress Intensity Factor of Pre-Cracked Charpy Specimen. *Engineering Fracture Mechanics*, 13, 1980.

[21] W. Böhme and Kalthoff. The Behaviour of Notched Bend Specimens in Impact Testing. *International Journal of Fracture*, 20, 1982.

[22] K. Kishimoto, K. Kuroda, S. Aoki, and M. Sakata. Simple Formulae for Dynamic Fracure Mechanics Parameters of Elastic and Viscoelastic Three-Point Bend Specimens Based on Timoshenko's Beam Theory. In *Advances in Fracture Research: Proceedings of the 6th International Conference on Fracture*, Oxford, 1984. Pergamon Press.

[23] J. F. Kalthoff. On the Measurement of Dynamic Fracture Toughness - a Review of Recent Work. *International Journal of Fracture*, 27(3–4), 1985.

[24] W. Böhme. *Experimentelle Untersuchungen Dynamischer Effekte beim Kerbschlagbiegeversuch.* PhD thesis, TH Darmstadt, 1985.

[25] J. H. Giovanola. One-Point Bend Test. In *Metals Handbook*, volume 8, Metals Park, Ohio, 1985. American Society for Metals.

[26] T. Peuser. Dynamic Analysis of Impact Test Specimens. In *Proceedings, AFMMS International Conference*, Freiburg, 1983. Martinus Nijhoff.

[27] D. R. Ireland. Critical Review of Instrumented Impact Testing. In *Proceedings of the International Conference on Fracture Toughness*, Cambridge, 1976. The Welding Institute.

[28] W. Böhme. Dynamic Key Curves for Brittle Fracture Impact Tests and Establishment of a Transition Time. In *Fracture Mechanics: Twenty-First Symposium, ASTM STP 1074*, pages 144–156, Philadelphia, 1995. ASTM.

[29] J. F. Kalthoff, S. Winkler, W. Böhme, and W. Klemm. Determination of the Dynamic Fracture Toughness K_{Id} in Impact Tests by Means of Response Curves. In *Advances in Fracture Research*, Oxford, 1980. Pergamon Press.

[30] J. F. Kalthoff, S. Winkler, and W. Böhme. A Novel Procedure for Measuring the Impact Fracture Toughness K_{Id} with Precracked Charpy Specimen. *Journal de Physique*, Colloque C5, No. 8, Tome 46, 1985.

[31] W. Böhme. Application of Dynamic Key Curves for the Determination of the Impact Fracture Toughness of Polymers at High Rates of Loading. In J. G. Williams and A. Pavan, editors, *Impact and Dynamic Fracture of Polymers and Composites*, number 19, London, 1995. ESIS, Mechanical Engineering Publications.

[32] R. J. Bucci, P. C. Paris, J. D. Landes, and J. R. Rice. J integral estimation procedures. In *Fracture Toughness, ASTM STP 514*, 1972.

[33] P. R. Marur. Charpy Specimen - A Simply Supported Beam or a Constrained Free-Free Beam? *Engineering Fracture Mechanics*, 61, 1998.

[34] P. R. Marur. Numerical Simulation of Anvil Interactions in the Impact Testing of Notched Bend Specimens. *International Journal of Fracture*, 81, 1996.

[35] I. V. Rokach. Modal Approach for Processing One- and Three-Point Bend Test Data for DSIF-Time Diagram Determination. Part I Theory. *Fatigue and Fracture of Engineering Materials and Structures*, 21, 1998.

[36] I. V. Rokach. Modal Approach for Processing One- and Three-Point Bend Test Data for DSIF-Time Diagram Determination. Part II Calculations and Results. *Fatigue and Fracture of Engineering Materials and Structures*, 21, 1998.

[37] G. Weisbrod and D. Rittel. A Method for Dynamic Fracture Toughness Determination Using Short Beams. *International Journal of Fracture*, 104, 2000.

[38] J.G. Williams. The Analysis of Dynamic Fracture Using Lumped Mass-Spring Models. *International Journal of Fracture*, 33, 1987.

[39] J.G. Williams. The Analysis of Instrumented Impact Tests Using a Mass-Spring Model. *International Journal of Fracture*, 33, 1987.

[40] J.G. Williams, V. Tropsa, H. MacGillivray, and A. Rager. Dynamic Correction Factors for K and G in High Rate, SENB, Impact Tests. *International Journal of Fracture*, 107(3), 2001.

[41] P. R. Marur. Influence of Anvil Supports and Overhangs in Dynamic Analysis of Three Point Bend Testing. *International Journal of Fracture*, 69, 1994.

[42] I. V. Rokach. Numerical Evauation of the Anvil Force for Precise Processing of the Impact Fracture Test Data. In *Proceedings ECF 11 - Mechanisms and Mechanics of Damage and Failure*, 1996.

[43] I. V. Orynyak and A. J. Krasowsky. The Modelling of Elastic Response of a Three Point Bend Specimen Under Impact Loading. *Engineering Fracture Mechanics*, 60(5–6), 1994.

[44] P. R. Marur, K. R. Y. Simha, and P. S. Nair. Dynamic Analysis of Three Point Bend Specimens under Impact. *International Journal of Fracture*, 68, 1994.

[45] P. R. Marur. Dynamic Analysis of One-Point Bend Impact Test. *Engineering Fracture Mechanics*, 67, 1998.

[46] T. Lorriot. Specimen Loading Determined by Displacement Measurement in Instrumented Charpy Impact Test. *Engineering Fracture Mechanics*, 65, 2000.

[47] P. Landrein, T. Lorriot, and L. Guillaumat. Influence of Some Test Parameters on Specimen Loading Determination Methods in Instrumented Charpy Impact Tests. *Engineering Fracture Mechanics*, 68(15), 2001.

[48] I. V. Rokach. Numerical Determination of the Dynamic Key Curves. In *Proceedings ECF-13*, San Sebastian, 2000.

[49] I. V. Rokach. Simple Formulae for Processing of the Results of a One-Point Bend Test. In *Charpy Centenary Conference*, Poitiers, 2001.

[50] D. R. Ireland. Procedures and Problems Associated with Reliable Control of the Instrumented Impact Test. In *ASTM STP 563*, Phiadelphia, 1974. ASTM.

[51] K. Oi. Transient Response of Bonded Strain Gages. *Experimental Mechanics*, 6(9), 1966.

[52] K. Ueda and A. Umeda. Dynamic Response of Strain Gages up to 300kHz. *Experimental Mechanics*, 38(2), 1998.

[53] S. Winkler. On the Determination of Dynamic Properties of Instrumentation. In *Conference on Instrumented Impact Testing of Metallic Materials*, Teddington, 1991. National Physical Laboratory.

[54] J. W. Dally and R. J. Sanford. Strain Gage Methods for Measuring the Opening-Mode Stress-Intensity Factor, K_I. *Experimental Mechanics*, 27(4), 1987.

[55] W. N. Jr. Sharpe and W. Böhme. Dynamic Fracture Toughness Measurements on Small Charpy Specimens - A Preliminary Study. *Journal of Testing and Evaluation*, 22(1), 1994.

[56] S. De Luna, L. Rubio, J. L. Perez-Castellanos, J. Fernandez-Saez, and C. Navarro. Some Developments in Dynamic Fracture Mechanics. In *Proceedings ECF-13*, San Sebastian, 2000.

[57] A. G. Dutton and R. A. W. Mines. Analysis of the Hopkinson Pressure Bar Loaded Instrumented Charpy Test Using an Inertial Modelling Technique. *International Journal of Fracture*, 51, 1991.

[58] A. Rager, I. Horsfall, Z. Major, R. Moore, A. Pavan, and J. G. Williams. The determination of time to fracture for polymers at high rates of loading. To be published.

[59] ESIS. www.shef.ac.uk/mecheng/tribology/esis.

[60] W. Böhme. Application of Dynamic Key Curves (DKC) on the Determination of the Impact Fracture Toughness K_{Id} of Plastics at High Rates of Loading. Technical report, Fraunhofer-Institut für Werkstoffmechanik, Freiburg, 1998.

[61] W. Böhme. Determination of the Impact Fracture Toughness K_{Id} of Plastics at High Rates of Loading "> 1m/s". In *Fracture Mechanics Testing Methods for Polymers, Adhesives and Composites.* Elsevier, Oxford, 2001.

[62] P.S. Leevers, S. Hazra, and S. Hillmansen. Impact Resistance of Thermoplastics Prediction from Bulk Properties. *Plastics, Rubber and Composites*, 29(9), 2000.

[63] P.S. Leevers. Impact and Dynamic Fracture of Tough Polymers by Thermal Decohesion in a Dugdale Zone. *International Journal of Fracture*, 73(2), 1995.

[64] K. Jagust. High Rate Tests on Polymers. 3M Final Report, Imperial College, London, 1999.

[65] J.G. Williams and J. M. Hodgkinson. Crack-blunting mechanisms in impact tests on polymers. In *Proceedings Royal Society London*, number 375, 1981.

[66] J. G. Williams. Introduction to the Work of ESIS TC4. In *Fracture Mechanics Testing Methods for Polymers Adhesives and Composites.* Elsevier, Oxford, 2001.

[67] I. Demirdzic and S. Muzaferija. Finite Volume Method for Stress Analysis in Complex Domains. *International Journal for Numerical Methods in Engineering*, 37(21), 1994.

[68] A. Ivankovic, I. Demirdzic, J.G. Williams, and P. S. Leevers. Application of the Finite Volume Method to the Analysis of Dynamic Fracture Problems. *International Journal of Fracture*, 66(4), 1994.

[69] A. Ivankovic. Finite Volume Modeling of Dynamic Fracture Problems. *Computer Modeling and Simulation in Engineering*, 4(3), 1999.

[70] V. Stylianou. Finite Volume Analysis of Dynamic Fracture Phenomena. *International Journal of Fracture*, 113, 2002.

[71] K. Maneeratana. *Development of the Finite Volume Method for Non-Linear Structural Applications.* PhD thesis, Department of Mechanical Engineering, Imperial College, 2000.

[72] H. Jasak and H.G. Weller. Finite volume methodology for contact problems of linear elastic solids. In *Proceedings of 3rd International Conference of Croatian Society of Mechanics, Cavtat/Dubrovnik*, September 2000.

[73] FOAM. http://www.nabla.co.uk.

[74] Nabla Ltd. *FOAM Demonstration Guide*, 2001.

[75] Nabla Ltd. *FOAM Programmers Guide*, 2001.

[76] V. Tropsa, I. Georgiou, A. Ivankovic, and A. J. Kinloch. Modelling of Peel Tests for Automotive Applications. In *25th Annual Meeting of the Adhesion Society and the 2nd World Congress on Adhesion and Related Phenomena (WCARP-II)*, Orlando, 2002.

[77] H. Jasak and A.D. Gosman. Automatic resolution control for the finite volume method. part 2: Adaptive mesh refinement. *Numerical Heat Transfer, Part B*, 38(3), 2000.

[78] T. Nishioka and S. N. Atluri. A Numerical Study of the Use of Path Independent Integrals in Elasto-Dynamic Crack Propagation. *Engineering Fracture Mechanics*, 18(1), 1983.

[79] T. Nakamura, C. F. Shih, and L. B. Freund. Computational Methods Based on an Energy Integral in Dynamic Fracture. *International Journal of Fracture*, 27(3-4), 1985.

[80] S. H. Crandall, N. C. Dahl, and T. J. Lardner. *An Introduction to the Mechanics of Solids.* McGraw-Hill, New York, 1978.

[81] American Society for Testing and Materials. Standard Test Methods for Notched Bar Impact Testing of Metallic Materials. Test Standard E23-86, ASTM, 1986.

[82] International Organization for Standardization. Plastics – Determination of Charpy Impact Properties – Part 1: Non-Instrumented Impact Test. Test Standard ISO 179-1, ISO, 2000.

[83] T. Nishioka and S. N. Atluri. Numerical Modeling of Dynamic Crack Propagation in Finite Bodies, by Moving Singular Elements, Part 2: Results. *Journal of Applied Mechanics*, 47, 1980.

[84] A. Rager. Determination of Kc via Time-to-Fracture-Methods. Diploma thesis, University of Leoben, 2001.

[85] S. Hazra. Personal Communication, 2001.

[86] P.S. Leevers. Personal Communication, 2003.

Appendix A

Here the test procedure is given, which was distributed to the participants of the round robin as a guideline.

HIGH RATE ROUND ROBIN 2001: K_C AND G_C AT HIGH RATES OF LOADING FOR POLYMERS

A. RAGER

1. System requirements

1.1 Testing machine

A fast testing machine, which is able to cover a range of velocities from 0.2 to at least 10 m/s (up to 32 m/s is preferred) is needed. Either servohydraulic machines or drop weight towers can be used. The peak loads may go up to 6 kN. The speed has to be constant at least during the time when the striker has contact with the specimen (displacement control). Furthermore the test velocity has to be measured accurately.

1.2 Contact detection circuit

A circuit as shown in the figure below should be used.

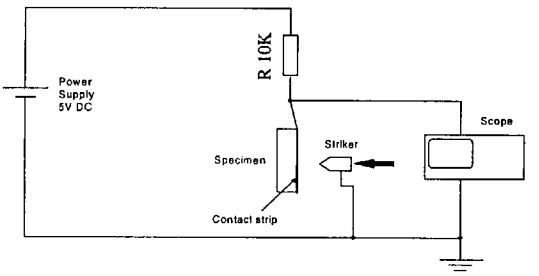

The frequency response of this equipment should be checked with a high rate test of at least 10 m/s. The rise time of the contact strip signal should be measured and it should be less than 400 ns for a rise from 10 to 90 % of the signal.

1.1 Strain measurement

A fast strain gauge amplifier has to be used for the crack tip strain gauge. The upper frequency bound at a gain of 100 (necessary for common foil gauges) has to be higher than 500 kHz. If there are doubts about the amplifier then a check with a signal generator and a scope is necessary for measuring the rise-time.
If conductive strips on the sides of the specimen are used for the detection of the point of fracture initiation, then also the rise time of the system (corresponding to an upper frequency bound: $t_r * f_g = 0.35$) has to be known. The upper frequency bound should also be higher than 500 kHz.

1.2 Load measurement

The load is measured either with a piezo loadcell or with an instrumented striker. The piezo loadcell has to be less than 20 mm away from the nose of the striker. The measured resonance frequency of the striker/loadcell system should be higher than 25 kHz. Otherwise a smaller and therefore lighter striker should be used and/or the material should be changed (aluminium, titanium preferable).
An instrumented striker with strain gauges should have the gauges less than 20 mm away from the tip of the striker. If a strain gauge amplifier is used, it should fulfil the same conditions as mentioned in 1.3.
The striker should be wider than the thickness of the specimen (here 8mm).

1.3 Signal recording

For signal recording a digital storage scope with at least 20 MS/s at 8 bit and at least 4 channels is needed.
Alternatively a PC with oscilloscope cards (specifications as above) and appropriate software can also be used.

1.4 Test rig

A rigid test rig with flat and parallel supports and a span of 64 mm is needed. The striker has to be parallel to the supports. The position of the specimen should be kept constant by stops which may be glued onto the supports with superglue and which may be removed afterwards. The specimen should be kept in place with rubber bands (machine vibration).

2. Testing details

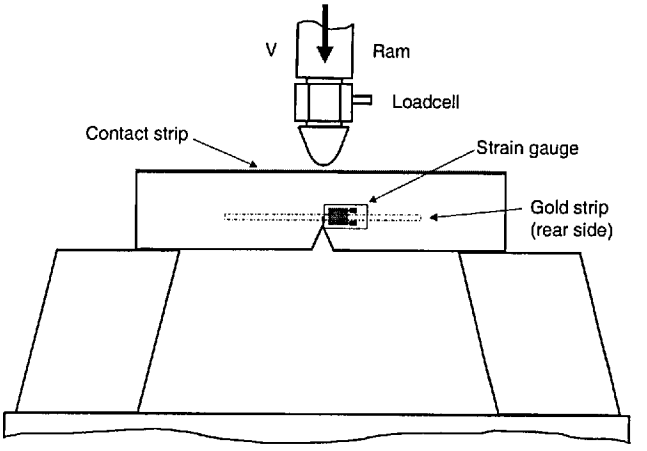

The following signals should be recorded versus time:

U_{CS}	contact strip voltage
U_{SG}	initiation detection (strain gauge/ gold strip)
P	Load
u	striker displacement (if possible)

2.1 Specimen

The chosen specimen geometry is 16*8*88 mm. The precrack has to be 4.8 mm in length for an a/W ratio of 0.3. The specimens are supplied already precracked for this round robin.

2.2 Specimen preparation

The top edge of the specimen has to be covered with a sputtered, continuous layer of gold (resistance from striker position to contact point less than 1kΩ). Therefore a sputter-coater used for electronmicroscope samples is needed. The layer should be very thin (about 50μm).

The specimen has to be equipped with a crack tip strain gauge. The strain gauge has to be placed as close to the crack tip as possible as displayed in the figure below.

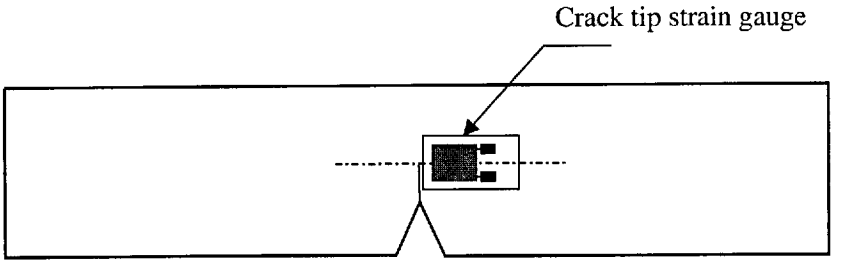

The strain gauge should be carefully aligned parallel to the specimen. The strain gauge leads should be fixed to the specimen by adhesive tape, otherwise they may come off due to machine vibrations or peel off the strain gauge. A grid size of 1.5*1.5 mm or smaller is recommended for the strain gauge.
Alternatively a conductive strip (very thin sputtered gold) across the crack tip can be used. The problem arising is that this procedure should measure the time to fracture at the crack tip. Due to variations in the time between contact detected by the contact strip and the rise of the strain gauge signal t_s cannot be measured or calculated accurately from a gold line on the specimen side. A compensation for the travelling time of the stress waves from the top of the specimen to the crack tip can be done, but will be inaccurate.

2.1 Crack length measurement

The crack length should be measured at 5 equidistant positions over the thickness of the specimen. A mean value of these five lengths should be taken as the crack length.

2.2 Time to fracture determination

The time to fracture at the crack tip is measured from the strain gauge (or from the gold line with the problems given above). The point where the strain signal starts to rise is taken as a starting point of the crak tip loading. The highest peak in the signal is taken as initiation.

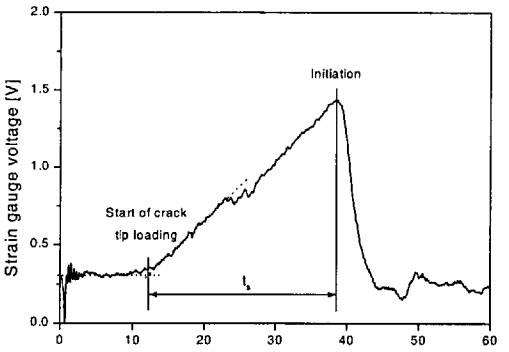

2.5 Experimental plan

The test velocities should be from the following list, depending upon the capabilities of the test system at the upper end:
0.2 1 2 4 8 16 m/s (or as a last value the maximum velocity of the machine).
Three replications for each velocity should be performed

3. Test results

The signal traces should be stored in an Excel-97 compatible spreadsheet in a folder with the abbreviation of the testing institution followed by signal traces (e.g.: IC signal traces). The name of the file should be given according to the specimen number written on the specimen. The following table shows the necessary format of the spreadsheet.

ICA10.xls

time	u	P	Usg	Ucs
[s]	[m]	[N]	[V]	[V]
-1.000E-04	-2.001E-04	2.4	0.1436	2.148
-9.939E-05	-1.988E-04	-5.7	0.1319	2.148
-9.875E-05	-1.975E-04	-5.7	0.1358	2.148
-9.811E-05	-1.962E-04	2.4	0.1358	2.148
-9.747E-05	-1.949E-04	2.4	0.1358	2.148
-9.683E-05	-1.937E-04	2.4	0.1202	2.109
-9.619E-05	-1.924E-04	-5.7	0.1436	2.148
-9.555E-05	-1.911E-04	-5.7	0.1358	2.148
-9.491E-05	-1.898E-04	-5.7	0.128	2.148
-9.427E-05	-1.885E-04	-5.7	0.128	2.148
-9.363E-05	-1.873E-04	-5.7	0.1319	2.148
-9.299E-05	-1.860E-04	2.4	0.1397	2.148
-9.235E-05	-1.847E-04	-5.7	0.1319	2.189
-9.171E-05	-1.834E-04	-5.7	0.1397	2.189
-9.107E-05	-1.821E-04	2.4	0.1358	2.189
-9.043E-05	-1.809E-04	-5.7	0.1358	2.189
-8.979E-05	-1.796E-04	2.4	0.1358	2.189
-8.915E-05	-1.783E-04	2.4	0.1358	2.189
-8.851E-05	-1.770E-04	-5.7	0.1241	2.148
-8.787E-05	-1.757E-04	2.4	0.1319	2.148

In order to be able to evaluate many test results from different laboratories it is necessary that the format of the data is standardised. Please include in the file individual graphs for u, P, U_{CS} and U_{SG} versus time. Also please use SI units as shown in the file above.

The test results should be stored in an Excel-97 compatible spreadsheet.

IC test results.xls

test no.	V [m/s]	W [m]	a [m]	b [m]	ts [s]
ICA1	0.2	0.016	4.906E-03	0.008	1.52E-03
ICA2	0.2	0.016	5.574E-03	0.008	1.54E-03
ICA3	0.2	0.016	4.758E-03	0.008	1.38E-03
ICA4	1	0.016	4.976E-03	0.008	2.73E-04
ICA5	1	0.016	4.438E-03	0.008	2.37E-04
ICA6	1	0.016	5.292E-03	0.008	3.13E-04
ICA7	1	0.016	4.518E-03	0.008	2.52E-04
ICA8	2	0.016	4.802E-03	0.008	1.41E-04
ICA9	2	0.016	5.232E-03	0.008	9.90E-05
ICA10	2	0.016	5.512E-03	0.008	1.11E-04
ICA11	4	0.016	4.516E-03	0.008	4.50E-05
ICA12	4	0.016	4.464E-03	0.008	4.26E-05
ICA13	4	0.016	4.910E-03	0.008	3.65E-05
ICA14	4	0.016	4.926E-03	0.008	5.70E-05
ICA15	8	0.016	4.598E-03	0.008	1.99E-05
ICA16	8	0.016	4.736E-03	0.008	1.99E-05

Please use the same type of spreadsheet as in the example in order to make the data reduction easier.
Also a list with the machines used and measurement devices with their specifications should be provided so that in case of big differences of the results we may be able to deduce a possible source of the differences.
The tables for the results should be stored in one Excel file (as described above) with the following abbreviations used for the testing institutions:

Testing institution	**Abbreviation**
Cranfield University	CU
ICI	ICI
Imperial College	IC
Politecnico di Milano	PDM
University of Leoben	UOL
University of Twente	UTW

Please send the results files before September to Alexander Rager, IC, either per email or on a 100 MB zip disc. The results files will be evaluated at IC and the data will be presented at the next ESIS TC4 meeting in October.

Enquiries and data to:

Alexander Rager
Mechanical Engineering Department
Imperial College of Science, Technology and Medicine
Exhibition Road
London SW7 2BX, UK
0044 171 5895111 57232 (Extension) in office 398
a.rager@ic.ac.uk